.

The Dissertation Committee for Hao Tang Certifies that this is the approved version of the following dissertation:

Applications of Self-Assembly – Liquid Crystalline Semiconductors and DNA-Conjugated Microparticles

Committee:

C. Grant Willson, Supervisor

John G. Ekerdt

Jennifer A. Maynard

Christopher J. Ellison

Edward T. Yu

Applications of Self-Assembly – Liquid Crystalline Semiconductors and DNA-Conjugated Microparticles

by

Hao Tang, B.E.

Dissertation

Presented to the Faculty of the Graduate School of

The University of Texas at Austin

in Partial Fulfillment

of the Requirements

for the Degree of

Doctor of Philosophy

The University of Texas at Austin

December 2012

Dedication

To my loving parents.

Acknowledgements

The dissertation would not be possible without the generous help from many brilliant and friendly people. I was extremely fortunate to work under the guidance of Dr. Willson during my graduate study. Over the past five years Dr. Willson has taught me far beyond science and discovery: integrity, responsibility, respect, perseverance, and excellence. I would like to thank Dr. Willson for his effort in providing resources for my graduate study and his dedication to the education of young engineers. The choice to join his research group is one of the most important choices in my life.

I would like to thank the Willson group members for their constant encouragement and support. I owe very much to the diligent administrative support from Ms. Donna Martin and Ms. Kathleen Sparks. I would like to extend my thanks to many current and former group members for their training, advice and help. This non-exhaustive list includes Dr. Xinyu Gu, Dr. Adam Berro, Dr. Brian Long, Dr. Tsuyoshi Ogawa, Dr. Jeff Strahan, Chris Bates, and Will Bell for teaching me organic synthesis and characterization skills; Dr. Elizabeth Stewart and Dr. Saul Lee for transfer of their MUFFINS technique; Dr. Brandon Rawlings, Dr. Michael Lin, Dr. Kane Jen, Dr. Siddharth Chauhan, Dr. Elizabeth Collister, and Dr. Frank Palmeri for initiating my chemical engineering journey.

Special thanks go to my research team members. Ryan Deschner has worked very hard on the DNA-conjugated microparticle project with me for four years. Without his help I would have been stopped by a large cohort of barriers halfway. I am extremely grateful to Dr. Younjin Cho, who joined this project as an extra assignment and helped clarify many key issues in DNA design and assembly. This project has also received tremendous input from Dr. Andrew Ellington and his group. Dr. Peter Allen built the foundation of microspheres self-assembly; Dr. Xi Chen helped with DNA design and characterization;

Dr. Alex Miklos provided numerous insightful suggestions in DNA conjugation. The liquid crystalline semiconductor project has enjoyed the fruitful collaboration with Dr. Patrice Rannou. I gleaned an enormous amount of knowledge and skills during my visit to his lab in summer 2010. I am also very grateful to Ryan Mesch who synthesized the terthiophene liquid crystal. I must recognize the contributions from six undergraduate students who worked on these two projects: Cecilia Hall, Rocco Hlis, Patrick Sermas, Alejandro Maurer, Brendan Folly and Kelvin Lo. Their diligent work has accelerated my research progress significantly.

Many people have generously allowed me to use their equipment. I am very much indebted to Dr. Scott Hunicke-Smith for access to the microarray scanner at the UT Genomic Sequencing and Analysis Facility; to Dr. Jack Lee, Dr. Edward Yu, and Dr. Sanjay Banerjee for access to their electrical test equipment; to Dr. Chen-Guan Lee for the transistor shadow mask; to Yujia Zhai, Fei Xue, Yanzhen Wang, Michael Ramon, Dr. Lei Zhu, Fei Zhou, and Yen-Ting Chen for help with device fabrication and testing.

I would like to acknowledge the UT Microelectronics Research Center, Center for Nano- and Molecular Science, and Institute for Cellular and Molecular Biology for the use of their instruments, and Nissan Chemical Company, Momentive, and Nippon Kayaku for generous donation of their materials. Finally, I would like to thank my dissertation committee for taking their precious time to evaluate my work and provide enlightening suggestions.

Applications of Self-Assembly – Liquid Crystalline Semiconductors and DNA-Conjugated Microparticles

Hao Tang, Ph. D.

The University of Texas at Austin, 2012

Supervisor: C. Grant Willson

Self-assembly provides an efficient way to build complex structures with great flexibility in terms of components and properties. This dissertation presents two different forms of self-assembly for technical applications. The first example is the molecular assembly of liquid crystals (LCs). Attaching appropriate side chains on anthracene, oligothiophene, and oligoarenethiophene sucessfully constructed liquid crystalline organic semiconductors. The phase transitions of the LC semiconductors were analyzed by differential scanning calorimetry (DSC) and polarized optical microscopy (POM). The effect of the LC phase change on charge transport was probed by the space-charge limited current (SCLC) method and the field-effect transistor (FET) method. Mobility in the LC phase rose in anthracenyl esters but decreased in oligothiophenes and oligoarenethiophenes. The different electronic behavior of LC semiconductors may be caused by the difference in domain size and/or the difference in response to electric field. The second example of self-assembly in this dissertation is DNA-guided self-assembly of micrometer-sized particles. Patternable bioconjugation polymers were synthesized to allow for lithographic patterning and DNA conjugation. The base pairing of DNA was then used to drive the self-assembly of DNA-conjugated particles. The DNA conjugation

chemistry was studied in detail using a fluorescence-based reaction test platform. The conjugated DNA on the polymer surface retained its ability to hybridize with its complement and was efficient in binding microspheres with complementary strands. Highly specific bead-to-bead assembly was analyzed using imaging flow cytometry, and the fractions of self-assembly products were explained on the basis of chemical equilibrium. The process of particle fabrication using photolithography was successfully developed, and the self-assembly of lithographically-patterned particles was demonstrated. We envision that the technologies described in this dissertation will be useful in a variety of fields ranging from microelectronics to biotechnology.

Table of Contents

List of Tables

List of Figures

Chapter 1: Introduction to Self-Assembly

1.1 General Features of Self-Assembly

Self-assembly is a process in which basic building blocks spontaneously assemble into higher level structures.[1] The scope of self-assembly is quite broad: the building blocks can be atoms, molecules, macromolecules, colloidal particles, or even macroscale objects with dimension up to centimeters.[2] Self-assembly can be driven by different kinds of forces, including van de Waals interaction, hydrogen bonding, capillary forces, or electric/magnetic forces. The resulting self-assembled structures are also very diverse: they can be one-dimensional (1D), two-dimensional (2D), or three-dimensional (3D). Self-assembly can also be hierarchical, that is, the primary building blocks self-organize into a primary assembly structure, and then the primary assembly structures serve as the building blocks for secondary structures. The folding of peptide chains into secondary, tertiary and quaternary structures of protein is a typical example of hierarchical self-assembly.

Understanding self-assembly is important to both science and technology. Examples of self-assembly abound in nature: phospholipids self-assemble to form cell membranes; ice nuclei grow into snowflakes; air convection and water transport form weather systems. Meanwhile, the efficiency, 3D capability and versatility of self-assembly make this phenomenon technologically attractive, providing a method to build complex systems with great flexibility in terms of components, structures, and properties. Figure 1.1 shows several examples of self-assembly and approximate dimensions of the assembled structures.

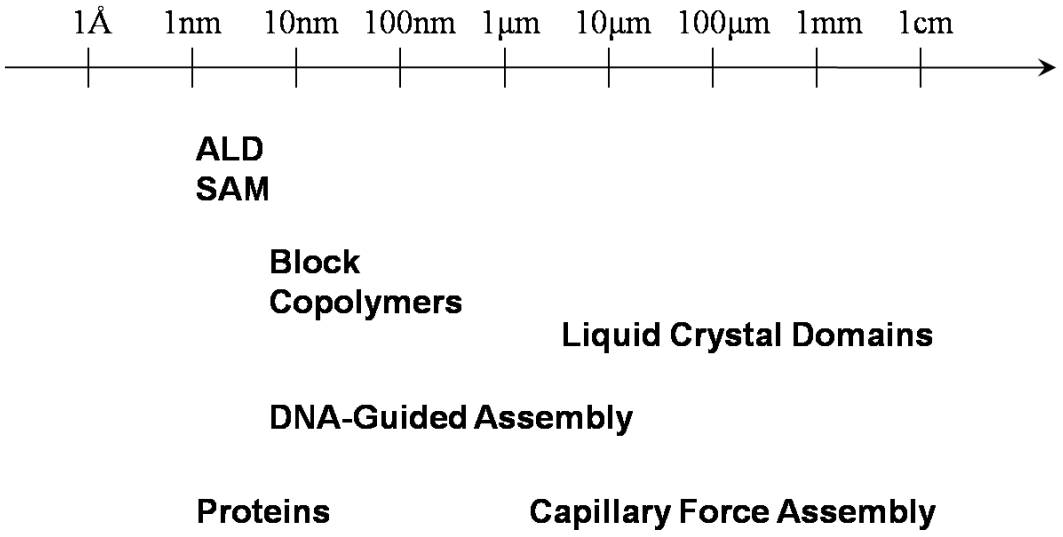

Figure 1.1 Examples of self-assembly and their approximate dimensions. ALD: atomic layer deposition; SAM: self-assembled monolayer.

1.2 Applications and Examples of Self-Assembly

Perhaps the most common example of self-assembly in daily life is the self-assembly associated with surfactants. Surfactants are usually amphiphilic molecules with a hydrophilic part and a hydrophobic part in their molecular structure. Many surfactants will self-assemble into micelles when the surfactant concentration exceeds a certain value in aqueous solution (the critical micellar concentration, cmc) (Figure 1.2a). Micelles are usually 2-20 nm in size. In the micelle structure, the hydrophilic head groups of the surfactants point out and expose themselves to water, while the hydrophobic tails hide in the middle. Notably, hydrophobic substances such as oil can be incorporated into the center of micelles, a process called micellar solubilization (Figure 1.2b). The cleaning power of detergents comes in part from micellar solubilization, and in part from their

ability to lower the surface tension at oil-water interface and thus promote the detachment of oil from substrates. Besides their daily use as detergents, surfactants are also very important in industry, for example, phase transfer catalysis and micellar catalysis, emulsion polymerization, enhanced oil recovery, [3] etc.

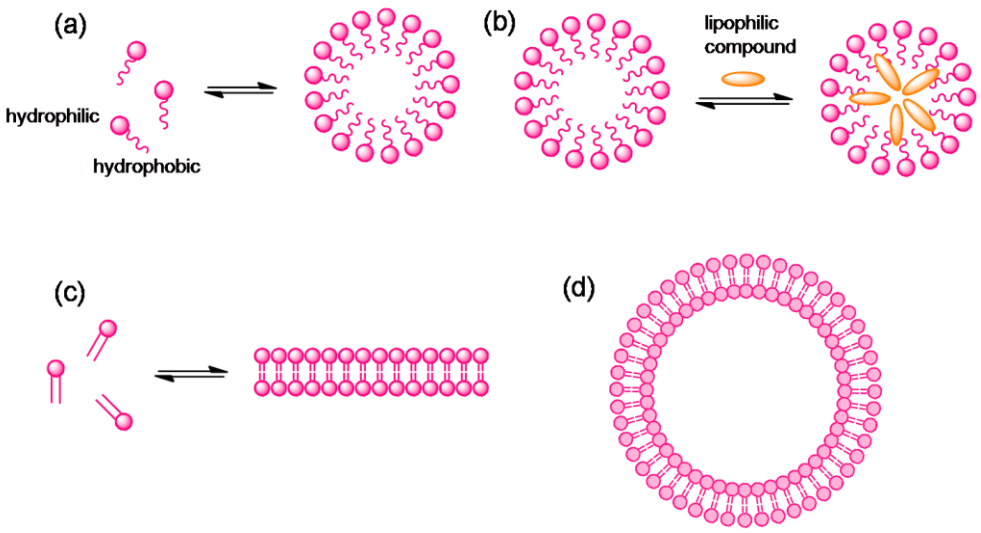

Figure 1.2 Self-assembly of surfactant (amphiphilic) molecules. (a) Formation of a spherical micelle. (b) Micellar solubilization. (c) Formation of bilayer structure. (d) Structure of a vesicle (liposome).

Surfactants can form a variety of structures in addition to spherical micelles, for example, rod-like and worm-like micelles, bilayers, and vesicles. The exact assembly structure depends on many factors, including the molecular structure of the surfactant, concentration, temperature, solvent, etc. The concept of surfactant packing parameter (g-factor) has been introduced to explain the self-assembly of surfactants.[4] Surfactants with two hydrocarbon chains are often efficient in forming bilayers and vesicles (Figure 1.2c, d). For example, phospholipid bilayer constitutes the framework of cell membranes. While cell membranes stabilize the chemical environment inside cells, they create a barrier for delivering drugs and genes into malfunctioning cells. Artificially constructed liposomes provide an important method for drug delivery. Since the approval of the first

liposome-formulated drug Doxil by US Food and Drug Administration (FDA) in 1995, more than ten liposomal drugs have been marketed.[5]

Surfactants can form liquid crystalline phases at high concentrations (typically >20 wt%), that is, the surfactant molecules in the solution have long-range orientational order. In fact, you can find such liquid crystalline phases in the "goo" at the bottom of your soap dish. The surfactant aggregates in these liquid crystals can adopt cubic, hexagonal, or lamellar packing, and their phase transitions depend primarily on the surfactant concentration. Such liquid crystals are called lyotropic liquid crystals[6]. Intriguingly, some of the hexagonal and lamellar phases formed from cationic lipids can incorporate DNA and promote the delivery of DNA into cells (Figure 1.3) [7, 8]. In contrast, liquid crystals for which temperature is the most important factor in phase transition are called thermotropic liquid crystals, and they will be discussed further in Chapter 2 and chapter 3.

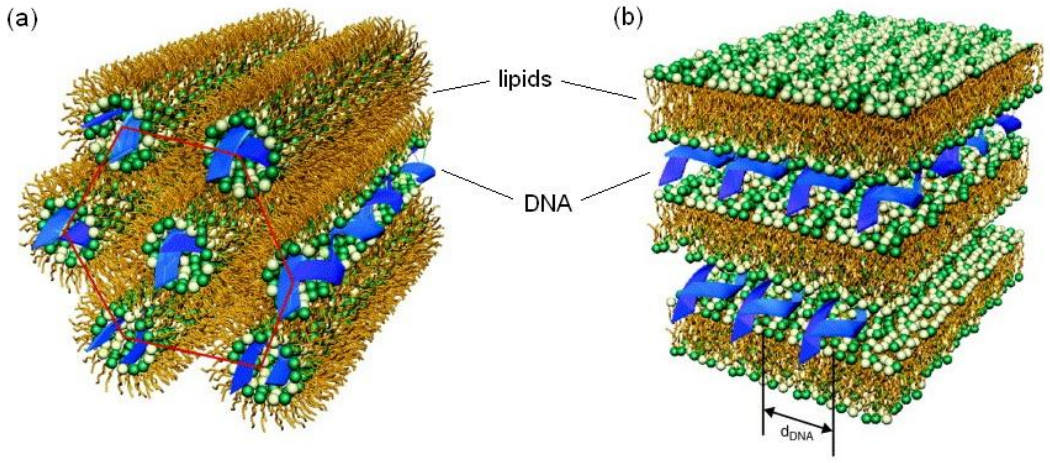

Figure 1.3 Schematics of (a) inverted hexagonal phase and (b) lamellar phase of lipid-DNA complexes. *Reprinted with permission from* [7].

An assembly that also forms hexagonal and lamellar phases occurs in the self-assembly of block copolymers. Block copolymers are polymers composed of two or more blocks

of monomers, and they can locally phase separate into nanosized domains, [9-11] as shown in Figure 1.4. A variety of structures are possible, including body centered spheres, hexagonally packed cylinders, gyroids, and lamellae. Block copolymers can generate features as small as 5 nm, rendering them very attractive for use in next-generation lithography.[12]

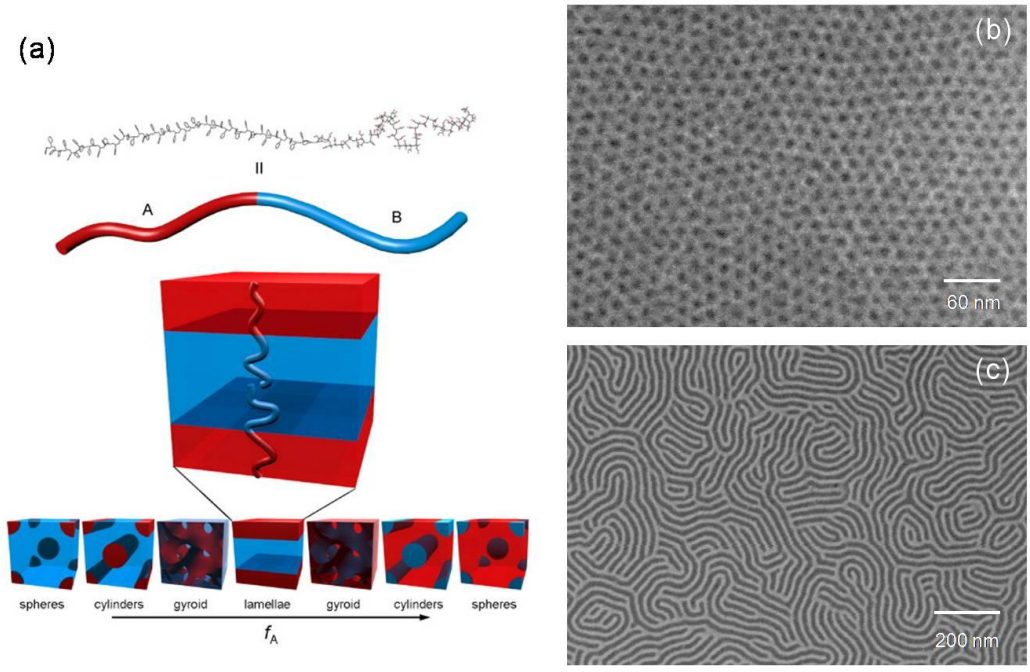

Figure 1.4 Self-assembly of block copolymers. (a) Schematics of a block copolymer and its self-assembly. (b) Scanning Electron Microscope (SEM) image of poly(4-(trimetylsilyl)styrene-b-lactide) cylinders. (c) SEM image of poly(styrene-b-4-(trimetylsilyl)styrene-b-styrene) lamellae. (a) *Reprinted with permission from* [11], (b) and (c) *Courtesy of Christopher M. Bates*.

More forms of self-assembly are finding their applications in microelectronics fabrication process. The continuous scaling down of transistor devices requires uniform and conformal deposition of very thin films on patterned substrates, where atomic layer deposition (ALD)[13] is becoming an important method for film growth. In ALD, the chemical deposition of precursors on a substrate is designed to be self-limited and layer-

by-layer (Figure 1.5). The growth of film is therefore surface reaction limited instead of mass transport limited, allowing for excellent uniformity and thickness control. ALD can be viewed as a repeated two-dimensional self-assembly process.

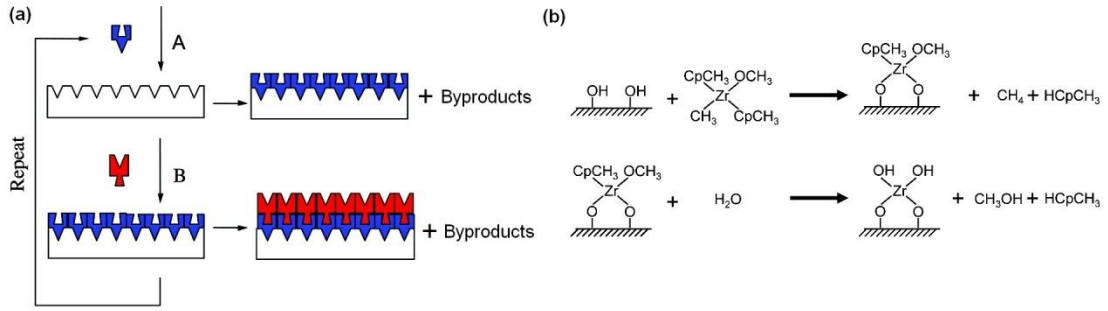

Figure 1.5 Atomic layer deposition. (a) Schematics of ALD with a binary reaction sequence. Each A-B reaction cycle gives one atomic (molecular) layer of product film, and the reaction cycle can be repeated many times to build up film thickness. *Reprinted with permission from* [13]. (b) An example of ALD deposition of ZrO_2. $CpCH_3$: methylcyclopentadienyl. *Reprinted with permission from* [14].

A 2D surface assembly that is very similar to ALD is self-assembled monolayers (SAMs). The formation of SAMs also uses self-limited chemical reactions such as the reaction of a chlorosilane with surface hydroxyls, but in this case one monolayer is formed and hence a binary reaction system and cycle repetition are not necessary. SAMs are very useful for various surface modification purposes, including electric property adjustment, adhesion control, chemical functionalization, etc. For example, SAMs are widely used to modify gate dielectrics and electrodes in organic transistors;[15, 16] Fluorinated SAMs have been used as a release agent in imprint lithography;[17, 18] Various surface functionalization reagents have been developed for DNA microarray fabrication.[19]

The self-assemblies described above can be classified as molecular self-assembly based on the size of their building blocks. Larger building blocks, such as nanoparticles and

microparticles, can also be manipulated by self-assembly. In this dissertation, self-assembly of nanosize building blocks (1 nm-100 nm) is termed nanoscale self-assembly, that of microsize building blocks (100 nm-1000 μm) is termed mesoscale self-assembly, and that of larger building blocks (> 1 mm) is called macroscale self-assembly. As an example of mesoscale self-assembly, colloidal aggregation and crystallization has been well studied (Figure 1.6a), and large size colloidal crystals can be obtained to measure their bulk properties.[20] Self-assembly at macroscale is also feasible. For example, 2mm-diameter hydrogel biosensors can self-assemble with capillary force to a biosensor array (Figure 1.6b), and 2.5cm triangles with magnets can self-assemble into hexagons[21] (Figure 1.6c).

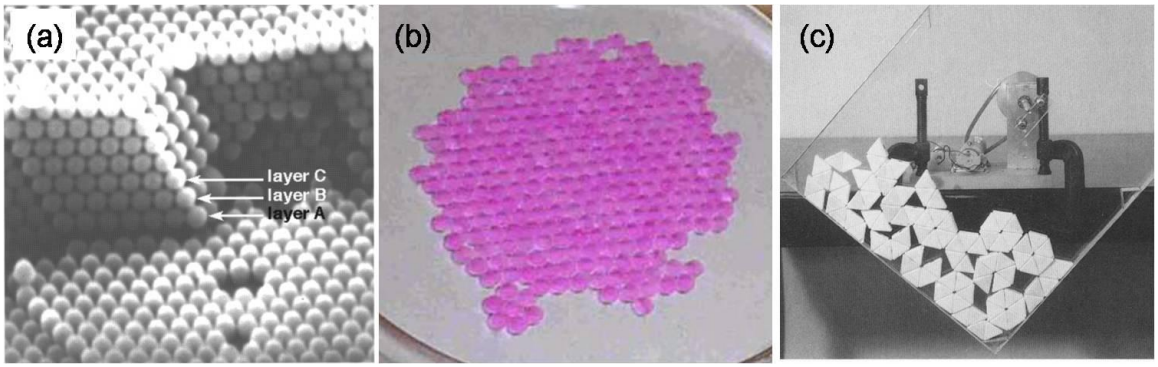

Figure 1.6 Mesoscale and macroscale self-assembly. (a) Crystallization of 0.48 μm polystyrene beads by sonication in a confined chamber. *Reprinted with permission from [20]*. (b) Self-assembly of 2 mm hydrogel biosensors at an air-liquid interface. *Courtesy of Dr. Scott M. Grayson.* (c) Self-assembly of 2.5 cm polyurethane triangles. *Reprinted with permission from[21]*.

Fabrication of building blocks with well-defined valency can bring further control into self assembled structures. For example, gold nanorods with two sticky ends can self-assemble into long chains (Figure 1.7a), and the assembly kinetics closely mimics those of step-growth polymerization.[22] In contrast, polystyrene beads with two sticky ends can self-assemble into a kagome lattice (Figure 1.7b).[23] Interestingly, the crystallization of the polystyrene beads follows an aggregation-reorganization mode, instead of the

classical nucleation-growth behavior. Therefore, self-assembly not only provides a cost-effective bottom-up route for fabrication, it also serves as a model system to study fundamental phenomena such as crystallization and phase transition.

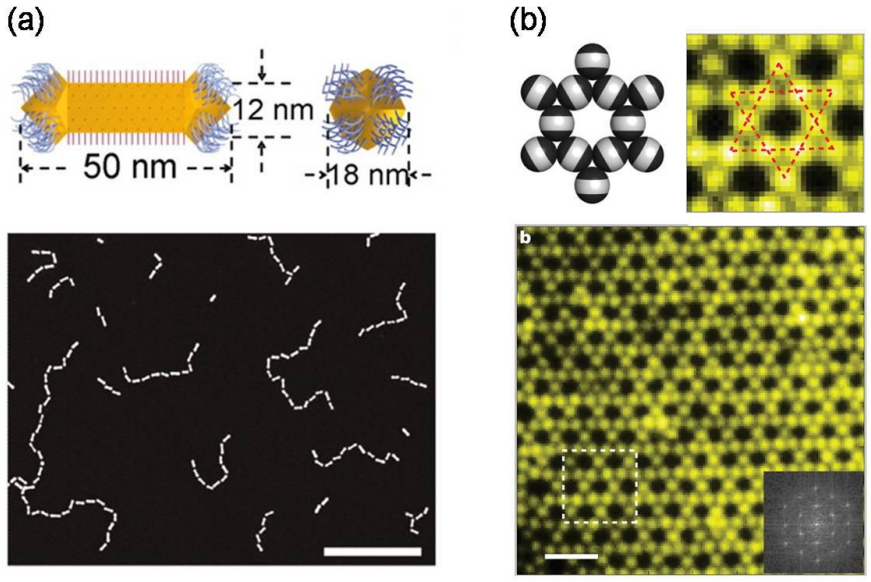

Figure 1.7 Self-assembly of building blocks with defined valency. (a) Self-assembly of 50 nm gold nanorods into polymer-like chains. *Reprinted with permission from* [22]. (b) Self-assembly of 1 μm polystyrene beads into a kagome lattice. *Reprinted with permission from* [23].

Another important class of self-assembly is related to biomolecules, for example, DNAs and proteins. DNA is a polymer of nucleotides containing four different kinds of bases: adenine (A), guanine (G), cytosine (C) and thymine (T). The base sequence stores the genetic information of life. DNA can form the well-known double helix structure (Figure 1.8a), inside which each type of nucleobases pairs with its complementary one, i.e., A binds to T and G binds to C. The high specificity of DNA base-pairing is illustrated in the example of DNA origami, where a long viral DNA was folded into almost arbitrary 2D shapes using hundreds of short DNA staples (Figure 1.8b). [24] DNA-guided self-assembly will be revisited in Chapter 4-7.

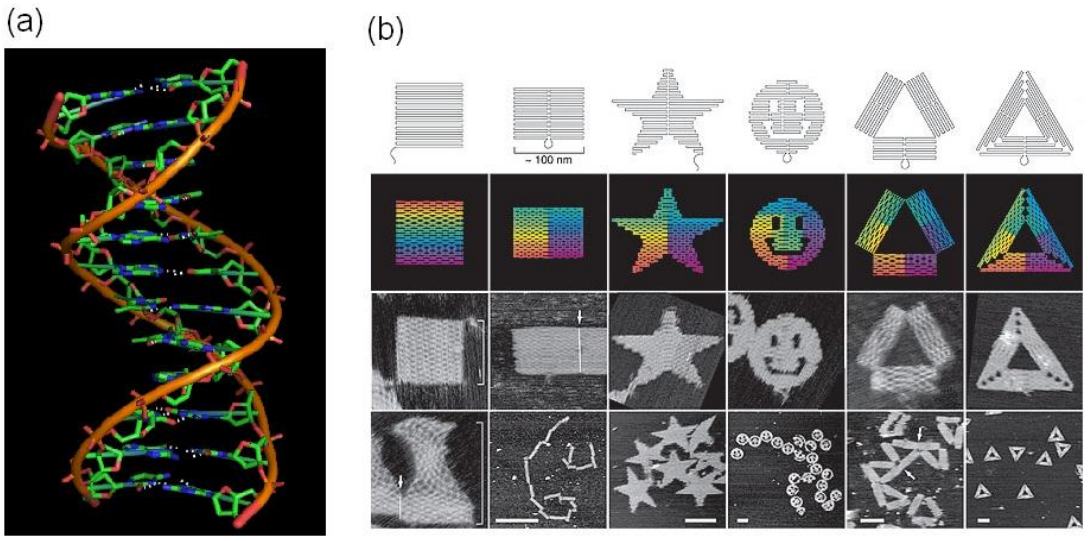

Figure 1.8 DNA and DNA origami. (a) Crystal structure of a 12bp DNA showing the double helical structure. The DNA is self-complementary with a sequence CGCAAATTTGCG. Data from PDB (Protein Data Bank) sequence 1D65. (b) Illustration and AFM image of DNA origami, created by folding M13mp18 single strand DNA with up to 273 short strands. *Reprinted with permission from* [24].

While the behavior of DNA can be predicted relatively well, the structure and function of proteins are much harder to decipher. The complexity arises partially from larger library of building blocks: proteins are composed of 20 natural amino acids instead of 4 different nucleotides. However, the rich palette of building blocks also gives proteins a much wider functional spectrum: catalysts (enzymes), structural constituents, cell signaling, and immune response. Proteins participate in almost every process in cells, and self-assembly is ubiquitous in their formation and function. For example, a heptameric protein complex (apoptosome) is assembled during the cellular aproptotic pathway (Figure 1.9a).[25] The aproptosome then recruits and activates the protein caspase-9, which can be viewed as another event of self-assembly. Another protein-related binding is biotin-avidin

interaction (Figure 1.9b). Both avidin (from egg white) and streptavidin (from the bacterium *Streptomyces avidinii*) bind biotin very strongly, thus providing a useful linker tool in many applications, for example, purification and detection of various biomolecules, [26] assembly of carbon nanotube based devices, [27] etc.

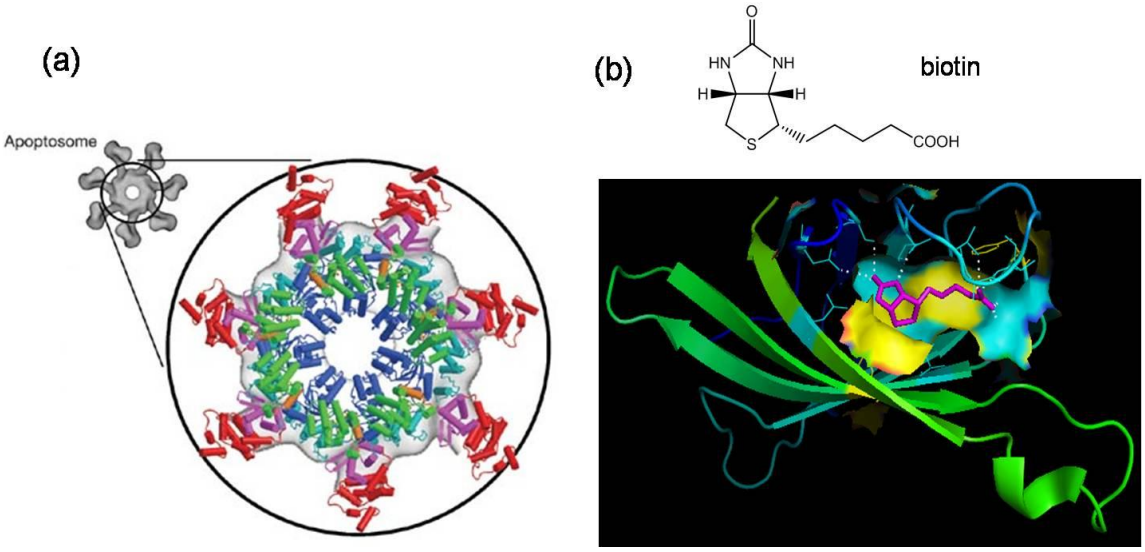

Figure 1.9 Examples of protein-related self-assembly. (a) In the intrinsic aproptotic pathway, cytochrome c released from mitochondrion binds with apaf-1(apoptotic protease activating factor 1) to form a heptameric apoptosome. *Reprinted with permission from* [25]. (b) Structure of biotin and the biotin-avidin complex. Residues forming hyrdogen bonds with biotin are colored aquamarine, and residues involved in hydrophobic interactions are colored yellow. Hydrogen bonding is shown in white dashed lines. The biotin molecule was colored magenta. Data from PDB 2AVI.

1.3 Outline of Dissertation

This dissertation presents two different research projects related to self-assembly: liquid crystalline semiconductors and DNA-functionalized microparticles. The self-assembly of liquid crystal molecules belongs to the category of molecular self-assembly, while DNA-functionalized particles provide a method for mesoscale self-assembly.

The first set of chapters present organic semiconductors with liquid crystalline phases and their charge transport properties. Chapter 2 introduces the concept of liquid crystalline semiconductors and describes the synthesis and characterization of liquid crystalline semiconductors. Chapter 3 presents the electrical measurement of liquid crystalline semiconductors by the space-charge limited current method and by the field-effect transistor method.

The latter chapters present the fabrication and self-assembly of DNA-functionalized microparticles. Chapter 4 describes lithographically patternable bioconjugation polymers and their potential to build multi-facet DNA-functionalized microparticles. Chapter 5 details the study of DNA conjugation and verification of DNA-hybridization properties. Chapter 6 presents DNA-conjugated polystyrene microspheres as a model to study DNA-guided self-assembly at the microscale. Chapter 7 presents the fabrication of DNA-functionalized microparticles by lithography and their self-assembly. Chapter 8 concludes both projects and recommends future work.

Chapter 2: Organic Semiconductors and Liquid Crystalline Semiconductors

2.1 Introduction to Organic Semiconductors

The discovery of conductivity in polyacetylenene in 1977[28] set in motion several waves of organic electronics research. In 1986, A. Trumura et al.[29] reported a polythiophene-based transistor in which the source-drain current can be well modulated by gate voltage, thus opening the era of organic field-effect transistors (OFETs). In contrast with conventional semiconductor devices based on Si or GaAs, OFETs use organic semiconductors as the active layer. The use of organic semiconductors in electronic devices brings several new features. First, organic materials can be solution-processed in cost-effective fabrication methods such as inkjet printing[30, 31] and roll-to-roll printing[32]. Second, organic semiconductors are amenable to flexible and large-area applications. Third, the use of organic semiconductors greatly broadens the choice of materials, therefore enabling special applications such as biocompatible and biodegradable devices. For example, the edible natural dyes indigo and β-carotene have been investigated for their field-effect mobilities[33].

One of the most important indicators for semiconductor performance is carrier mobility, which characterizes how fast electrons or holes can move under an applied electric field. For example, the electron mobility of single crystal silicon is about 1350 $cm^2V^{-1}s^{-1}$ at room temperature, and its hole mobility is about 480 $cm^2V^{-1}s^{-1}$. The mobility of organic semiconductors is typically much lower. For example, A. Trumura's pioneering polythiophene device in 1986 has mobility around 10^{-5} $cm^2V^{-1}s^{-1}$. Since then, tremendous improvements have been achieved in the performance of OFETs.

Pentacene set a milestone in the performance of organic semiconductors in the 1990s, with a mobility higher than 1 $cm^2V^{-1}s^{-1}$ [34]. The race of high-mobility organic semiconductors has led in 2011 to the development of 2,7-dioctyl[1]benzothieno[3,2-b][1]benzothiophene (C8-BTBT), with a maximum mobility of 31.3 $cm^2V^{-1}s^{-1}$ [31]. The structures of the above mentioned organic semiconductors are shown in Figure 2.1.

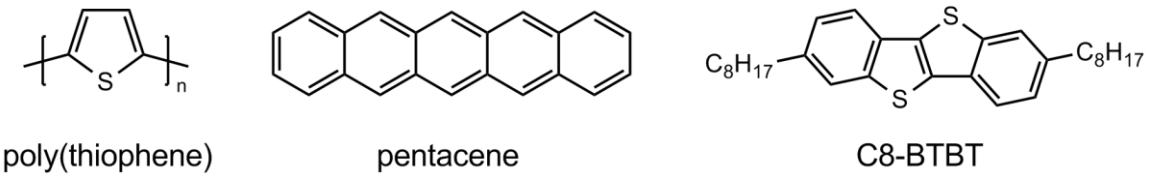

Figure 2.1 Several representative organic semiconductors: poly(thiophene), pentacene, and C8-BTBT.

All of these organic semiconductors are aromatic compounds with extensive π-conjugation. Beyond that, the structure-property relationship of organic semiconductors is quite complex but some significant insight has been gained over the years of study. Mobility depends on both intrinsic factors like molecular structure and crystal packing and extrinsic factors such as crystallinity and device configuration. The Marcus theory[35] gives intrinsic hopping mobility as:

$$\mu = \frac{qa^2}{k_B T}\frac{1}{\hbar}\left(\frac{\pi}{\lambda k_B T}\right)^{\frac{1}{2}} J^2 \exp\left(-\frac{\lambda}{4k_B T}\right) \tag{2.1}$$

where q is elementary charge, a is intermolecular spacing, k_B is the Boltzmann constant, T is temperature, $\hbar$ is the reduced Plank constant, λ is reorganization energy, and J is transfer integral. Reorganization energy describes the coupling of electronic energy and vibrational energy between neutral and charged molecular species, while transfer integral describes the orbital overlap between adjacent molecules. Both λ and J can be calculated

by *ab initio* quantum chemistry methods once the molecular structure and crystal packing structure are known.[36]

In actual devices, mobility also depends on extrinsic factors such as crystal grain size and device configuration. Crystal grain boundaries can be described as energy barriers and therefore they impede charge transport. F. Farmakis et al.[37] suggested that

$$\mu_{eff} = \mu_0 \exp(-\frac{qV_b}{k_B T}) \tag{2.2}$$

where μ_{eff} is the effective mobility, μ_0 is the intrinsic mobility, and V_b is the potential barrier of the grain boundary. In the fabrication of OFETs, it has been a routine practice to screen film growth temperatures and substrate modifications to obtain large grain sizes and thereby high mobility. In addition, several strategies to apply single crystals to OFETs have been investigated,[31, 38, 39] as single crystals of organic semiconductors usually offer the best performance.[40]

An intriguing topic in the area of organic semiconductors is liquid crystalline semiconductors (LCS). The transition from crystalline phase into liquid crystalline phase is concomitant with several structural changes that may affect the mobility. The size of LC domains (typically tens of microns) is larger than the size of crystalline grains (typically several microns). Therefore, the reduction of grain boundary density may improve the charge transport in LC phase. LC domain size can be further increased by several alignment methods, which provides a potential route to enhance the mobility in OFETs (Figure 2.2).[41-43]

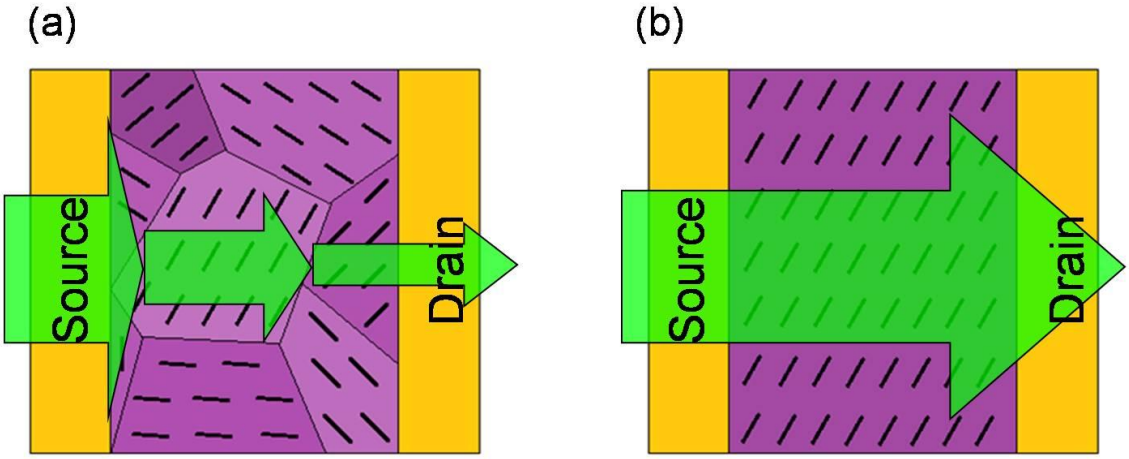

Figure 2.2 Concept of liquid crystalline semiconductors. (a) In polycrystalline materials charge transport is impeded at grain boundaries. (b) Liquid crystals can be aligned into monodomain and the grain boundary effect can be minimized.

However, several complications exist for liquid crystals. The decrease of overall molecular order in LC phase may offset the benefit of grain boundary reduction. The charge transport in LC phase is further complicated by the fact that LC molecules can switch their orientation under electric field. Mobility measurement in LC phase will help elucidate which of the mechanisms dominates in LC phase.

2.2 Liquid Crystals

Liquid crystals have orientational order between isotropic liquids and solid crystals.[44] Liquid crystals can flow like liquids, yet they possess certain amount of orientational or positional order like crystals. Many applications of liquid crystals derive from the unique combination of optical anisotropy and liquid-like behavior, with the most famous application being liquid crystal displays (LCDs). In LCDs, the liquid crystal material switches its molecular arrangement under electric field, and therefore changes its optical

properties. Such property changes under external forces are crucial to many applications of liquid crystals.

Liquid crystal can be classified into different types, as shown in Figure 2.3. Chapter 1 has introduced lyotropic liquid crystals, which are composed of two or more substances and their phase transition depends mainly on composition. In contrast, the phase transition of thermotropic liquid crystal depends mainly on temperature. A thermotropic liquid crystal usually has only one component, but multi-component mixtures are also possible.[45, 46] Thermotropic liquid crystals have two main categories: calamitic (rod-like) and discotic (disk-like), and several other non-conventional shapes have been discovered.[47]

Figure 2.3 Classification of of liquid crystals. *Courtesy of Dr. Arnold Maliniak.*

Within calamitic liquid crystals, further sub-categories of liquid crystals can be defined according to different degrees of order. The type of liquid crystal with the least degree of order is *nematic*[48], within which the LC molecules orient themselves roughly in the same direction. LC molecules in nematic liquid crystals have only orientational order but no positional order. Liquid crystals having both orientational order and positional order are called *smectic*. In smectic phases the LC molecules form layered structures (Figure 2.3).

There are many further subtypes within liquid crystals. These include smectic A, C, B, I, F phases and soft crystal B, J, G, E, K, H phases (Figure 2.4). Smectic A (SmA) and smectic C (SmC) phases have layered structures but there is no positional order within each layer. In the SmA phase the preferred orientation of LC molecules is perpendicular to the layer plane, while in the SmC phase the LC molecules are tilted with respect to the layer normal (Figure 2.4).

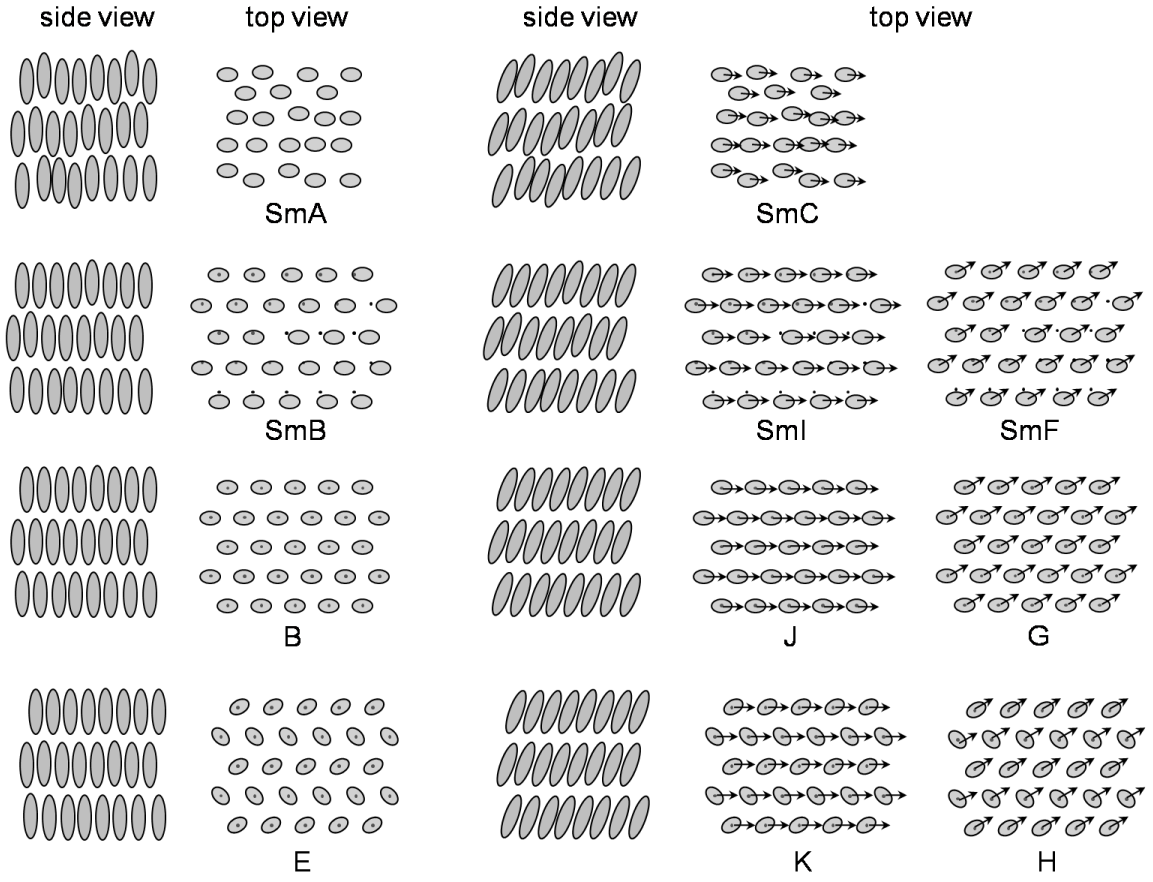

Figure 2.4 Subtypes of smectic liquid crystals. The dots indicate the positions of a perfect hexagonal array. The arrows indicate the tilt direction of the LC molecules.

Several more ordered smectic phases may appear when LCs are cooled from SmA or SmC phase. For example, the LC molecules in smectic B phase (abbreviated as SmB

phase) and soft crystal B phase (abbreviated as B phase) adopt not only a layered structure but also a roughly hexagonal packing within the layers. In smectic B phase, the spatial correlation within layers is short-range, while in soft crystal B phase, the spatial correlation is long-range. Similar to the SmA and SmC phase, tilted versions of the SmB phase and B phase exist. When the molecules in SmB phase tilt along the edge of the hexagon, the tilted phase is then called smectic I (SmI); When the molecules tilt perpendicular to the edge of the hexagon, the tilted phase is called smectic F (SmF) (Figure 2.4 and 2.5).

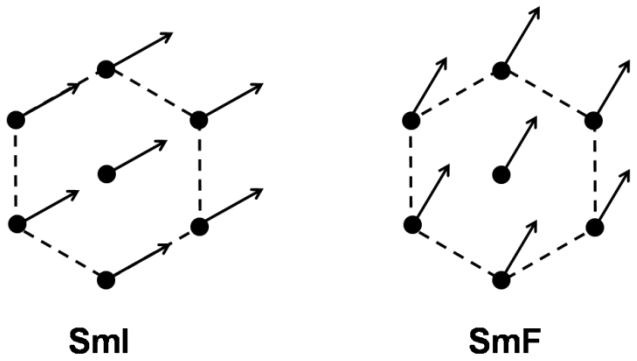

Figure 2.5 Tilt directions of SmI phase (along the edge) and SmF phase (perpendicular to the edge). Each dot represents a LC molecule and the arrow indicates the tilt direction.

Correspondingly, the tilted versions of the soft crystal B phase are the soft crystal J phase and the soft crystal G phase. The soft crystal J phase is the long-range-order version of smectic I phase and the soft crystal G phase is the long-range-order version of smectic F phase (Figure 2.4). Finally, when cooled further, the LC molecules may adopt a face-to-edge packing motif (the herringbone packing). Similar to the soft crystal B, J, G phases, there are three versions soft crystal phases with herringbone packing: soft crystal E phase, soft crystal K phase and soft crystal H phase.

By now the readers may have become very confused about the nomenclature of smectic and soft crystal phases. The major source of confusion comes from the fact that the

alphabetic assignments (SmA, SmC, SmB, SmI, SmF, B, J, G, E, K, H) are mainly determined by their timeline of discovery instead of their structural properties. For example, the E, SmF, G, H, SmI phase was initially discovered in 1966, 1971, 1971, 1972, and 1978, respectively.[49] A second part of confusion comes from the fact that in many early and even current papers, the soft crystal B, J, G, E, K, H phases are called SmB, SmJ, SmG, SmE, SmK, SmH phases, and to resolve the conflict of two SmB phases, the smectic (short-range order) B phase was called hexatic B phase (SmB_{hex}) and the soft crystal (long-range order) B phase was called crystal B phase (SmB). In this dissertation, the system of I. Dierking[50] was used, with different nomenclature for smectic and soft crystal phases.

2.3 Design, Synthesis, and Characterization of Liquid Crystalline Semiconductors

The structure of calamitic (rod-like) liquid crystal usually contains a rigid, elongated central portion and flexible end groups attached to each side of central portion, often alkyl chains. Figure 2.6 shows several liquid crystals involved in the development of LCDs. N-(4-methoxybenzylidene)-4-n-butylaniline (MBBA) and 4-Cyano-4'-pentylbiphenyl (5CB) are two liquid crystals used in early pocket calculators. A liquid crystal mixture E7 containing 5CB is used in pocket calculator and digital watch displays to the present day. The material development efforts in LC for monitor displays include the phenylcyclohexane structure and the so-called super fluorinated materials.[51-53] All of these liquid crystals have a rod-like molecular shape.

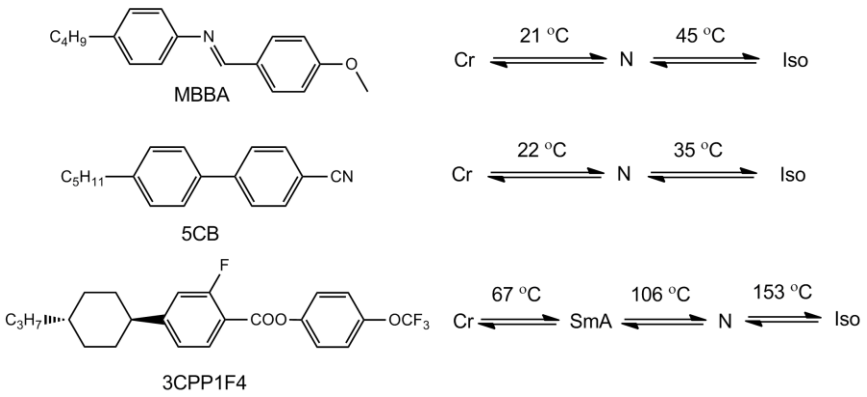

Figure 2.6 Examples of liquid crystals used in displays and their phase transition temperatures. Cr: crystalline phase, SmC: smectic C phase, N: nematic phase, Iso: isotropic liquid phase.

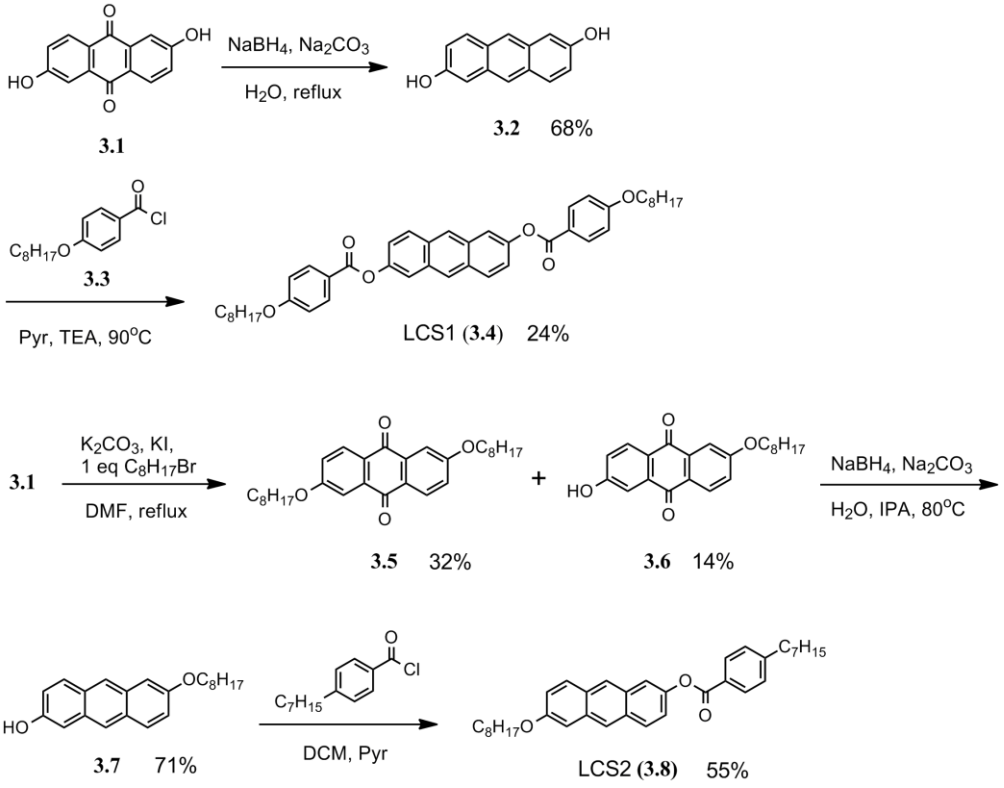

Figure 2.7 Synthesis of anthracene-based organic semiconductors. LCS: liquid crystalline semiconductor.

Acenes (naphthalene, anthracene, tetracene, pentacene, etc.) are an important class of organic semiconductors. It is reasonable to anticipate that attaching alkyl chains to acenes can produce semiconducting LC phases. Only a few examples of liquid crystals of this type have been reported in literature.[54, 55] The synthesis of two new anthracene-based liquid crystals is shown in Figure 2.7 (synthetic details in Appendix A).

A different series of organic semiconductors based on oligothiophenes and oligoarenethiophenes were synthesized and characterized (Figure 2.8). The core region of these liquid crystalline organic semiconductors is fully conjugated and therefore they provide better mobility than LCS1 and LCS2 which have ester linkage.

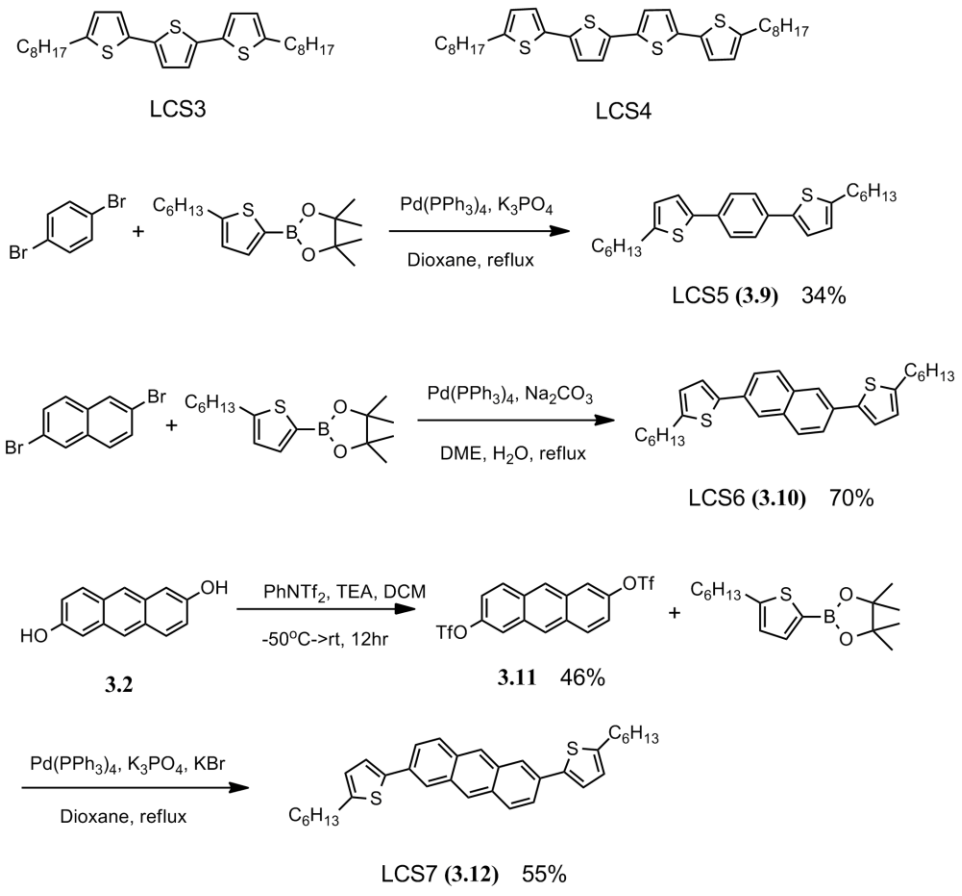

Figure 2.8 Synthesis of oligo(arene)thiophene-based organic semiconductors.

The phases of the liquid crystals were characterized by differential scanning calorimetry (DSC) and polarized optical microscopy (POM). Figure 2.9 shows the DSC traces of the anthracenyl esters LCS1 and LCS2. Each peak in DSC curve indicates an enthalpy change and a phase transition. It can be inferred from the DSC curves that LCS1 has two LC phases while LCS2 has only one LC phase.

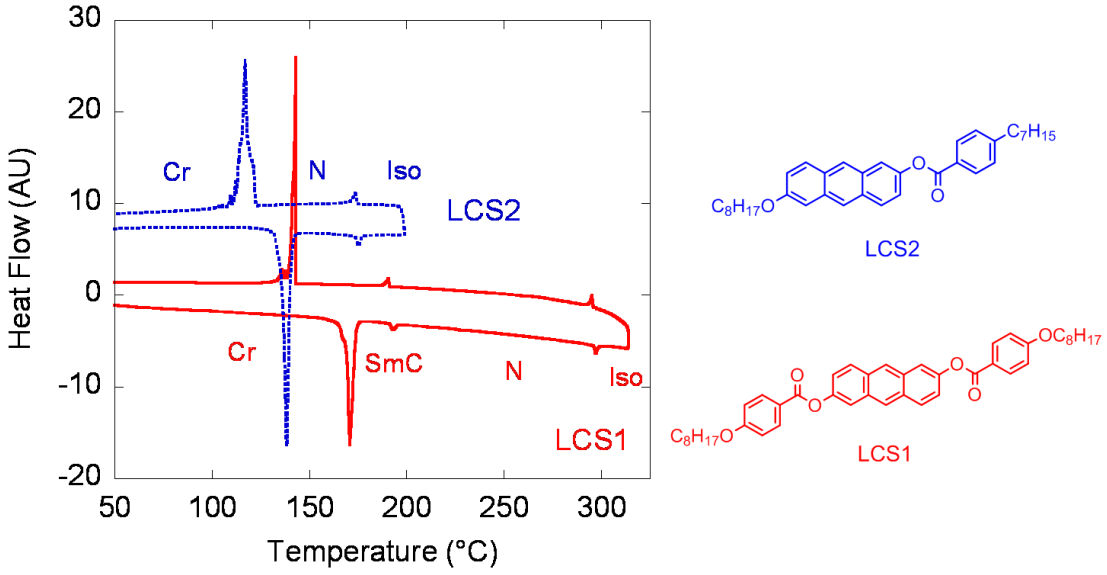

Figure 2.9 DSC traces of anthracenyl esters LCS1 and LCS2. The LC phases are assigned according to POM texture data.

Furthermore, the phase transition enthalpy (area under peak) can roughly indicate the nature of LC phase. For example, LCS2 has a large Cr to LC peak and a small LC to Iso peak (Figure 2.9), which indicates that the LC phase is closer to isotropic liquid, in this case, a nematic phase. In contrast, LCS4, LCS5, and LCS6 show a small Cr to LC peak and a large LC to Iso peak (Figure 2.10, 2.11), and their LC phases are of higher order (SmB phase).

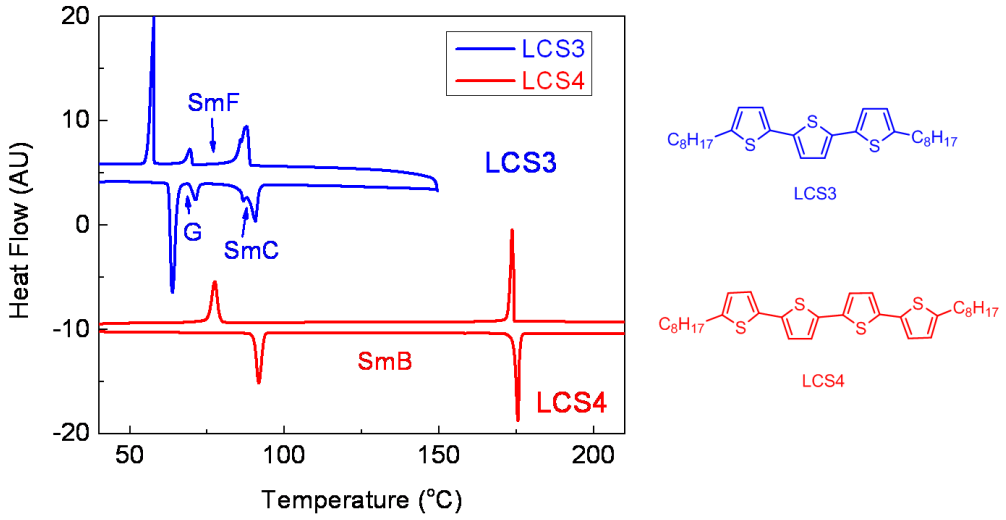

Figure 2.10 DSC traces of oligothiophenes LCS3 and LCS4. LCS3 phases are assigned according to [56]; LCS4 phases are assigned according to POM texture data.

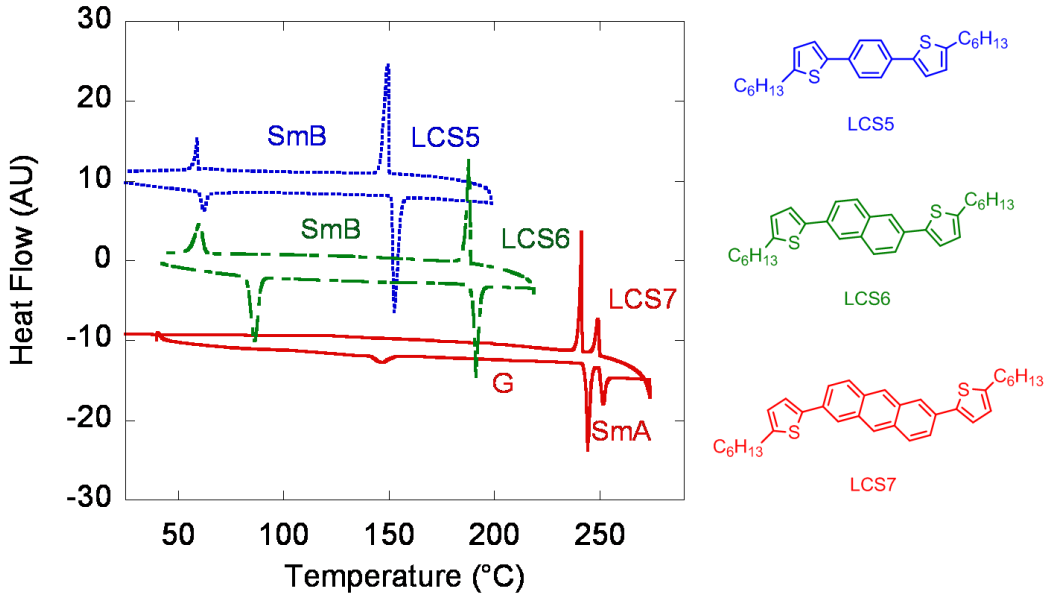

Figure 2.11 DSC traces of oligoarenethiophenes LCS5, LCS6, and LCS7. The LC phases are assigned according to POM texture data.

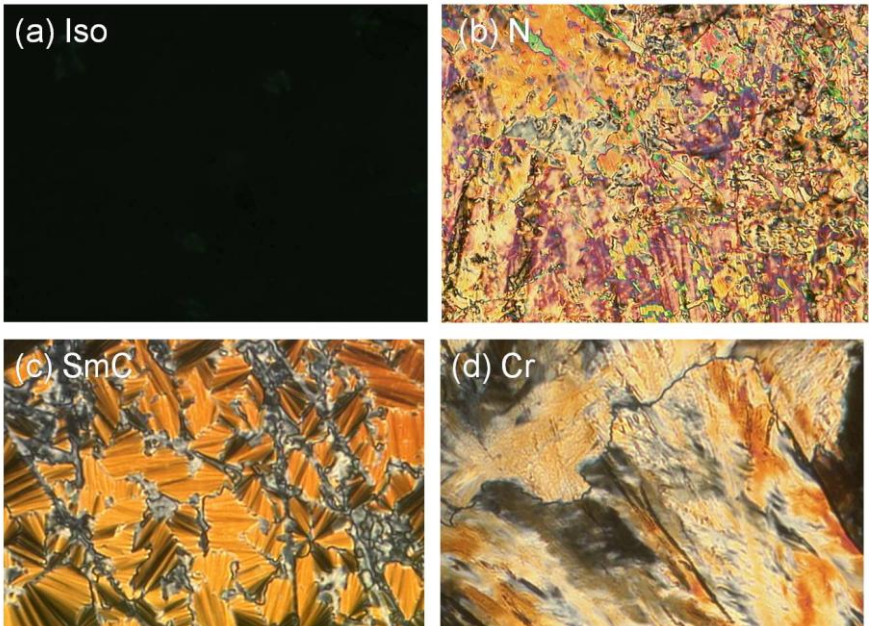

Figure 2.12 POM micrographs of LCS1 upon cooling. (a) Isotropic liquid state at 305°C. (b) Nematic marble texture at 177.5 ℃. (c) Broken fan-shaped texture of SmC phase at 160°C. (d) Crystalline phase at 140°C.

More details of the LC phases were obtained from study by POM at different temperatures. Figure 2.12 shows POM pictures of LCS1 in different phases. An isotropic liquid phase appears back under POM (Figure 2.12a). When LCS1 was cooled, it formed a nematic LC phase, and a characteristic texture appeared, in this case a generally uniform texture with different colored regions and defect lines, the so-called marble texture (Figure 2.12b). Upon further cooling, LCS1 entered a SmC phase with broken fan-shaped texture (Figure 2.12c). Finally, the sample crystallized when it was cooled below 145°C (Figure 2.12d). Figure 2.13 shows the textures of LCS2 through LCS7. Note that the assignment of hexatic smectic phases and soft crystal phases according to POM texture is sometimes only tentative owing to the fact that these high-order phases have very subtle differences in POM texture. A rigorous identification of LC phase requires X-ray diffraction and miscibility investigations.[49, 50]

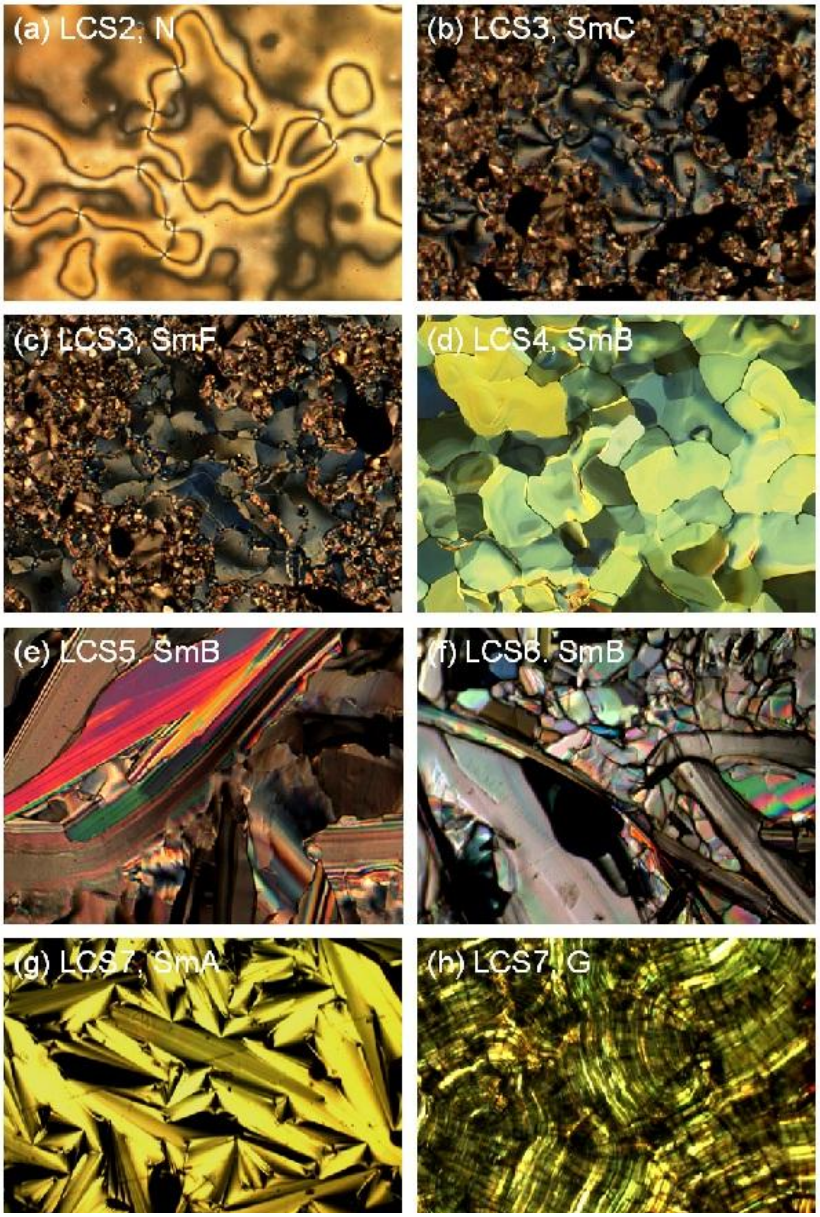

Figure 2.13 POM pictures of LCS2 to LCS7. (a) Nematic Schlieren texture of LCS2 at 177 ℃. (b) SmC fan-shaped + schlieren texture of LCS3 at 87 ℃. (c) SmF fan-shaped + mosaic-schlieren texture of LCS3 at 80 ℃. (d) SmB mosaic texture of LCS4 at 160 ℃. (e) SmB mosaic texture of LCS5 at 80 ℃. (f) SmB mosaic texture of LCS6 at 178 ℃. (g) SmA fan-shaped texture of LCS7 at 240 ℃. (h) G arced-fan texture of LCS7 at 170 ℃.

The phase change behavior of LCS1 through LCS7 is summarized in Figure 2.14. The phase transition temperature is recorded as the endpoint of texture change under POM. In general, the POM transition temperatures agree well with the DSC data.

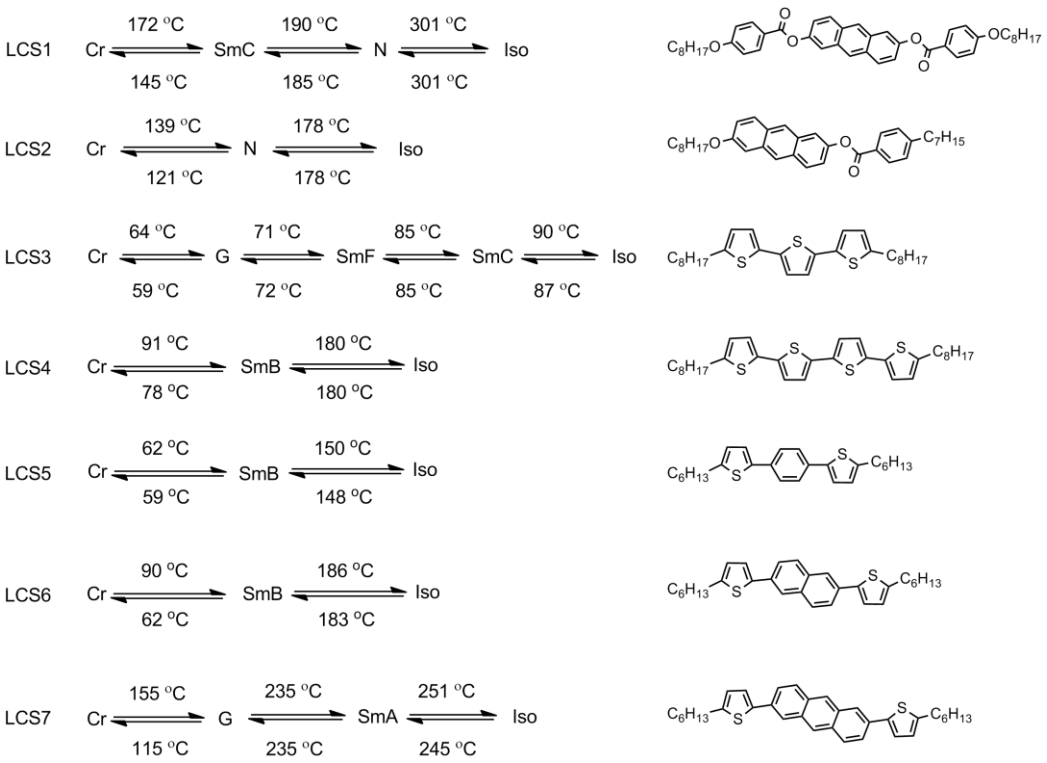

Figure 2.14 Phase transition temperature of liquid crystalline semiconductors.

Liquid crystal is a delicate state of matter and its phase change behavior is very sensitive to molecular structure. For example, LCS3 and LCS5 are very similar in structure but they have very distinct LC phases (Figure 2.14). Nevertheless, several guidelines can be generalized for the design of liquid crystals. First, symmetrical molecules are likely to have smectic phases while unsymmetrical molecules tend to have nematic phases (LCS2). Second, the melting temperature often increases rapidly with core size (LCS5, LCS6, LCS7). Last, LCs with alkoxy side chain are prone to having tilted smectic phases.[44] For example, a SmC phase was observed in the alkoxy-subsitituted LCS1.

Chapter 3: Electrical Measurement of Liquid Crystalline Semiconductors

This chapter details the characterization of the carrier mobility of liquid crystalline semiconductors by the space-charge limited current (SCLC) method[57, 58] and the field-effect transistor (FET) method.[59] The SCLC method requires simple experimental setup and gives high sensitivity, while the FET method gives more meaningful results from the perspective of application.

3.1 SCLC Method

Organic semiconductors typically have a band gap around 3 eV, and hence behave much like insulators. Nevertheless, when an organic semiconductor is sandwiched between two metal contacts and a voltage is applied across the sample (Figure 3.1), a small current will flow through:

$$j = j_{ohm} + j_{SCL} = \frac{n_0 q \mu}{L} V + \frac{9}{8} \frac{\varepsilon_r \varepsilon_0 \mu}{L^3} V^2 \tag{3.1}$$

where n_0 is the carrier density, L is sample thickness, V is voltage, ε_0 is vaccum permittivity, ε_r is relative permittivity (dielectric constant), and μ is mobility. The space-charge limited current j_{SCL} is associated with the injection of carriers from metal electrodes into the semiconductor. A relevant phenomenon is a cathode ray, which can be viewed as electron injection into vaccum.

The ohmic current j_{ohm} is the drift current of the intrinsic carriers in the sample, and in many cases this term is small and can be neglected. Therefore, one can calculate the mobility from the slope of J-V^2 curve:

$$\mu = \frac{8L^3}{9\varepsilon_r \varepsilon_0} \frac{dJ}{d(V^2)} \tag{5.1}$$

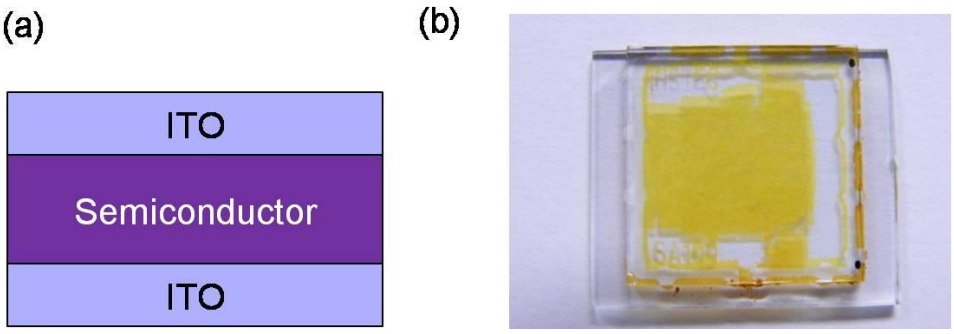

Figure 3.1 (a) Metal-semiconductor-metal structure for SCLC measurement. ITO: indium tin oxide. (b) Picture of a LC cell with ITO electrodes filled with the quarterthiophene LCS4.

Experimental. A liquid crystal cell with ITO top and bottom electrode was purchased from Instec (Boulder, CO). The ITO electrode area was 1cm^2 and the cell gap was 4 μm. A melted liquid crystal was loaded into the cell in the isotropic state or nematic state, facilitated by capillary force. After filling, the cell was cooled to room temperature at a rate of 1-3 °C/min. I-V characteristics were measured on a Cascade Microtech 11000 probe station using an Agilent 4155C precision semiconductor parameter analyzer under ambient atmosphere. The probe station is equipped with either a temperature control system or a built-on hot plate. The dielectric constant ε_r was assumed to be 4 for all the LCSs (literature value: pentacene, 3.3-3.9[60]).

Figure 3.2(a) shows the J-V curve of LCS2 at 100 °C (crystalline state). The J-V curve can be fitted well by the SCLC equation with an apparent mobility of 3×10^{-7} cm^{2}V^{-1}s^{-1}. The low mobility may be the result of non-optimal material design and the large Schottky barrier at the metal-semiconductor interface. Figure 3.2(b) shows a set of J-V curves measured at different temperatures, in both the crystalline (Cr) and the liquid crystalline (LC) phases. In the Cr phase, the current showed a strong thermally activated behavior, while in the LC phase, the current became much less dependent on temperature. At the Cr to N transition, the current increased rapidly by several fold. The current for LCS1

showed a similar increase at the Cr to SmC transition (Figure 3.2c). The mobility increase is consistent with better self-organization and reduction of grain boundary barriers in the LC phase.

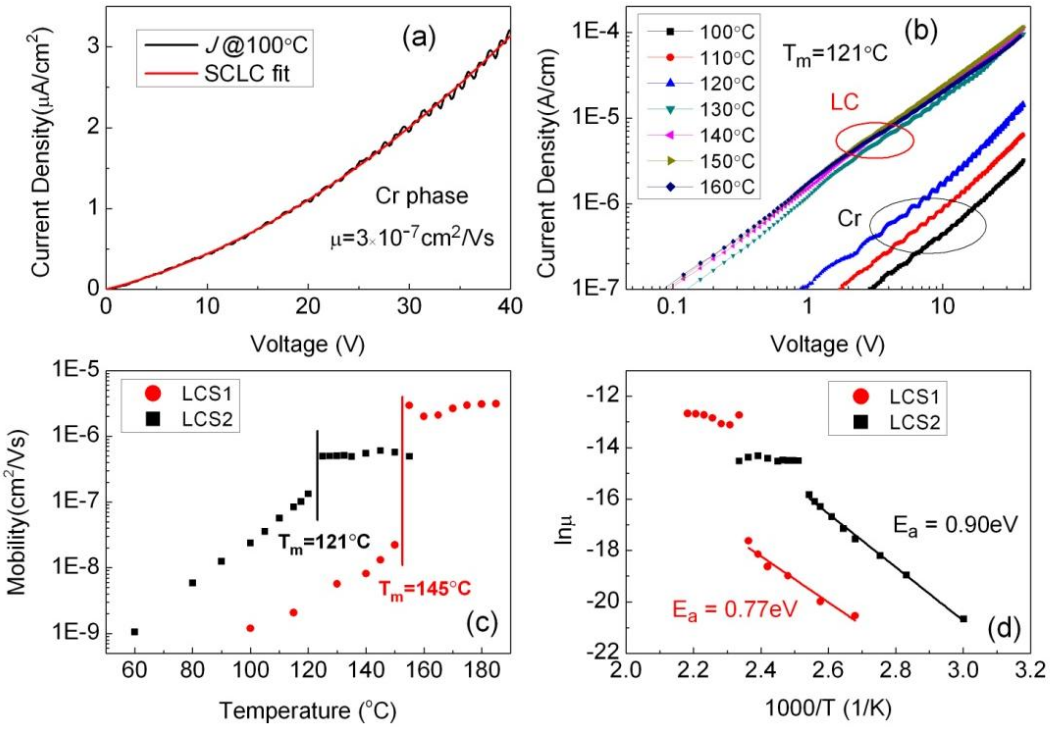

Figure 3.2 SCLC measurement of LCS1 and LCS2. (a) J-V curve at 100 ℃ and SCLC fit of LCS2. The fluctuation in current was due to temperature variation. (b) J-V curves of LCS2 in crystalline and liquid crystalline state. (c) Calculated SCLC mobility of LCS1 and LCS2 versus temperature. (d) Arrhenius plot of mobility for LCS1 and LCS2.

The activation energy of the mobility in Cr phase was 0.77eV and 0.90 eV for LCS1 and LCS2 respectively (Figure 3.2d). A large part of the activation energy may come from the Schottky barrier between the ITO and the semiconductor, which is calculated to be 0.53 eV and 0.49eV for LCS1 and LCS2, respectively (ϕ_M=4.8eV for ITO, see Appendix B for calculation details). The rest of the activation energy may come from the grain boundary barriers inside the semiconductor. Interestingly, the apparent mobility (current)

is almost constant inside the LC phase. It is known that the order parameter of LC decreases with temperature in LC phase[44], which may counteract the current increase due to better thermionic emission at the Schottky barrier. Alternatively, the barrier width in LC phase may reduce and allow efficient Fowler-Nordheim tunnelling, thus showing a nearly ohmic contact.

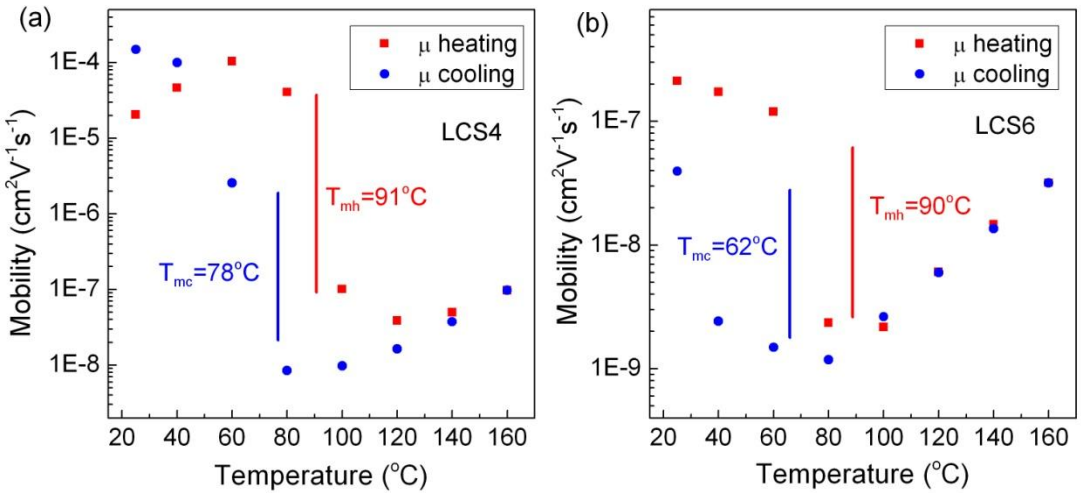

Figure 3.3 (a) SCLC mobility of LCS4 versus temperature. T_{mh}: melting point (Cr→SmB phase) upon heating, T_{mc}: freezing point upon cooling (SmB→Cr phase); (b) SCLC mobility of LCS6 versus temperature.

The other LC semiconductors behave differently in their LC mobility. Figure 3.3 shows the change of SCLC mobility versus temperature and phase change for LCS4 and LCS6. In contrast to LCS1 and LCS2, the mobility drops near the LC phase transition for these two semiconductors. The mobility was tested both in a heating run and a cooling run; the hysteresis of mobility change corresponds very well to the phase change for LCS4. The mobility change misaligns with the phase transition temperature in LCS6, which may be caused by a pre-transition effect[61] or supercooling. For LCS4, the mobility exceeds the initial value after cooling back to room temperature, while for LCS6, the mobility drop was only partially recoverable. Therefore, a melting-cooling cycle does not always

improve mobility and care should be taken in any attempt to improve mobility by thermal annealing.

It is interesting that we observed different mobility changes upon phase transition for different LCs. One possible reason is the difference in LC phases and alignment behavior. When a crystal melts into a liquid crystal, two counteractive changes happen：the overall orientational and positional order decrease, which negatively influences mobility, and the size of grain (domain) may increase, which enhances mobility. The net effect will depend on which of the two mechanisms dominates. For LCS1 and LCS2, they have a nematic phase and the flow during the filling process of LC cell easily aligns them into large domains (Figure 3.4a), and therefore the mobility in LC phase benefits very much from the reduction in grain boundary density. The smectic LCS4 and LCS6 are much harder to align; they form mosaic texture with domain boundaries even inside LC cell (Figure 3.4b). Therefore, the net result of LC phase change is a mobility drop due to decrease in molecular order. The thermal activated behavior inside LC phase (Figure 3.3) also suggests that there are remaining domain boundaries inside the LC phase of LCS4 and LCS6.

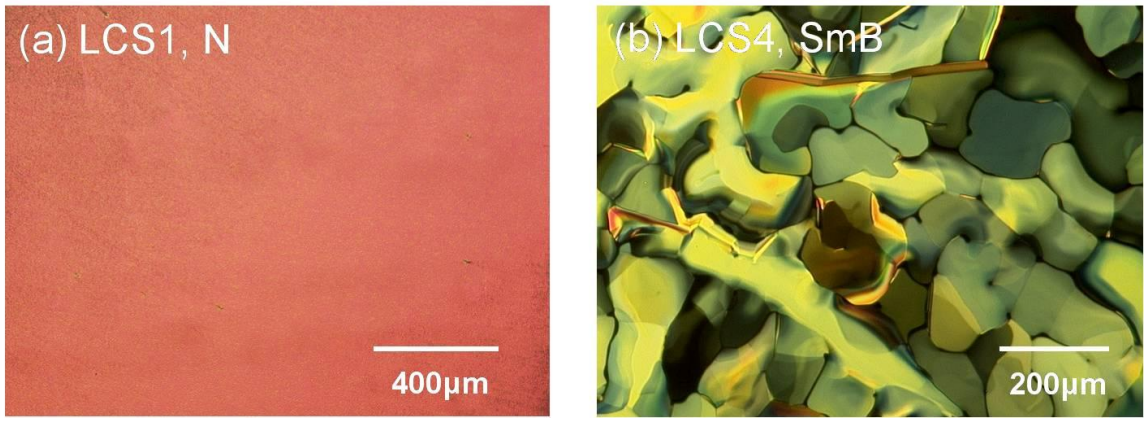

Figure 3.4 (a) POM image of LCS1 inside LC cell, which shows a monodomain larger than 1mm^2; (b) POM image of LCS4 inside LC cell.

Another possible issue is that the voltage applied during the measurement may change the orientation of LC molecules. Considering LC molecules as rods, the preferred orientation in the SCLC measurement configuration is planar alignment, i.e., the long-axis of the molecule lies parallel to the electrode plane. The POM images in Figure 3.4 suggest that the LCs adopt a planar orientation under zero field. The orientation of LC molecules under electric field depends on the dielectric anisotropy of the LC molecules, with the induced electric dipoles aligning parallel to the electric field. If the induced dipole is along the long-axis of the LC molecule, then the molecule may align perpendicular to the electrode plane under electric field. Perpendicular alignment in the SCLC cell is unfavorable for charge transport because the more insulating alkyl chains on the ends of the molecule. The configurations of LCS1 through LCS7 under electric field are still unknown, and POM imaging under electric field will greatly clarify this issue.

3.2 FET Method

SCLC method is a simple way to characterize the mobility of organic semiconductors but it has several limitations. First, the commercially available LC cell uses low work function ITO electrodes, which often forms an injection barrier with organic semiconductors and lowers the apparent mobility. Second, the dielectric constant is anisotropic for LCs and also temperature-dependent[61]. Therefore, mobility calculations based on constant dielectric constant assumption, although widely adopted in literature, are not rigorously valid. Last, SCLC measurement may have large variation from sample to sample.[62] Therefore, we fabricated thin-film transistors with LCS as an alternative method to characterize mobility.

Figure 3.5 shows the device structure of top-contact and bottom contact thin-film transistors. The source-drain contacts can be patterned either after the deposition of organic semiconductors (top-contact) or before the OSC deposition (bottom-contact). For LCS-OFETs, bottom-contact devices are preferred because of the fluid-like behavior of LCs; however, top-contact devices can also be used for soft crystal phase materials.

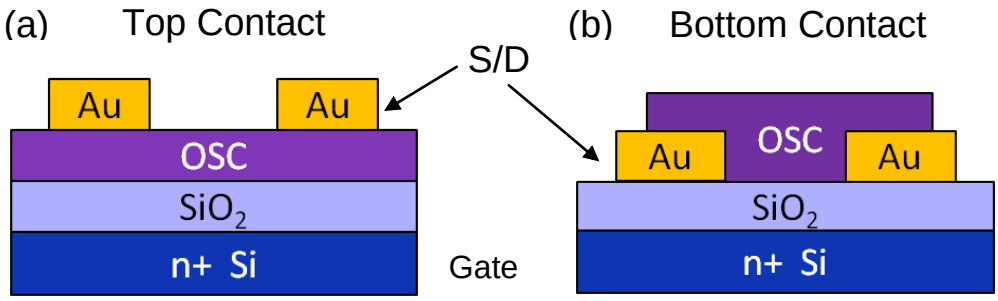

Figure 3.5 Device structure of (a) top-contact transistor and (b) bottom contact transistor. OSC: organic semiconductors. S/D: source/drain contact.

Organic thin-film transistors operate in the accumulation regime, and their I-V characteristics can be approximated using the following equations:

linear regime: $I_{DS} = \frac{\mu C_i W}{L}(V_{GS} - V_T - \frac{V_{DS}}{2})V_{DS}$, when $|V_{DS}| \leqslant |V_{GS}\text{-}V_T|$ (5.1)

saturation regime: $I_{DS} = \frac{\mu C_i W}{2L}(V_{GS} - V_T)^2$, when $|V_{DS}| > |V_{GS}\text{-}V_T|$ (5.1)

where I_{DS} is drain-source current, μ is mobility, C_i is the capacitance per unit area of gate dielectic, W is channel width, L is channel length, V_{GS} is gate-source voltage, V_{DS} is drain-source voltage, and V_T is the threshold voltage. Mobility can be calculated in the saturation regime according to the following equation:

$$\mu = \frac{2L}{C_i W}\left(\frac{\partial\sqrt{I_{DS}}}{\partial V_{GS}}\right)^2 \quad (5.1)$$

OFET fabrication. The fabrication of bottom-contact transistors was described as follows. N-type silicon wafer (resistivity 1-10 Ω·cm) was chosen as the gate electrode, and 230 nm SiO_2 was grown by thermal oxidation as the gate dielectric. The SiO_2 on the back of the wafer was removed by buffered oxide etch with photoresist protection of the top SiO_2 layer. After removal of the photoresist, the SiO_2 was treated in several different methods. For hexamethyldisilazane modification (HMDS-SiO_2), the wafer was exposed to HMDS vapor at 150˚C for 5 min. For octadecyltrichlorosilane (OTS)-modification, the wafer was immersed in 90 mM OTS + 0.5M triethylamine (TEA) in toluene for 30min, rinsed with toluene, acetone, and IPA, and dried. Gold S/D electrodes were formed either by thermal evaporation through a shadow mask or by photolithography. For pentafluorobenzenethiol (PFBT) modification of gold, the wafer was treated with 10mM PFBT for 10 min, rinsed with toluene, and dried. The solution organic semiconductors were deposited using a drop casting technique. Typically, a 2 wt% solution of organic semiconductor was dropped onto the wafer and evaporated slowly to form a film covering the channel region as well as part of the source/drain electrode. The wafer was then baked at 90°C for 2 min to remove the residual solvent.

Top contact devices were fabricated using the same SiO_2/Si substrate. The SiO_2 surface was treated with HMDS or coated with a thin layer of polystyrene (PS-SiO_2) or polyimide (PI-SiO_2). PS-SiO_2 was prepared by spin-coating a 2 wt% PS solution in xylenes and baking at 90˚C for 5min. The PS film thickness was determined to be 47 nm by ellipsometry. PI-SiO_2 was prepared by spin-coating 2.5 wt% Nissan polyimide SE-1211 in cyclopentanone and imidizing at 200˚C for 1h. The PI thickness was 41 nm. The unit area capacitance for the HMDS-SiO_2, PS-SiO_2, and PI-SiO_2 was calculated to be 15.0 nF/cm^2, 11.3 nF/cm^2, and 10.6 nF/cm^2, respectively. The organic semiconductor was deposited by thermal evaporation at a pressure of 5×10^{-5} torr at a rate of ~0.05 nm/s, with the wafer substrate at room temperature. The thickness of the semiconductor was about 40 nm. Afterwards, 50 nm-thick gold source/drain electrodes were deposited by thermal evaporation through a shadow mask. The devices were measured under ambient atmosphere.

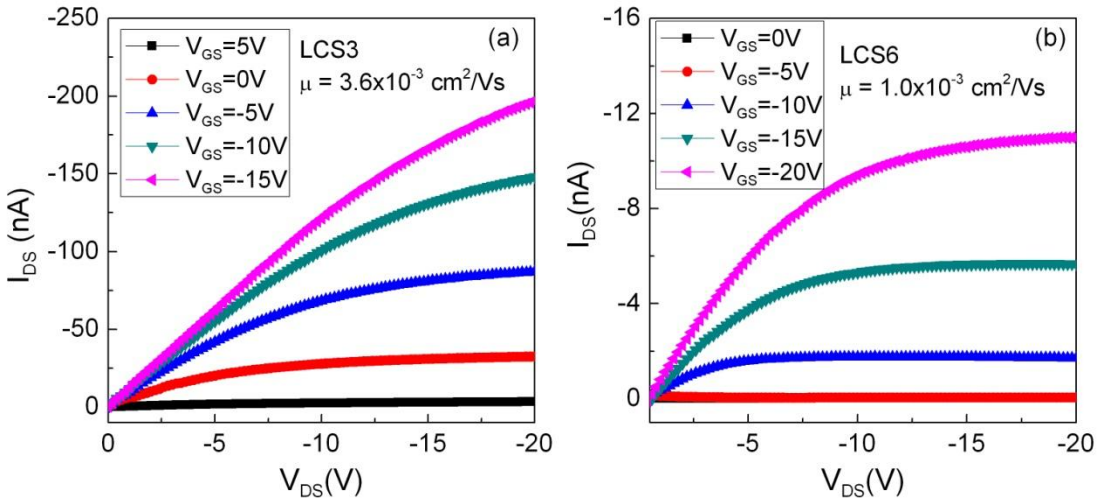

Figure 3.6 Output characteristics of transistors with (a) LCS3 and (b) LCS6 in crystalline phase. The organic semiconductors were drop-casted on HMDS-treated SiO_2 and PFBT-treated Au. Electrical measurements were performed at room temperature and ambient atmosphere.

First, device fabrication conditions were screened, including dielectric modifications, electrode modifications, casting solvents, etc. A standard solution-processible organic semiconductor, 6,13-bis(triisopropylsilylethynyl)pentacene (TIPSP)[63, 64] was tested for reference. Figure 3.6 shows the output characteristics of LCS3 and LCS6. The transistor output curve showed good saturation and p-type behavior, with negative gate voltage inducing the source-drain current. Note that the FET mobility of LCS6 (1.0×10^{-3} $cm^2V^{-1}s^{-1}$) is much higher than its SCLC mobility (2.1×10^{-7} $cm^2V^{-1}s^{-1}$, Figure 3.3b), which may be the result of improved carrier injection from Au electrode instead of from ITO electrode in the SCLC cell.

Table 3.1 summarizes effect of transistor fabrication parameters on mobility. The best mobility for TIPSP was achieved with HMDS-modified SiO_2 and PFBT-modified Au (2.8×10^{-2} $cm^2V^{-1}s^{-1}$), and therefore, this device fabrication condition was used for LCS transistors. The casting solvent for solution-processed organic transistors affects the device performance significantly. Several parameters may affect the choice of solvent: boiling point, solubility of organic semiconductors, and wettability with substrates. Generally, high boiling point (bp) solvents, such as chlorobenzene and dichlorobenzene, are preferred to allow slow evaporation and growth of better crystals. However, solvents with very high bp such as tetralin may leave residual solvent in the film and degrade device performance (Entry 1 and 2 in Table 3.1). Among the solvents we tested, chlorobenzene was the best solvent for TIPSP and LCS3 (Entry 6, 9), while dichlorobenzene was slightly better than chlorobenzene for LCS6 (Entry 12, 13). Dichlorobenzene was also the best solvent for the sparingly soluble semiconductor LCS7 (Entry 16). Film deposition by thermal evaporation instead of solution processing offers much better performance for this semiconductor (Entry 17-19).

	Material	Geometry	Dielectric	S/D	Solvent	Mobility (cm^2/Vs)
1	TIPSP	BC	SiO_2	Au	tetralin	9.0×10^{-4}
2	TIPSP	BC	SiO_2	Au	toluene	3.6×10^{-3}
3	TIPSP	BC	OTS-SiO_2	Au	toluene	3.4×10^{-3}
4	TIPSP	BC	OTS-SiO_2	PFBT-Au	toluene	2.1×10^{-3}
5	TIPSP	BC	HMDS-SiO_2	PFBT-Au	toluene	9.6×10^{-3}
6	TIPSP	BC	HMDS-SiO_2	PFBT-Au	PhCl	2.8×10^{-2}
7	TIPSP	BC	HMDS-SiO_2	PFBT-Au	$PhCl_2$	1.2×10^{-2}
8	LCS3	BC	HMDS-SiO_2	PFBT-Au	toluene	5.5×10^{-4}
9	LCS3	BC	HMDS-SiO_2	PFBT-Au	PhCl	3.6×10^{-3}
10	LCS4	BC	HMDS-SiO_2	PFBT-Au	$PhCl_2$	8.1×10^{-5}
11	LCS5	BC	HMDS-SiO_2	PFBT-Au	toluene	2.5×10^{-5}
12	LCS6	BC	HMDS-SiO_2	PFBT-Au	PhCl	1.0×10^{-3}
13	LCS6	BC	HMDS-SiO_2	PFBT-Au	$PhCl_2$	1.4×10^{-3}
14	LCS7	BC	HMDS-SiO_2	PFBT-Au	toluene/$CHCl_3$	1.4×10^{-5}
15	LCS7	BC	HMDS-SiO_2	PFBT-Au	$PhCl_3$/$CHCl_3$	3.4×10^{-5}
16	LCS7	BC	HMDS-SiO_2	PFBT-Au	$PhCl_2$	9.6×10^{-4}
17	LCS7	TC	HMDS-SiO_2	Au	evaporation	2.8×10^{-2}
18	LCS7	TC	PS-SiO_2	Au	evaporation	7.3×10^{-2}
19	LCS7	TC	PI-SiO_2	Au	evaporation	1.0×10^{-1}

Table 3.1 Screening of transistor fabrication. BC: bottom-contact, TC: top-contact, PhCl: chlorobenzene, $PhCl_2$: 1,2-dichlorobenzene, $PhCl_3$: 1,2,4-trichlorobenzene.

We evaluated the FET mobility of several LC semiconductors in their LC phases. Figure 3.7 shows the output and transfer characteristics for LCS3 in both crystalline and liquid crystalline phase. At room temperature where LCS3 was in crystalline phase, the

transistor had nearly standard output curves with a mobility of 1.8×10^{-3} $cm^2V^{-1}s^{-1}$. When it was heated to 67 °C and LCS3 entered the soft crystal G phase (Figure 2.14), the mobility dropped by more than one order of magnitude to 8.7×10^{-5} $cm^2V^{-1}s^{-1}$. Heating into higher temperature smectic F phase at 75 °C caused an additional slight drop in mobility to 6.0×10^{-5} $cm^2V^{-1}s^{-1}$. In the meanwhile, the output curves became less standard and lost saturation. Figure 3.8 plots the mobility change with temperature and phase transition. It is confirmed that mobility dropped near the vicinity of phase transition, and the hysteresis due to supercooling was also seen. The mobility drop was largely reversible after a cooling run to room temperature. The reversibility indicates that the mobility drop in LC phase is likely to stem from change in molecular ordering rather than irreversible chemical oxidation.

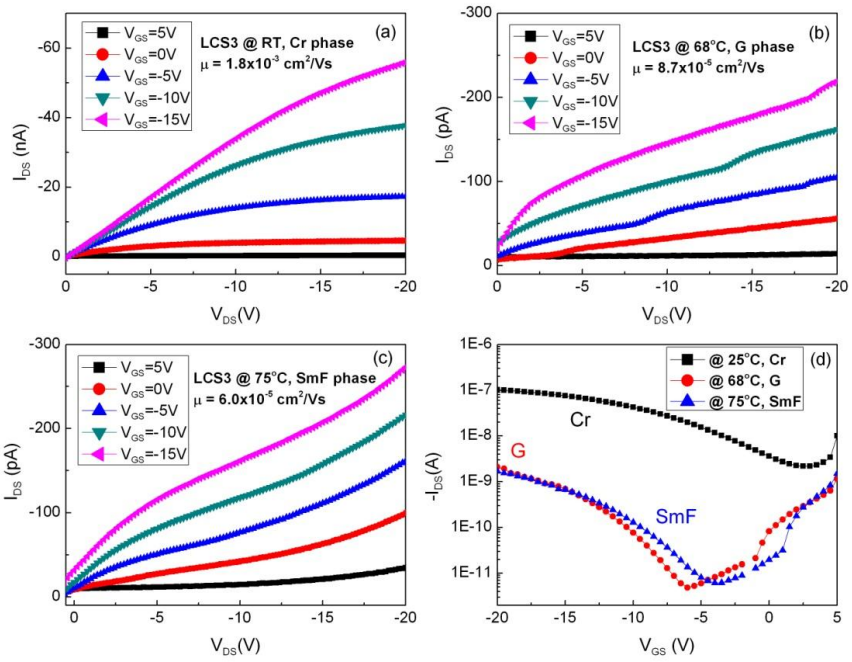

Figure 3.7 Transistor performance of LCS3 at different temperatures. (a) Output characteristics at 25°C, in crystalline phase. (b) Output characteristics at 67°C, in soft crystal G phase. (c) Output characteristics at 75°C, in smectic F phase. (d) Transfer characteristics (at V_{DS} = -20V) at 25°C, 67°C, and 75°C.

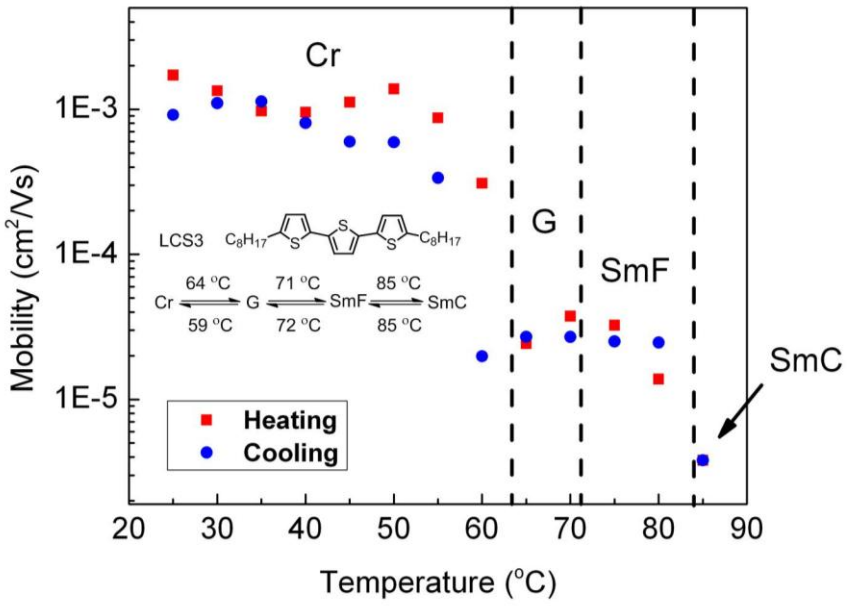

Figure 3.8 FET mobility of LCS3 versus temperature in a heating run (red squares) and a cooling run (blue dots).

We also tested the FET mobility of LCS4, LCS6 and LCS7. For these semiconductors, transition into the LC phase was concomitant with complete loss of field-effect current, i.e., mobility dropped to zero in the LC phase (Figure 3.9a-f). The FET behavior of LCS7 reappeared when the semiconductor was cooled from LC phase back to Cr phase, although the mobility was only partially recoverable (Figure 3.9g, h). The mobility of the original device in Figure 5e was 0.10 $cm^2V^{-1}s^{-1}$, and after the phase transition cycle and electrical measurement, the mobility of the device dropped to 0.024 $cm^2V^{-1}s^{-1}$. We notice that the mobility of an adjacent device without extensive electrical measurement during LC phase recovered to 0.050 $cm^2V^{-1}s^{-1}$ (Figure 3.10). The better recovery suggests that electric field may disrupt the molecular ordering in LC phase or electrochemically degrade the LCS, contributing to the degradation of mobility in LC phase.

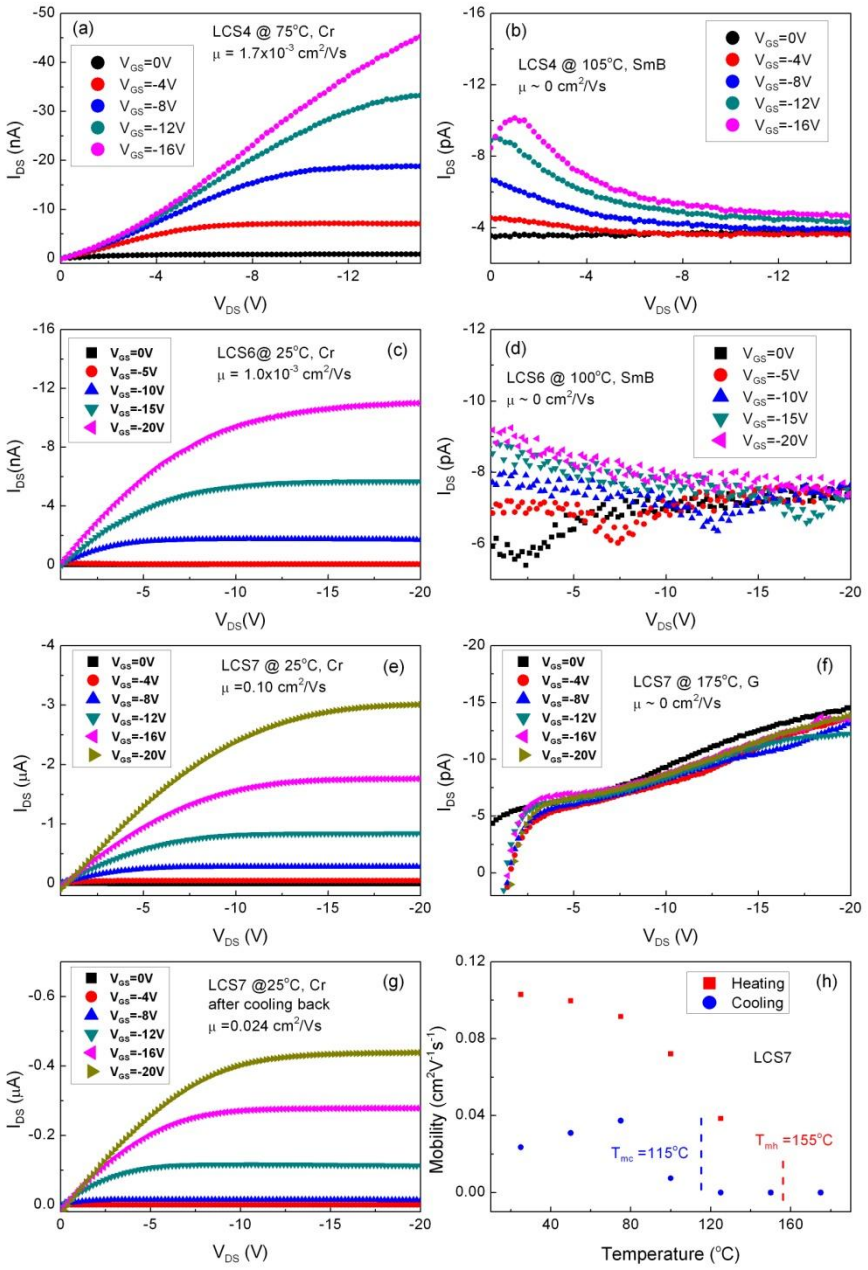

Figure 3.9 OFETs measured in Cr and LC phase. (a) LCS4 in Cr phase. (b) LCS4 in SmB phase. (c) LCS6 in Cr phase. (d) LCS6 in SmB phase. (e) LCS7 in Cr phase. (f) LCS in G phase. (g) LCS7 in Cr phase, cooled back from LC phase. (h) Mobility-temperature plot of LCS7.

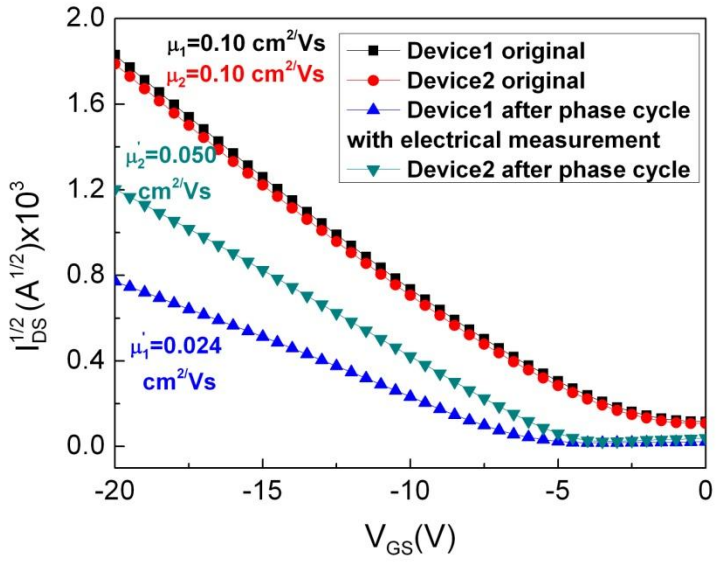

Figure 3.10 Transfer characteristics of LCS7 OFETs at room temperature. Device 1 and device 2 have very close initial mobility values. After thermal cycling, the electrically more stressed device 1 dropped to lower mobility.

Chapter 4: Patternable DNA-Conjugation Polymers for DNA-Guided Self-Assembly

4.1 DNA-Guided Self-Assembly

DNA is an essential molecule for life. With very few exceptions, all forms of life store, replicate, and pass on their genetic information in the form of DNA. Structurally, DNA has a backbone of deoxyribose phosphodiester; the genetic information is stored in the sequence of four different bases: adenine (A), guanine (G), cytosine (C) and thymine (T). The bases are attached to the deoxyribose by N-glycosidic bond (Figure 4.1a).

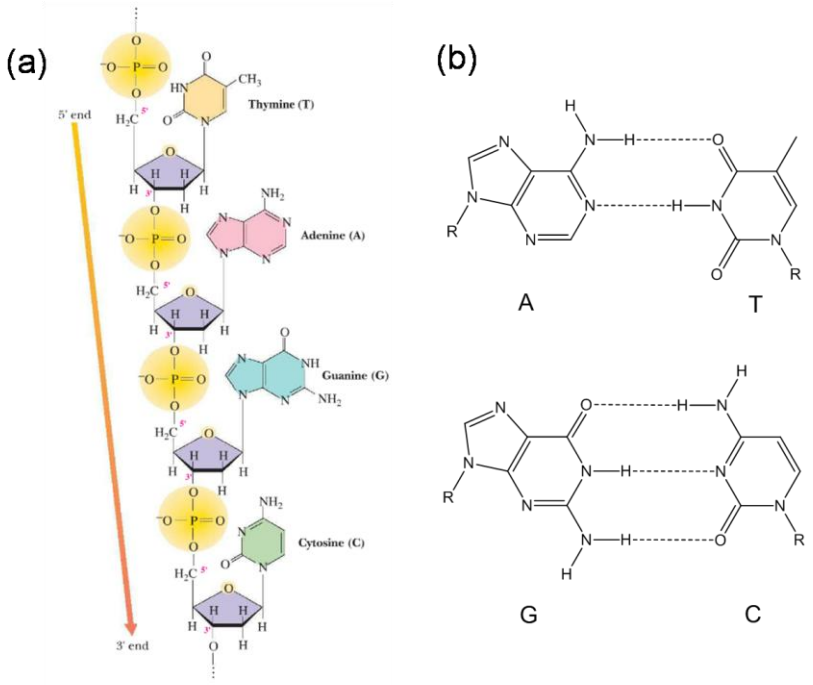

Figure 4.1 Structure of DNA. (a) DNA is a macromolecule composed of deoxyribose, bases, and phosphate. *Reproduced by permission from BROWN/FOOTE/IVERSON. Instructor's Edition for Brown/Foote/Iverson's Organic Chemistry, 4th, 4E. © 2005 Brooks/Cole, a part of Cengage Learning, Inc.* (b) Base pairing of A and T, G and C via hydrogen bonding.

In the double helical structure of DNA, each base forms a pair with its complement by hydrogen bonding. As shown in Figure 4.1b, adenine pairs with thymine with two hydrogen bonds, while guanine pairs with cytosine with three hydrogen bonds. The G-C pair is thermodynamically more stable than the A-T pair. Therefore, DNA with higher G-C content forms a more stable duplex. The stability of double-strand DNAs will be revisited in Chapter 5.

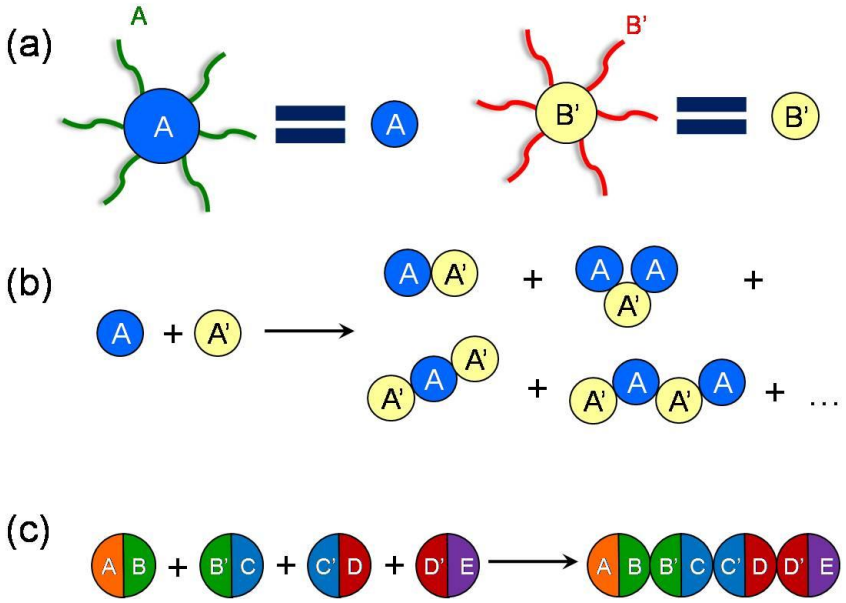

Figure 4.2 DNA-guided self-assembly. (a) Different particles can be coated with different DNA strands. (b) Isotropic coating of particles with complementary DNA strands can lead to mixed aggregates with alternating particle arrangements. (c) Janus particles with different DNAs on opposite surface can assemble into a specific sequence.

The high specificity of DNA base pairing provides a very useful tool for self-assembly. The work of "DNA origami"[24] demonstrated that a long DNA strand can be folded into almost arbitrary two-dimensional (2D) shapes by binding with hundreds of different short DNA strands. The self-assembly of DNA can go beyond the biomolecule itself (Figure 4.2). Mirkin et al.[65] grafted DNA onto the surface of gold nanoparticles and assembled them into amorphous aggregates and crystals[66]. Besides high specificity, the

incorporation of DNA into the self-assembly system imparts many unique properties, including thermal reversibility[67], self-replication[68], and modulation of assembly by factors such as nucleases[69], competitive displacement[70], or photo-crosslinking[71]. These advances are beginning to herald applications in a variety of fields. For example, a diagnostic platform to detect anthrax DNA based on the color difference in assembled/isolated Au nanoparticles has been described.[72]

DNA in living organisms serves to define the sequence in which amino acids are assembled to form proteins. Bruce Merrifield won the Nobel Prize for developing the first synthetic methodology that allows chemists to accomplish this feat.[73] Scientist have sought to mimic the programmed assembly of life to create an arbitrary sequence of building blocks, for example, ABCDEFG....To accomplish the assembly of such an arbitrary sequence, each building block need to be functionalized with different DNAs on opposite faces. Such particles with two or more distinct faces are called Janus particles, named after the Roman God Janus. While the self-assembly of isotropic spheres gives amorphous aggregates or certain crystal lattices, the self-assembly of Janus particle can create a profusion of structures (for example, see Figure 1.7). Figure 4.2 illustrates the difference between the self-assembly of isotropic particles and Janus particles.

The directed self-assembly of Janus objects was demonstrated by Dr. Peter Carmichael in a magnet-encoded plastic sheet setup (Figure 4.3). Magnets were placed into predrilled holes in one-inch polycarbonate (PC) squares, and their polarity was designed to maximize the attraction between adjacent squares in the final sequence (Figure 4.2a). The PC squares were placed in a cylindrical dish containing water, and agitation was provided by an orbital shaker and the baffles in the dish. The attractive forces (magnetic) and disruptive forces (mechanical) were balanced to achieve the assembly of the programmed sequence (Figure 4.2 b to e). This magnet-polycarbonate system illustrates several elements of directed self-assembly: creation of Janus particles, design of attractive interactions, and a balance between attractive and disruptive forces.

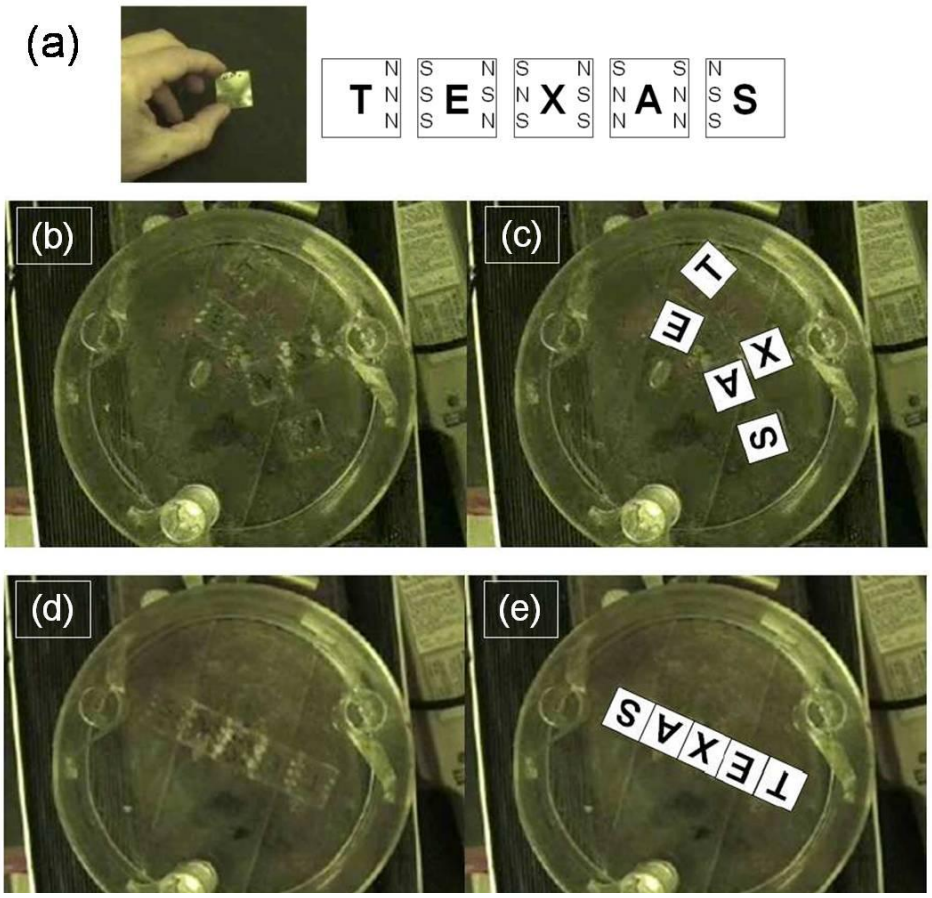

Figure 4.3 Directed self-assembly of magnet-encoded polycarbonate (PC) sheets. (a) Coding sequence of magnets on five PC squares. (b) Initial configuration of PC squares floating on water. (c) Manually labeled PC squares to show their initial position. (d) The squares assembled into a sequence after 5 minutes of shaking. (e) Manually labeled PC squares to show their final position. *Courtesy of Dr. Peter Carmichael.*

4.2 Lithography Extends the Scope of Self-Assembly

Optical lithography is the cornerstone of microelectronics industry. A modern integrated circuits (IC) chip is composed of many patterned layers of different materials, and most of the patterns are created by optical lithography. The basic process sequence of photolithography is illustrated in Figure 4.4. First, a light-sensitive material, a photoresist,

is coated on the substrate material that needs to be patterned. Light transmitted through the transparent regions of a photomask exposes selected regions of the film. The exposure changes the solubility of the photoresist. The solubility of negative photoresist is decreased by exposure. Therefore a develop step removes the unexposed region of negative photoresist and leaves the exposed region behind. For positive photoresist, solubility increases after exposure, and therefore the exposed regions are dissolved after develop and the unexposed areas are left behind. The patterned photoresist then acts as a mask for the etch process, which transfers the resist pattern into the substrate. Finally the resist is removed, leaving a relief pattern in the substrate that is a replica of the pattern on the mask.

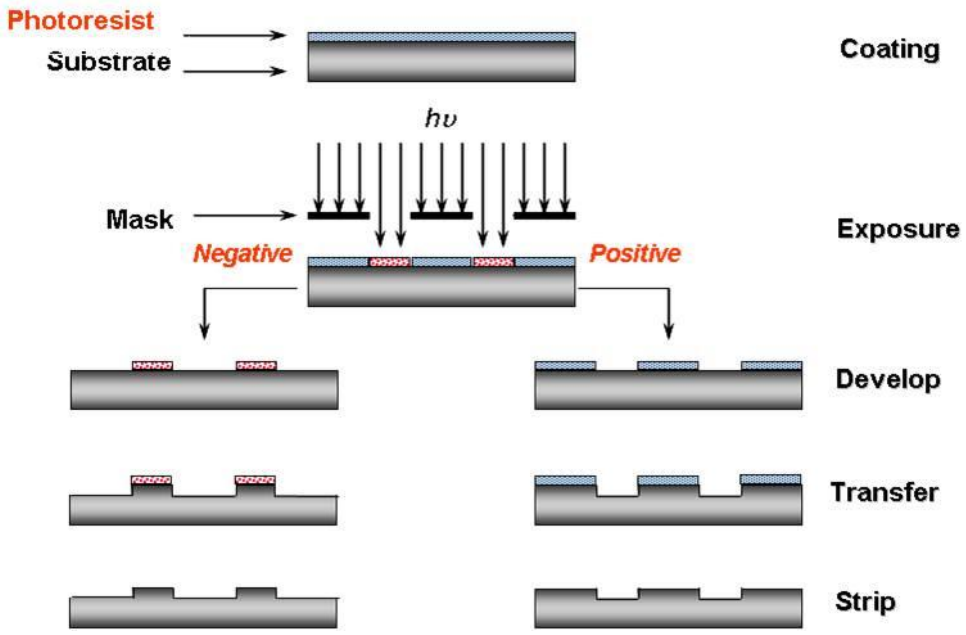

Figure 4.4 Basic photolithography process. A photoresist material has switchable solubility after light irradiation. The circuit pattern is transferred from a mask to the photoresist, and then further transferred to the layer beneath.

The incorporation of lithography into self-assembly can bring several benefits. First, lithography can print almost any quasi-3D shapes. Figure 4.5 shows several examples of shapes created by photolithography. Using photolithography, objects other than spheres

can be fabricated, which may add to the flexibility of building block design. For example, the use of cubes or rectangular prisms as building blocks should have larger contact area than spheres and thus maximizes the interaction between assembly units. Building blocks with complementary shapes can also be designed, where the self-assembly may be aided by shape-recognition.

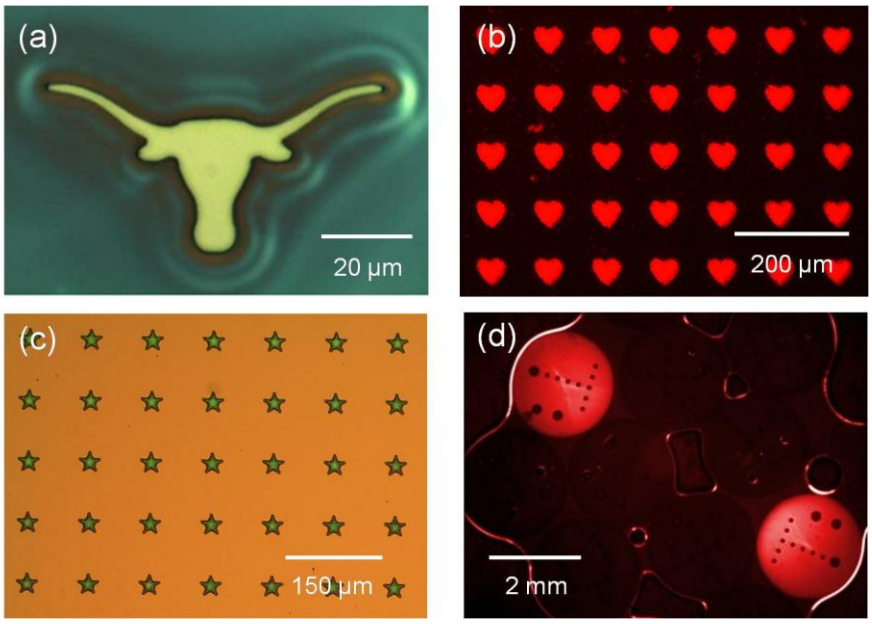

Figure 4.5 Shapes patterned by photolithography. (a) A longhorn pattern of poly(methyl methacrylate) copolymer. (b) Hearts of EPON-SU8 photoresist, doped with nile red. (c) Stars of EPON-SU8. (d) Poly (ethylene glycol)-based DNA sensor (MUFFINS, Mesoscale Unaddressed Functionalized Features INdexed by Shape)[74, 75].

Second, lithography has very high resolution and precision. The state-of-the-art photolithography process can manufacture a chip with more than a billion transistors with minimum features as small as 22 nm. Therefore, one can fabricate building blocks from nanoscale to macroscale using photolithography. Third, lithography provides potential routes to fabricate Janus particles. One of the potential routes is shown in Figure 4.6. First, a patternable, DNA-attachable polymer is spin coated onto a sacrificial lift-off layer. Then, DNA strand A is attached to the top surface of the polymer. A

photolithography step patterns one dimension of the particle and creates the side wall surface, where the second DNA strand B can be attached. Another photolithography step can create additional side wall surfaces and allow for the attachment of the third DNA strand C.

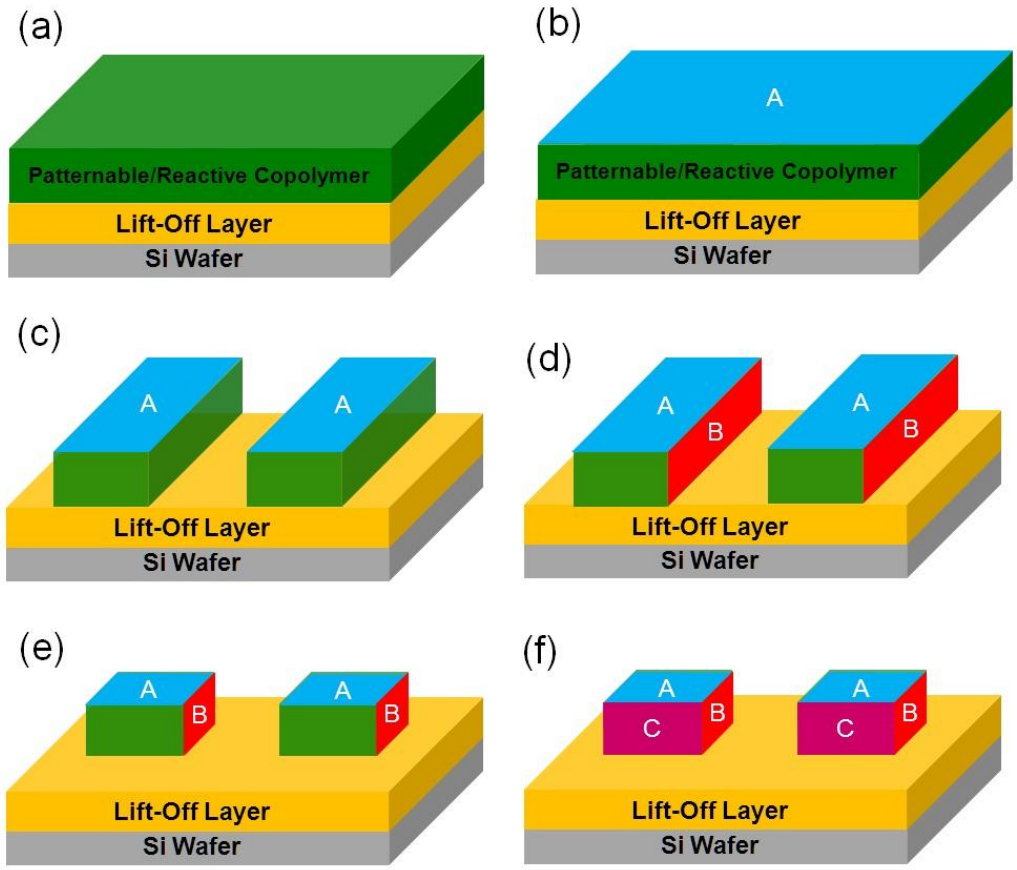

Figure 4.6 Fabrication of Janus particles using lithography. (a) Spin coating of film stack: substrate (grey), sacrificial lift-off layer (maize), reactive, photo-sensitive copolymer (green). (b) Conjugation of DNA sequence A to the top surface. (c) The first lithography step exposes the sidewall surfaces. (d) Conjugation of DNA sequence B to the sidewall surface. (e) The second lithography step exposes additional sidewall surfaces. (f) Conjugation of DNA sequence C to the newly created sidewall surface.

The above described stepwise lithography and DNA conjugation method is further extendable in several ways. A properly designed lithography and conjugation scheme can attach four different DNA strands to each of the four sidewalls of a cube. The lift-off step exposes the bottom surface and hence another possible DNA conjugation site. Furthermore, when combined with etching, Janus particles with a variety of materials can be fabricated, provided that the DNA attachment chemistry is available.

4.3 Patternable DNA-Conjugation Materials

Patternable DNA-conjugation polymers were synthesized by copolymerizing methyl methacrylate with several reactive monomers. Poly (methyl methacrylate) (PMMA) is one of the early deep-ultraviolet (DUV) photoresists and an e-beam photoresist.[76] PMMA offers the advantages of high resolution, environmental stability, and excellent film-forming properties. PMMA is a positive photoresist. Upon DUV exposure, it undergoes chain scission, leading to reduction of molecular weight and generation of small molecule products (Figure 4.7). Both mechanisms may contribute to the solubility increase of exposed polymer in organic solvents. The standard developer for PMMA is a mixture of methyl isobutyl ketone and isopropyl alcohol (MIBK: IPA).

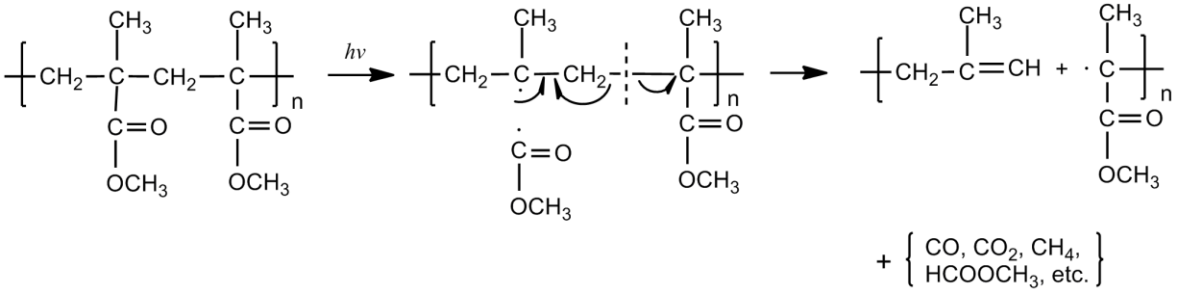

Figure 4.7 Mechanism of radiation-induced chain scission in PMMA.

Custom oligonucleotide synthesis has catapulted the progress in many areas, including DNA-guided self-assembly. Solid-phase synthesis using phosphoramidite chemistry can

synthesize DNA in up to 200 bp length with a myriad of chemical modifications and labels. The availability of amine, thiol, and azide-modified DNA enables the chemical conjugation of DNA onto a variety of substrates including polymers. Figure 4.8 shows the PMMA copolymers that bear pendant functionality designed to provide covalent linkages to modified DNAs. Glycidyl methacrylate (GMA), N-hydroxysuccinimide methacrylate (NHSMA), and pentafluorophenyl methacrylate (PFPMA) all react directly with amines; Methacrylic acid reacts with amines in the presence of condensing agent such as carbodiimide; Maleimidoethylmethacrylate (MEMA) reacts with thiols; Propargyl methacrylate reacts with azides in the presence of Cu(I) catalyst. Figure 4.9 shows the potential DNA conjugation scheme for these PMMA copolymers.

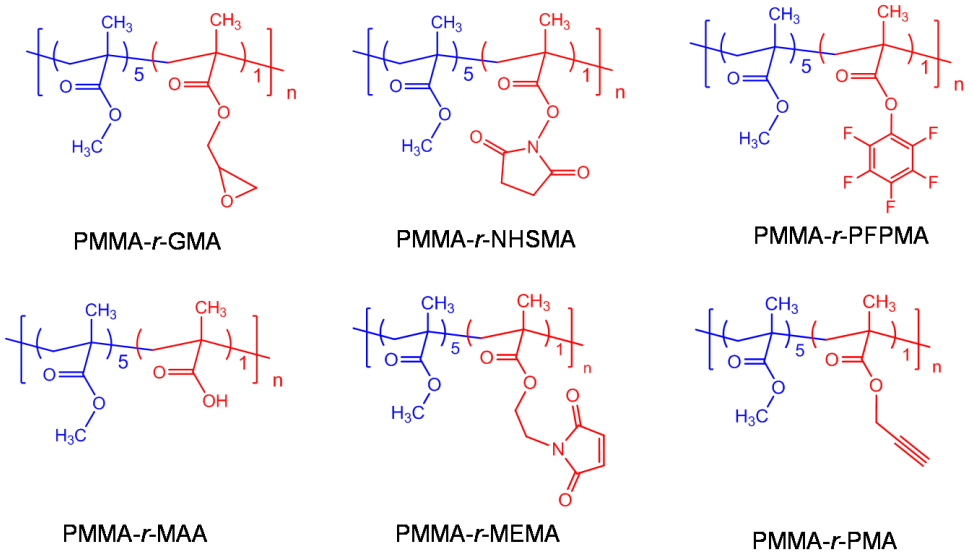

Figure 4.8 Structures of PMMA copolymers for lithographical patterning and DNA conjugation. PMMA-r-GMA: poly(methyl methacrylate-r-glycidyl methacrylate); PMMA-r-NHSMA: poly(methyl methacrylate-r-N-hydroxysuccinimide methacrylate); PMMA-r-PFPMA: poly(methyl methacrylate-r-pentafluorophenyl methacrylate); PMMA-r-MAA: poly(methyl methacrylate-r-methacrylic acid); PMMA-r-MEMA: poly(methyl methacrylate-r-maleimidoethyl methacrylate); PMMA-r-PMA: poly(methyl methacrylate-r-propargyl methacrylate) . r denotes random copolymer.

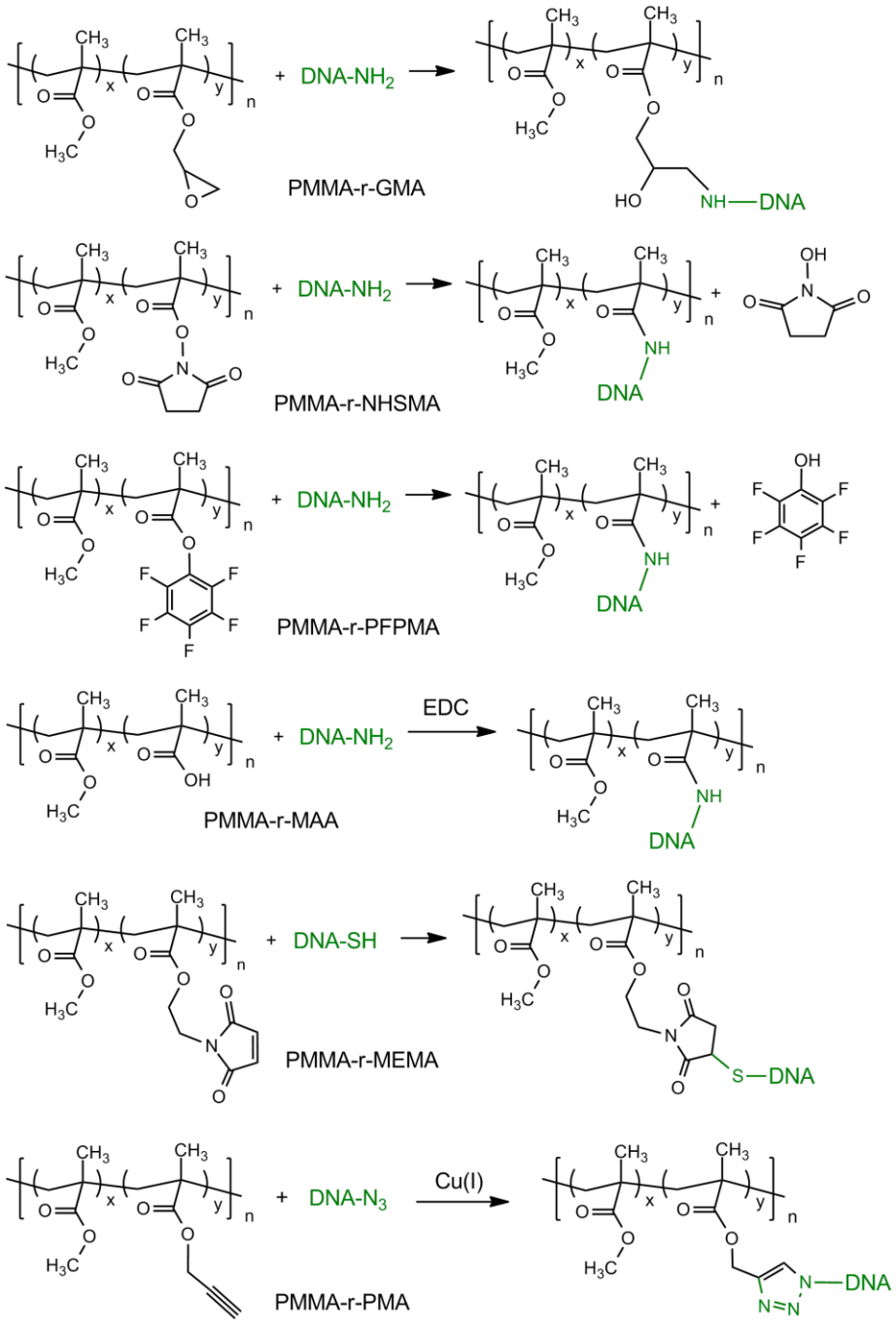

Figure 4.9 DNA-conjugation schemes for reactive PMMA copolymers.

4.4 Synthesis and Characterization of PMMA Copolymers

Figure 4.10 shows the general preparation scheme for the PMMA copolymers. The monomers MMA, GMA, MAA, and PMA are commercially available. NHSMA was synthesized from methacryloyl chloride and N-hydroxysuccinimide. PFPMA was synthesized similarly using methacryloyl chloride and pentafluorophenol. The copolymer was then prepared by free radical polymerization of MMA and the corresponding reactive monomer. The details of synthesis are described in Appendix C.

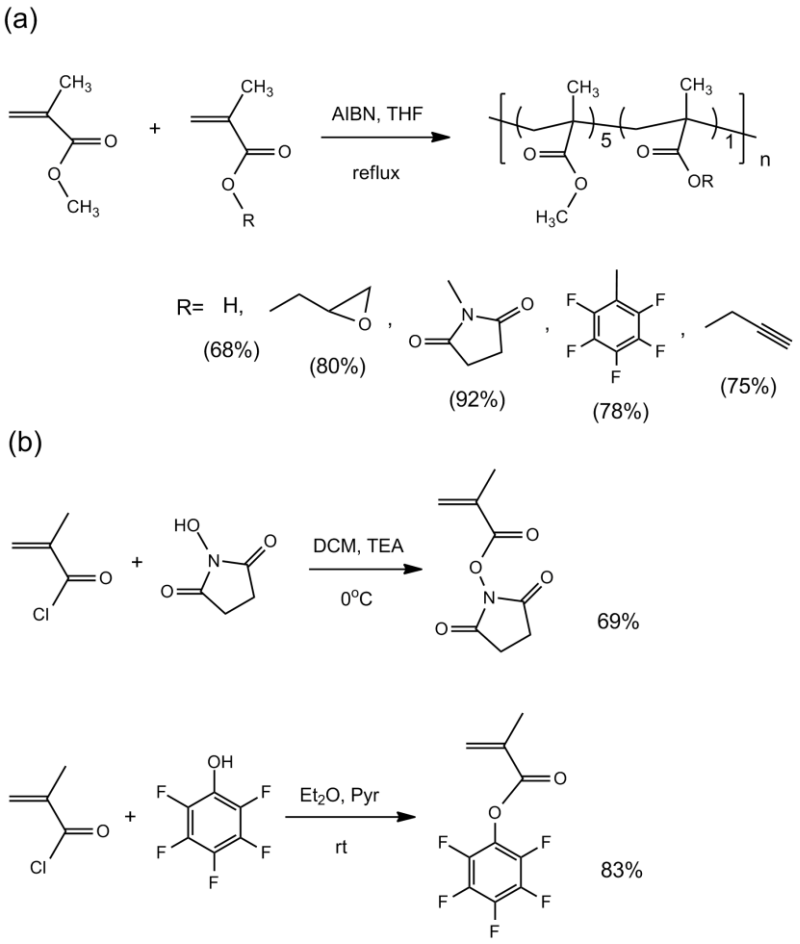

Figure 4.10 (a) General synthesis scheme of PMMA copolymers. (b) Synthesis of NHSMA and PFPMA.

Nuclear Magnetic Resonance (NMR) showed that the monomers GMA, NHSMA, PFPMA, MAA and PMA all survived radical polymerization. NMR also revealed the copolymer compositions. Molecular weights were determined by gel permeation chromatography (GPC). Table 4.1 shows the composition and molecular weight of the copolymers.

Polymer	Feed ratio	Actual Ratio	M_w	M_n	PDI
PMMA-GMA	5 : 1	4.7 : 1	103k	51k	2.02
PMMA-NHSMA	5 : 1	5.1 : 1	60k	18k	3.31
PMMA-PFPMA	5 : 1	NA	30k	16k	1.80
PMMA-MAA	5 : 1	5.2 : 1	52k	31k	1.67
PMMA-MEMA	5 : 1	5.1 : 1	48k	18k	2.61
PMMA-PMA	5 : 1	5.0 : 1	42k	18k	2.25

Table 4.1 Properties of PMMA copolymers. The actual ratio in the copolymers was determined by the integral of assigned peaks in ^{1}H NMR. The PFPMA functional group is undetectable in ^{1}H NMR.

It is known that the ethylene functionality of maleimide can be incorporated into polymer backbone by radical polymerization.[77] Therefore, the synthesis of PMMA-r-MEMA was achieved via a protection-deprotection process (Figure 4.11). Reaction of furan-protected maleic anhydride with ethanolamine gives the furan-protected maleimide (phthalimidoethanol, PE). Reaction of PE with methacryloyl chloride gives the methacrylate monomer (phthalimidoethyl methacrylate, PEMA). PEMA can be radically copolymerized with MMA to give the furan-protected prepolymer PMMA-r-PEMA. NMR confirmed that the furan-protected maleimide survived radical polymerization (Figure 4.12). Finally, PMMA-r-PEMA can be deprotected to generate the active maleimide polymer PMMA-r-MEMA via retro Diels-Alder reaction. The deprotection was near completion as evidenced by NMR (Figure 4.12).

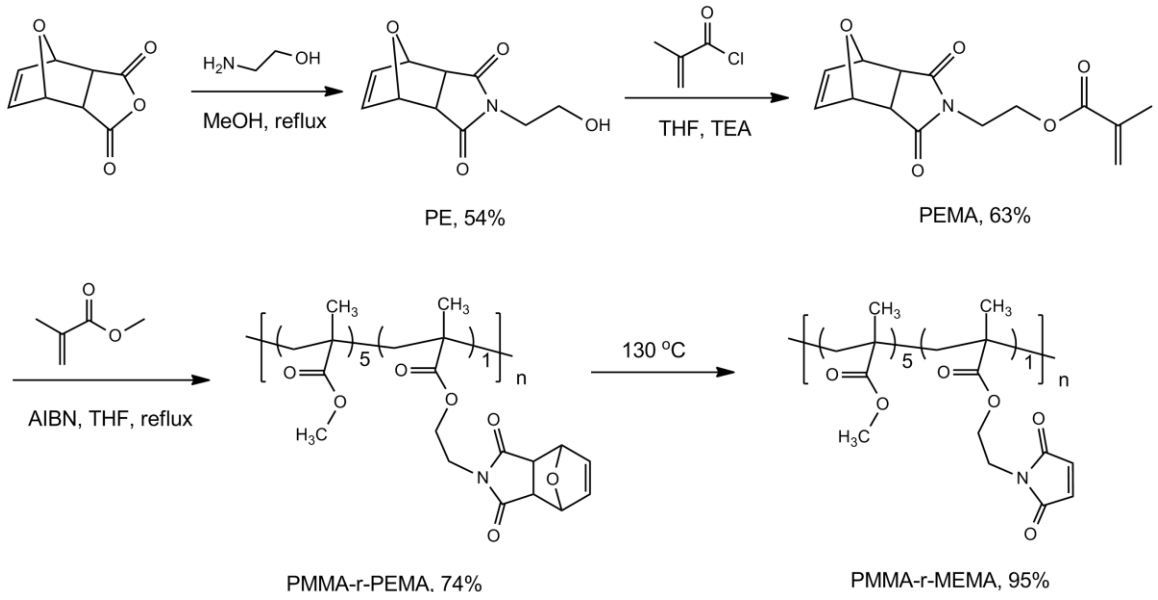

Figure 4.11 Synthesis of PMMA-r-MEMA.

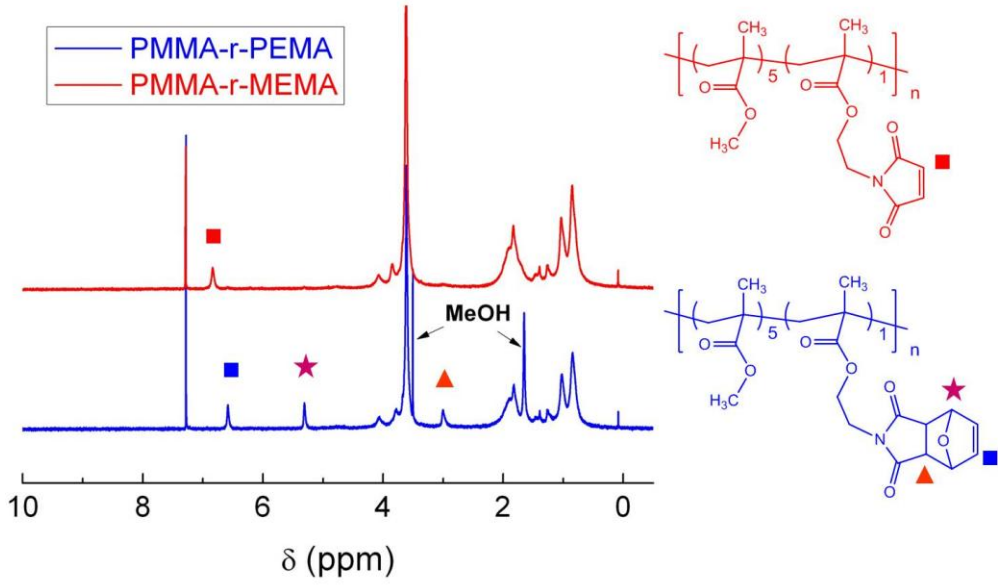

Figure 4.12 NMR spectra of PMMA-r-PEMA and PMMA-r-MEMA.

The deprotection of PMMA-r-PEMA was further studied by thermogravimetric analysis (TGA) and UV-Vis spectroscopy (Figure 4.13). The release of furan during the deprotection reaction causes a weight loss of the polymer, which can be followed by TGA (Figure 4.13a). The detected 8.6% weight loss was in good agreement with the theoretical weight loss 8.75%. Based on the TGA data, PMMA-r-PEMA can be deprotected by heating at 100°C for 2 hr or at 130°C for 20 min. The deprotection of the polymer as thin film can be followed by UV-Vis (Figure 4.13b). The conversion from PEMA to MEMA is concomitant with a decrease in absorbance near 200 nm and an increase in absorbance near 225 nm. Based on UV-Vis, the deprotection reaction was largely complete by 20 min, which is consistent with the TGA data.

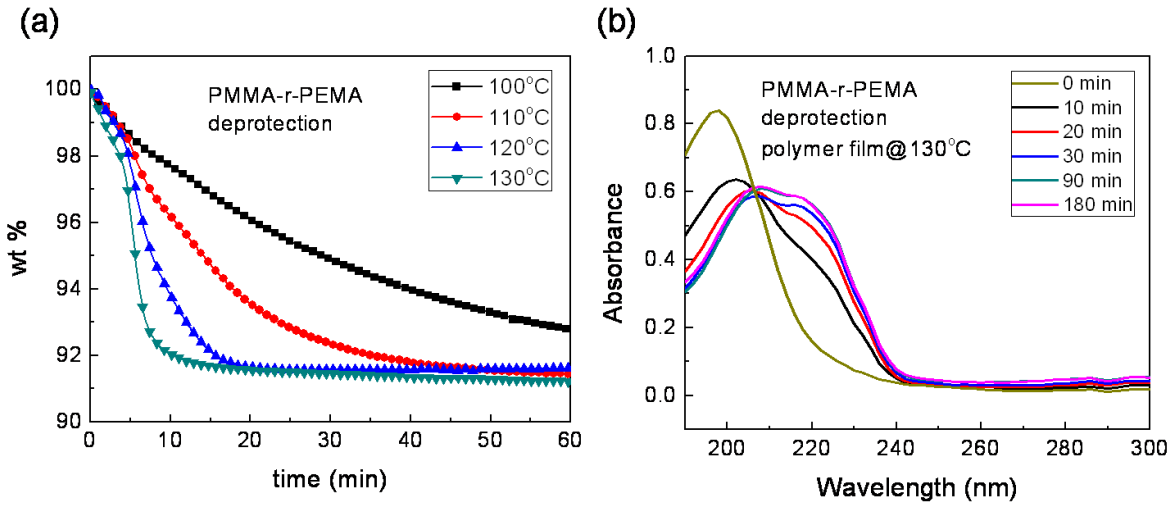

Figure 4.13 (a) TGA of PMMA-r-PEMA at 100°C, 110°C, 120°C, and 130°C. The trace at 100°C dropped further beyond 60 min to a final weight of 91.4% at 2 hr. (b) UV-Vis spectra of PMMA-r-PEMA film over time of deprotection.

4.5 Photopatterning Study

The incorporation of reactive monomers into PMMA may affect its photosensitivity. Plus, the different copolymers synthesized had different molecular weights (Table 4.1),

which may also affect their solubility and photopatterning properties. Therefore, contrast curves were measured for each of the PMMA copolymers.

Experimental. The polymer films for exposure study were spin-coated on silicon wafers. Typically, a 10 wt% polymer solution was prepared by dissolving 0.5 g polymer in 4.5 g solvent. PMMA-r-NHSMA was dissolved in cyclopentanone, PMMA-r-MAA was dissolved in 1-methoxy-2-propanol (PGME), and the other copolymers were dissolved in propylene glycol monomethyl ether acetate (PGMEA). The polymer solution was sonicated in a Cole-Parmer 8891 ultrasonic bath for 30 min and filtered through a 0.2 μm pore-size Chromafil Xtra syringe filter. The solution was loaded on the wafer and spin-coated for 1 min at 750-1500 rpm, and the coated film was baked for 2 min at 130 °C. The film thickness was measured using a J. A. Woollam M-2000V ellipsometer. Each spin-coating typically gives a thickness of 400–900 nm, and the spin-coating/baking process was repeated to build up a thickness of 2.5 ± 0.1 μm. After reaching the final thickness, the wafer was baked at 130 °C for 30 min.

The polymer film was exposed at different doses through an aluminum foil mask, under an Oriel 68810 500W mercury arc lamp with Oriel 71445 shutter control. The exposed wafer was then immersed into a developer bath for 2 min with gentle agitation, rinsed with IPA, and dried under air flow. The film thickness after exposure was measured using the Woollam ellipsometer or a Veeco Dektak 6M stylus profiler.

First, the developer formulation was determined based on the dissolution rate of unexposed film. The dissolution rate of PMMA in the MIBK: IPA developer can be adjusted by the MIBK content. A 1: 1 MIBK: IPA developer is commonly used for high throughput/sensitivity requirements and a 1: 3 MIBK: IPA developer is suitable for high resolution applications. Figure 4.14 shows the dissolution rate for the PMMA copolymers in different MIBK: IPA formulations. The MAA and PFPMA copolymer have higher

dissolution rate than PMMA, while the PMA, GMA and MEMA copolymer have lower dissolution rate than PMMA.

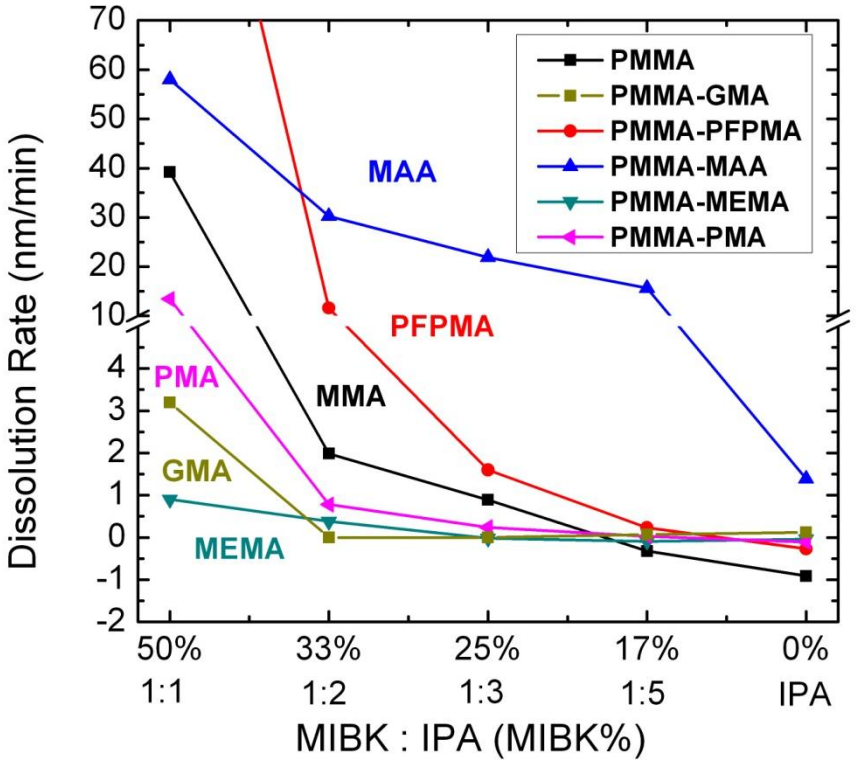

Figure 4.14 Dissolution of PMMA copolymers in 1:1, 1:2, 1:3, 1:5 MIBK: IPA and neat IPA. Negative dissolution rate indicates swelling of the polymer and thus increase in film thickness.

For the purpose of fabricating cubes with different DNA conjugated to different facets (Figure 4.6), it is important that the DNA conjugated on the top surface survives the develop process, i.e., the dissolution rate of unexposed region needs to be very low. A dissolution rate lower than 2 nm/ min was chosen in this study. Table 4.2 showed the developer choice for the contrast curve study and subsequent particle patterning. PMMA-r-NHSMA was developed in ethyl acetate: IPA (1:3) because of better solubility of the polymer in ethyl acetate.

Polymer	Developer	R_0 (nm/min)
PMMA	MIBK : IPA (1 : 3)	0.9
PMMA-r-GMA	MIBK : IPA (1 : 2)	0.0
PMMA-r-NHSMA	EtOAc : IPA (1 : 3)	-1.9
PMMA-r-PFPMA	MIBK : IPA (1 : 3)	1.6
PMMA-r-MAA	IPA	1.4
PMMA-r-MEMA	MIBK : IPA (1 : 1)	0.9
PMMA-r-PMA	MIBK : IPA (1 : 2)	0.8

Table 4.2 Developer for PMMA and PMMA copolymers. R_0: dissolution rate of unexposed film.

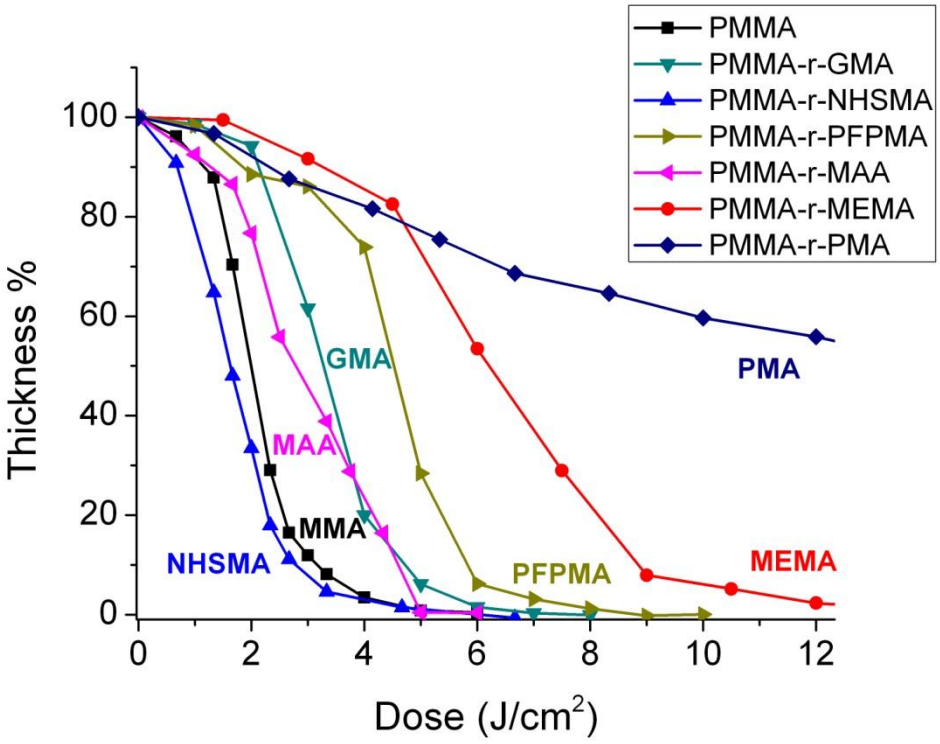

Figure 4.15 Contrast Curves for PMMA and PMMA copolymers. The film thickness was 2.5 ± 0.1 μm.

Figure 4.15 shows the contrast curves for PMMA copolymers using the developer choice in Table 4.2. Table 4.3 summarizes the energy to start develop (Q_0), energy to clear (Q_f), and contrast (γ) for the PMMA copolymers. The dosage to clear Q_f of each polymer was compared with that of PMMA. The NHSMA polymer was slightly more sensitive than PMMA, while the GMA and MAA polymer were less sensitive than PMMA. The PFPMA polymer was harder to pattern than PMMA probably due to the increased absorbance of PFPMA group. The MEMA and PMA were hard to pattern possibly due to crosslinking of the alkene and alkyne functionalities under UV light.

Polymer	Q_0 (J/cm^2)	Q_f (J/cm^2)	Q_f/Q_0 (PMMA)	γ
PMMA	0.75	3.75	1	1.4
PMMA-r-GMA	1.82	5.23	1.39	2.2
PMMA-r-NHSMA	0.35	3.30	0.88	1.0
PMMA-r-PFPMA	1.33	6.42	1.71	1.5
PMMA-r-MAA	0.68	4.82	1.29	1.2
PMMA-r-MEMA	2.37	10.7	2.85	1.5
PMMA-r-PMA	1.59	>20	>5	<1

Table 4.3 Exposure properties of PMMA and PMMA copolymers. Q_0 and Q_f are estimated dosage at 95% and 5% thickness, respectively. $\gamma = 1/ (\log_{10}(Q_f/Q_0))$.

Chapter 5: DNA Conjugation and Hybridization

The chemical linking of biomolecules, known as bioconjugation, has found wide application in biochips[78, 79] and targeted therapeutics[80]. In this chapter, the conjugation of DNAs to poly(methyl methacrylate) (PMMA) copolymers was studied in detail. The binding of complementary DNA strands, known as DNA hybridization, was also verified on the PMMA copolymer platform.

5.1 Introduction to Fluorescence

Fluorescent dyes were extensively used to label DNAs and particles in this study. Fluorescence labeling offers high sensitivity, good contrast, and multi-color capability. Fluorescence is the reemission of a photon from a photo-excited molecule or atom. Figure 5.1 shows an illustration of fluorescence (Jablonski diagram). When a molecule absorbs a photon, it is excited to a higher-energy electronic state. The excited molecule can return to the ground state by emission of a photon, and thereby a fluorescence signal is detected.

Note that each electronic state is associated with a series of finer vibrational and rotational energy levels. When a molecule is excited to a higher energy level other than the lowest excited state, it quickly relaxes to the lowest excited state before fluorescent emission takes place, a process called internal conversion and vibrational relaxation. Because fluorescence emission starts from the lowest excited state, the wavelength of emitted light is usually longer than the wavelength of absorbed light. The shift of emission spectrum with respect to excitation spectrum is known as Stokes shift. The wavelength shift is critical for easy isolation of fluorescence signals in the background of incident light.

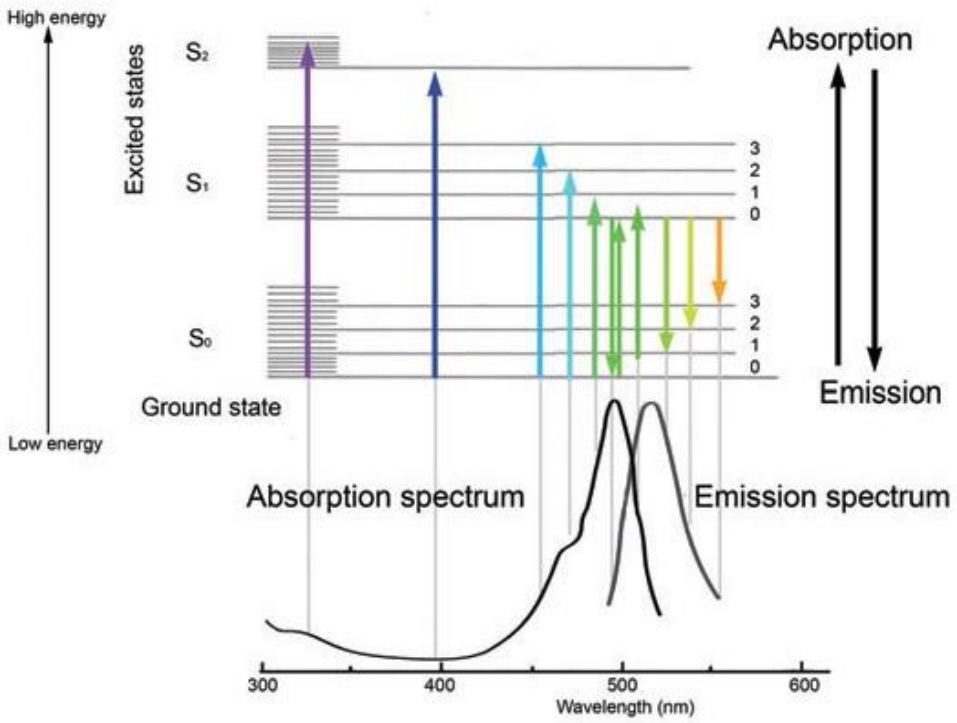

Figure 5.1 Jablonski diagram showing the energy levels of a molecule and the process of absorption and emission. The absorption (excitation) and emission spectra of a common fluorescent dye, fluorescein, is shown below. *Reprinted with permission from* [81].

Over 3,000 fluorescent dyes have been developed for various applications in molecular and cellular biology, covering the entire visible and near infrared spectrum.[82] Important parameters for selection of fluorescent dyes include excitation and emission spectra, extinction coefficient, quantum yield of fluorescence, and availability. Table 5.1 shows the structure, wavelength of maximum excitation (λ_{ex}), and wavelength of maximum emission (λ_{em}) of the fluorophores used in this study. FAM, HEX, Cy3, TYE665, and Cy5 are common fluorescent dyes for labeling DNA, where TYE665 is a substitute for Cy5 providing almost identical spectroscopic properties as Cy5. The rest of the dyes were used to label the identity of microparticles or used in the screening of bioconjugation chemistry.

Name	Structure	λ_{ex} (nm)	λ_{em} (nm)	Ref
Coumarin 314	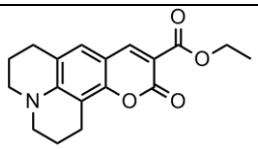	436	475	[83]
Coumarin 6	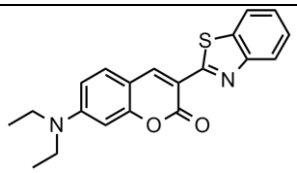	460	500	[83]
Fluorescein (FAM)	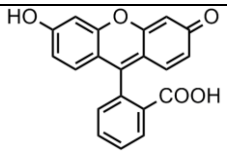	500	540	[83]
Nile Red	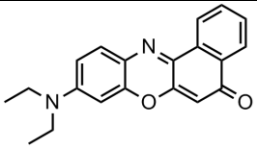	519	580	[83]
Hexachloro-fluorescein (HEX)	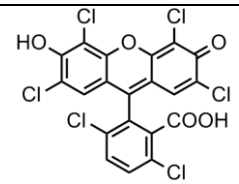	538	555	[84]
Cy3	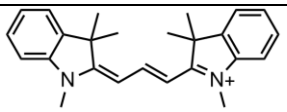	550	564	[85]
Tetramethyl-rodamine (TAMRA)	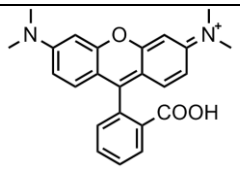	559	583	[85]
Sulforhodamine 101(Texas Red)	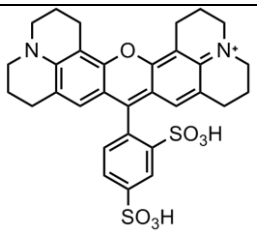	574	591	[83]

Nile Blue	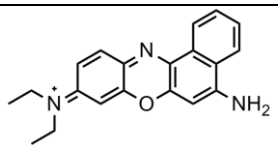	627	659	[83]
TYE 665	NA	645	665	[85]
Cy5	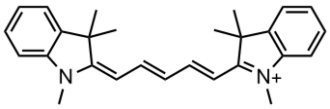	648	668	[85]

Table 5.1 Properties of fluorophores in this study. Only the parent fluorophore is shown in the structure; linkage modification is not shown.

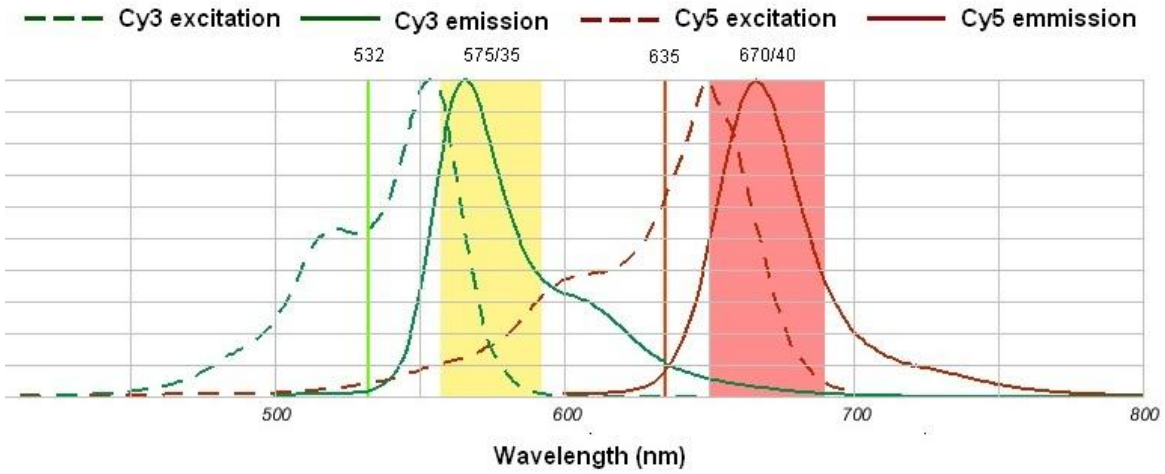

Figure 5.2 Illustration of dual-color fluorescence detection. The 532 nm and 635 nm laser excites Cy3 and Cy5 respectively. Two band-pass filters (575/35 nm and 670/40 nm) collect the emissions. Data from Molecular Probes Fluorescence SpectraViewer.[85]

The use of different excitation sources and emission filters enables fluorescence detection over multiple wavelength channels. Figure 5.2 shows an example of dual-color detection with the fluorescent dyes Cy3 and Cy5. Different excitation wavelengths are typically provided by different lasers or a broad-band illumination with monochromators/filters. Band-pass emission filters are commonly used to remove incident light and to select

emission wavelength. Table 5.2 lists the channel settings and suitable dyes for the instruments used in this study.

Instrument	Channel	Excitation (nm)	Emission (nm)	Dyes
Olympus IX71 Fluorescence Microscope	WB	460-490	520+	FAM, Coumarin 6
	WG	510-550	590+	HEX, Nile Red, Cy3, TAMRA
	Cy5	590-650	665-740	Cy5, TYE665, Nile Blue
Genepix 4000B Microarray Scanner	Green	532	557-592	Cy3, HEX, TAMRA
	Red	635	650-690	Cy5, TYE665
Amnis ISX Imaging Flow Cytometer	1	405	430-506	Coumarin 314
	2	488	504-560	FAM
	3	488	560-596	HEX, Cy3
	4	488	596-660	Texas Red
	5	658	660-720	Cy5, TYE665

Table 5.2 Channel settings of equipments and suitable fluorescent dyes.

5.2 A Fluorescence-Based Reaction Test Platform

The low concentration at which DNA is commonly handled (1~10 μM) presents significant challenges for its chemical manipulation and detection. In this regard, fluorescence labeling provides a very sensitive method to follow and quantify DNA. Figure 5.3 shows a fluorescence-based platform used to characterize the reaction between the PMMA copolymers and DNA. Briefly, the reactive PMMA copolymer described in section 4.3 was spin-coated on a glass slide and baked, and then solutions of fluorescent

dye-labeled DNA were spotted on the film. After the reaction, the glass slide was rinsed to remove excess DNA, and a fluorescence scanner recorded the fluorescence image of the entire glass slide.

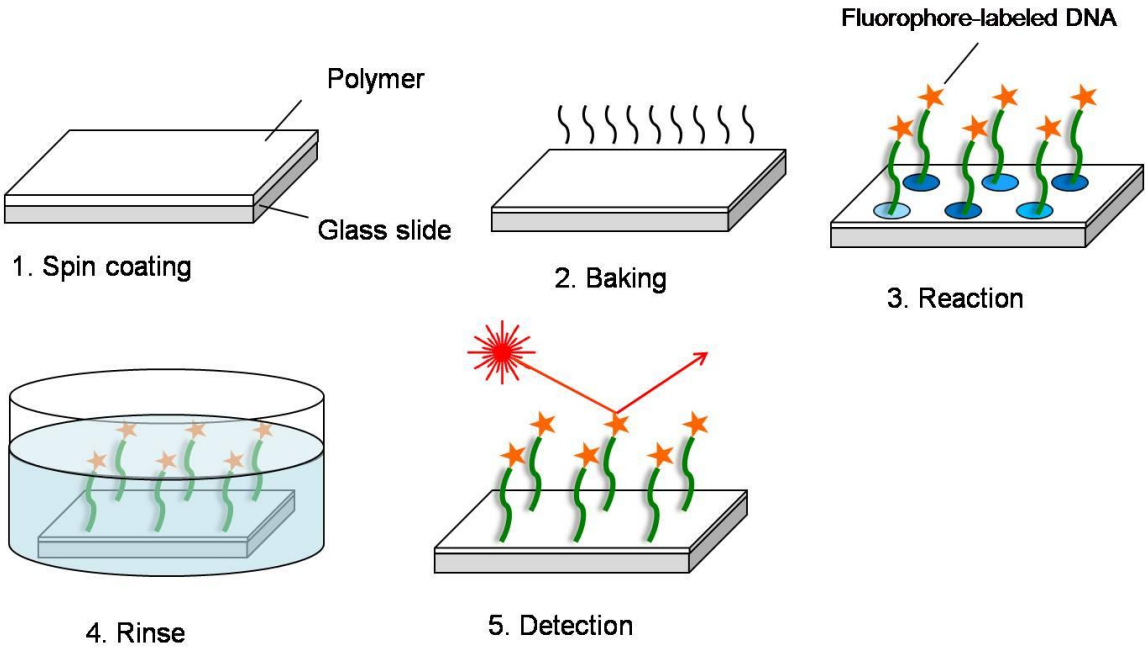

Figure 5.3 Testing of DNA-conjugation reactions using fluorescent dye-labeled DNA.

5.2.1 Experimental

General. DNA oligonucleotides with modifiers and/or fluorescent dye labels were purchased from Integrated DNA Technologies (IDT, Coralville, IA). DNA-containing solutions were prepared in Eppendorf DNA LoBind tubes. The as-received DNA sample was dissolved in sterile water to a stock concentration of 100 μM, and the stock solution was stored at 4°C until use. Fluorescence micrographs were taken by an Olympus IX-71 inverted microscope equipped with an Olympus MagnaFire SP digital camera. Fluorescence scanning images were recorded by a Genepix 4000B microarray scanner (Molecular Devices, Sunnyvale, CA). The scanner images were stored in 8-bit TIFF

format, with pixel intensities ranging from 0 (black) to 255 (white). Fluorescence intensity was quantified using GIMP 2.6 software. Background fluorescence intensity was subtracted for DNA density calculation and fluorescence intensity calibration.

Film preparation. Standard 3"×1" microscope slides were cleaned in base bath overnight, rinsed with DI water and dried. An adhesion promoter (AP410 or 2 wt% 3-(trimethoxysilyl)propyl methacrylate in PGMEA) was spin-coated onto the glass slide and baked at 160 ℃ for 5 min to improve the polymer/glass adhesion. The reactive PMMA copolymer was spin-coated onto the glass slide as described in section 4.5. A film thickness of 200 nm was adequate for the DNA conjugation study. The polymer film was then baked at 120-160 °C for 30 min to remove residual solvent and reduce passive diffusion during DNA conjugation.

DNA conjugation. DNA was conjugated onto the polymer by spotting a DNA conjugation solution onto the polymer-coated glass slide. DNA concentration was 10 μM for all reactions, and a typical spot volume was 10 μL. The spotted microslide was incubated in a humidified chamber at room temperature. After the reaction, the microslide was washed in 1× SSPE + 0.1% Tween-20 twice, and then 0.1× SSPE for three times. Buffer formulations and abbreviations were described in Appendix D. DNA sequence information was shown in Table 5.3.

The exact conjugation condition depends on the nature of conjugation chemistry. Typical conjugation conditions are described as follows:
Direct amine conjugation: 100 mM phosphate/carbonate buffer, pH 7-11, 2 mM EDTA, 16 hr.
EDC coupling: 100 mM MES buffer, pH 4-5, 16 hr.
Thiol-maleimide conjugation: 5× SSC, 2 mM EDTA, 100 μM TCEP, 1 hr.
Click chemistry: 0.5 mM $Cu(MeCN)_4PF_6$, 0.5 mM THPTA, 0.5 mM sodium ascorbate, 16 hr.

Name	Sequence (5’ to 3’)
Cy3-P4-NH_2	/5AmMC6/ATGCA GTGCG TCTTT /3Cy3Sp/
Cy3-A1-NH_2	/5AmMC6/ ATACG CACAT GCCTG TTT /3Cy3Sp/ -3’
HEX-A3-NH_2	/5HEX/$(AAAAA)_{10}$ /3AmMO/
HEX-A50-SH	/5HEX/$(AAAAA)_{10}$ /3ThioMC3-D/
A50-SH	$(AAAAA)_{10}$ /3ThioMC3-D/
T50-SH	$(TTTTT)_{10}$ /3ThioMC3-D/
HEX-A30	/5HEX/$(AAAAA)_6$
Cy3-B6-N_3	/5AzideN/ CGCAC ACGCA CGCAC GCATA CATAC GCATA /3Cy3Sp/

Table 5.3 DNA sequence information in conjugation study.

DNA reduction and purification. The reduction and purification of disulfide-modified DNA was illustrated in Figure 5.4. Typically, to a 1.5 ml eppendorf DNA LoBind tube was added 45 μL sterile water, 25 μL of 20× SSC, 10 μL of 20 mM EDTA solution, followed by 10 μL of 100 μM DNA stock solution, and then 10 μL of 1mM TCEP solution. The tube was gently vortexed and then incubated for 5 min. The as-reduced solution can be used directly for thiol-maleimide conjugation. Alternatively, it can be purified by size exclusion chromatography. Illustra Nap-5 columns preloaded with Sephadex G-25 resin were purchased from GE Healthcare. The column was washed with 10 ml of water, and then 500 μL of reduced DNA solution was loaded to the column. The column was eluted with 1 mL of water. The DNA recovery was > 90% as quantified by a NanoDrop ND-1000 Spectrophotometer.

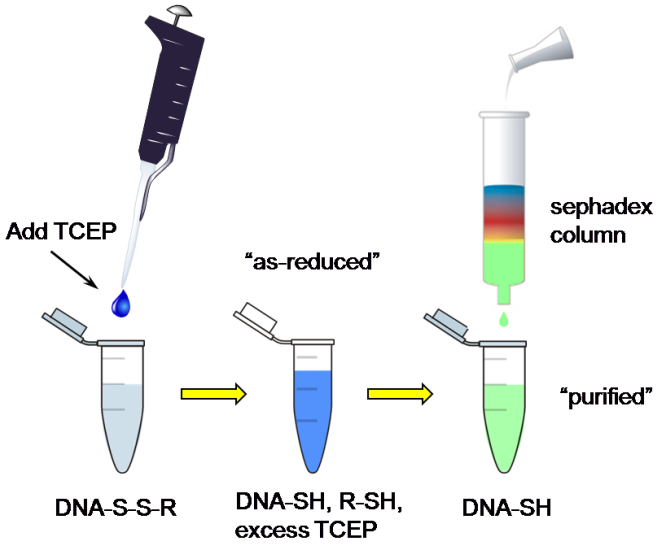

Figure 5.4 Illustration of reduction and purification procedure.

5.2.2 Results

The fluorescence-based reaction test platform was first evaluated with a fluorescent dye with aliphatic amine group (TAMRA-NH_2, or TMR-NH_2). The same dye without the aliphatic amine group (TMR-COOH) was used as a negative control. Dots of 10 μL dye solution in pH 10 buffer were spotted on PMMA-r-PFPMA film. After reaction for 24h, the slide was rinsed as described. As shown in Figure 5.5, TMR-NH_2 generated bright spots on the polymer, while TMR-COOH dots were completely rinsed off. The average intensity of TMR-NH_2 dots was 229.1, the intensity of TMR-COOH was 20.8, and the background intensity was 20.0. The high signal to noise ratio (11.0) and the low signal of the negative control clearly attested the performance of the reaction test platform.

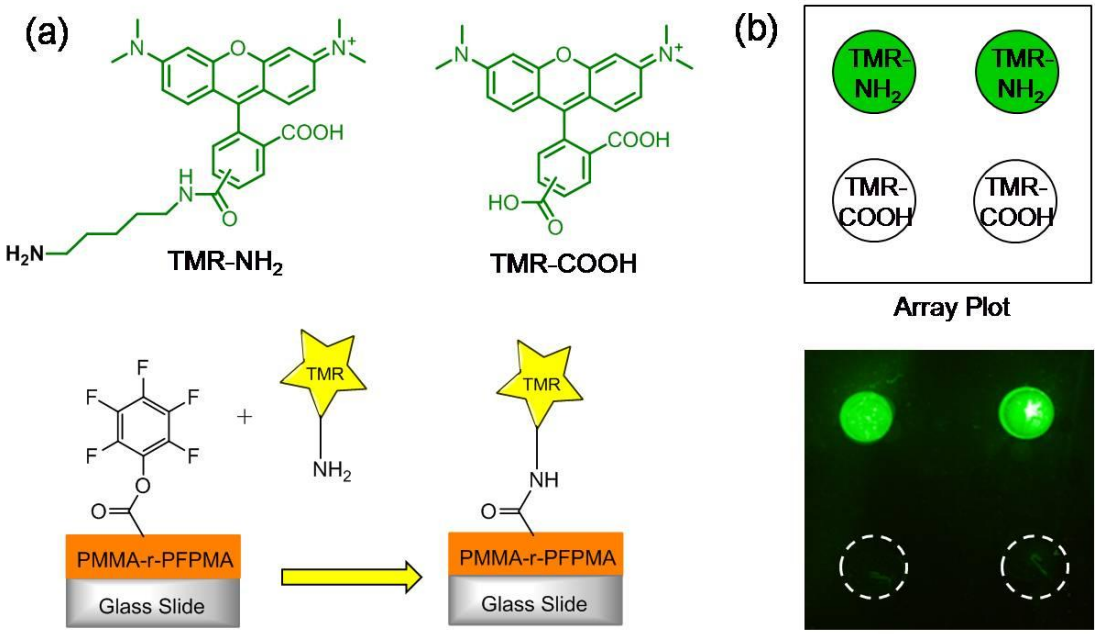

Figure 5.5 Conjugation of amine-modified fluorescent dyes to PMMA-r-PFPMA film. (a) Reaction schemes. (b) Fluorescence scanner image. Top 2 dots: TMR-NH_2. Bottom 2 dots: TMR-COOH.

5.2.3 Fluorescence Calibration

In principle, the fluorescence intensity is proportional to the density of fluorescent dyes on the polymer. Therefore, DNA density can be calculated once a calibration curve is known. To construct the calibration curve, different concentrations of dye-labeled DNA were spotted on the PMMA copolymer. After the spots dried, their fluorescence intensity was measured directly without rinse. The area of spots was also measured to calculate the DNA surface density. Figure 5.6 shows the fluorescence intensity as a function of DNA density for two commonly used DNA labels, Cy3 and HEX. Both dyes gave a nearly linear relationship between intensity and density at all three photodetector (PMT) gains. The slight deviation of HEX dye to linearity may be caused by intensity saturation/

fluorescence quenching at high concentrations. Fluorescence quenching of fluorescein-labeled DNA at density higher than 5 pmol/cm^2 has been observed.[86]

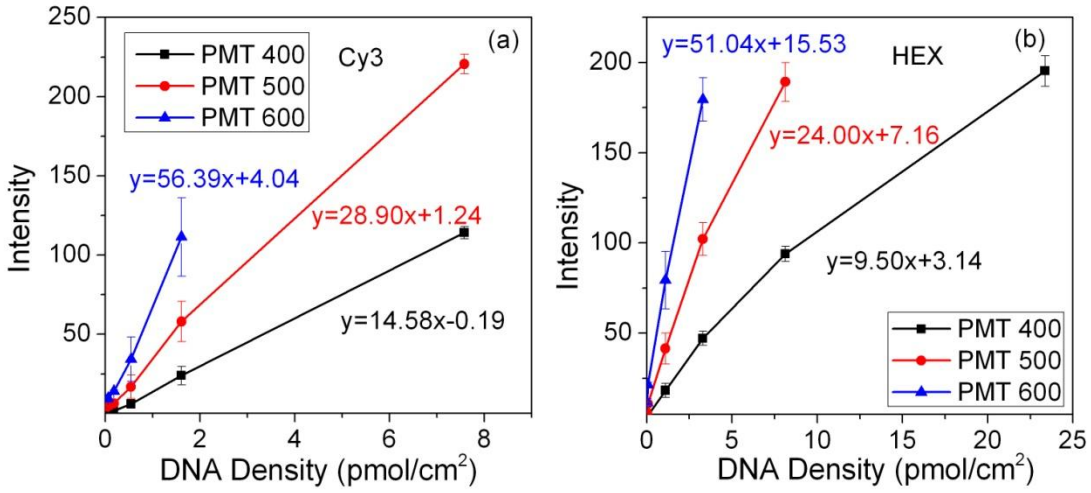

Figure 5.6 Fluorescence intensity-DNA density calibration. (a) Cy3-labeled DNA. (b) HEX-labeled DNA. PMT: The voltage of photomultiplier tube detector in the scanner.

5.3 DNA Conjugation Chemistry

The DNA conjugation efficiency of the PMMA copolymers was investigated in detail using the reaction test platform described above. The polymer-coated slide allows quick screening of reaction conditions, such as pH, concentration, and stoichiometry.

5.3.1 Amine-Active Ester Chemistry and Amine-Epoxide Chemistry

Amine modifiers for DNA at both 5' end and 3' end have been developed (Figure 5.7a). NHS esters and PFP esters can undergo nucleophilic acyl substitution with aliphatic amine under mild conditions, forming an amide bond (Figure 5.7b). Epoxide can also react directly with amine, generating β-amino alcohol.

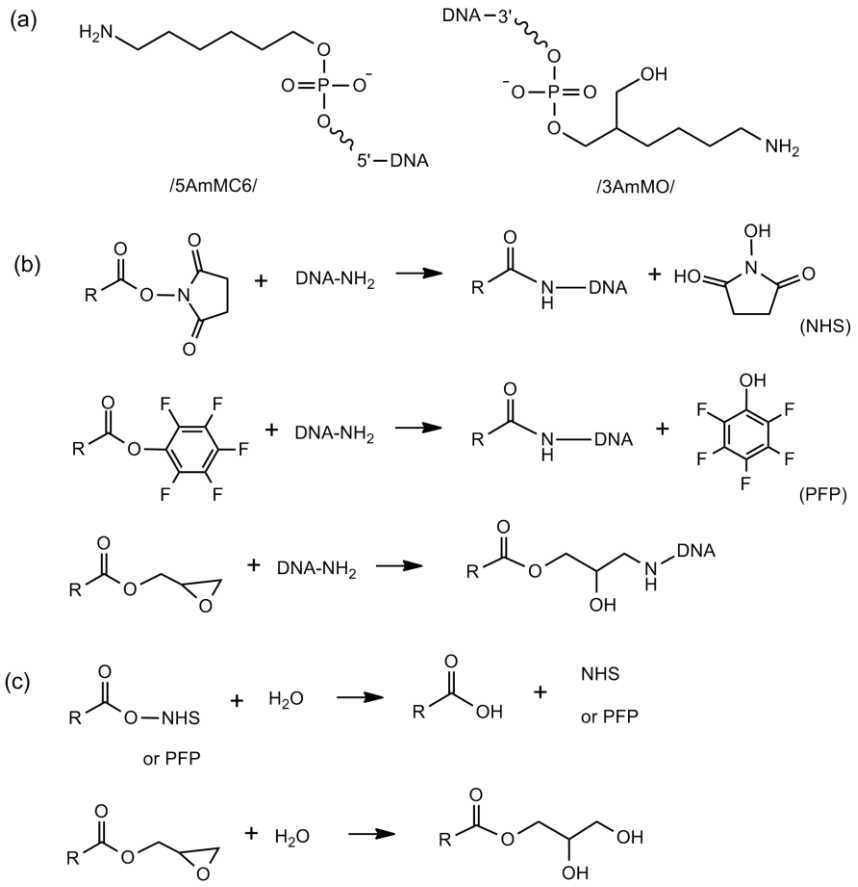

Figure 5.7 (a) Structure of 5' DNA amine-modifier /5AmMC6/ and 3' DNA amine-modifier /3AmMO/. (b) DNA-conjugation scheme using amine-active ester chemistry and epoxide chemistry. (c) Hydrolysis of active esters and epoxide.

The major side reaction for the direct amine conjugation is hydrolysis (Figure 5.7c). Since DNA is commonly handled at low concentration in aqueous media, hydrolysis may present serious limitations as the desired rate of amine substitution falls behind the rate of competitive hydrolysis. An important factor of direct amine conjugation chemistry is pH, which affects both the rate of amine conjugation and the rate of hydrolysis. Figure 5.8 shows the DNA conjugation results of GMA, NHSMA, and PFPMA copolymers. GMA and PFPMA reacted better at pH 10 and 11, while NHSMA reacted better at pH 7 and 8, indicating NHSMA was more sensitive to hydrolysis. The PFPMA copolymer provided

the best reactivity among the three polymers. The optimal DNA density of the PFPMA copolymer (5.9 pmol/cm^2) was comparable with a literature value using similar TFPMA chemistry (6.8 pmol/cm^2). [87]

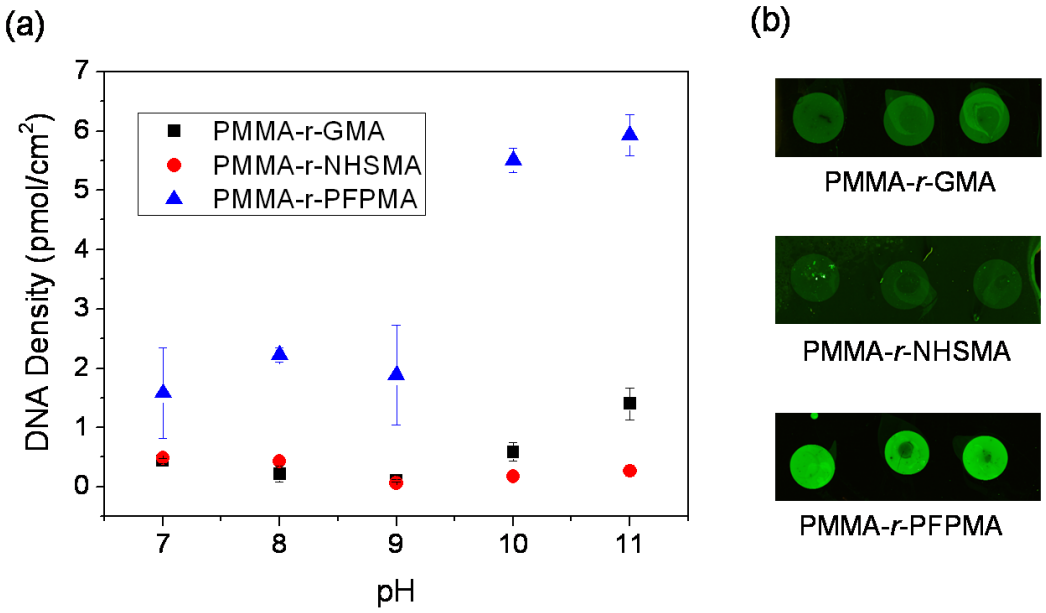

Figure 5.8 Conjugation of DNA Cy3-P4-NH_2 to PMMA copolymers. (a) DNA surface density after conjugation reaction at pH 7-11. (b) Fluorescence scanner images of the highest density dots for each polymer. Each conjugation condition was tested in triplets. PMT gain: GMA and NHSMA, 600. PFPMA, 500.

Figure 5.9 shows the DNA density of PMMA-r-PFPMA over a wider range of conjugation pH, together with a calculation result based on a rate model (see Appendix E). The conjugation yield had a plateau at pH 10 to 11.5 and dropped at both ends. The plateau behavior can be explained by as follows: at low pH such as 7 and 8, the aliphatic amine is largely protonated and has decreased reactivity, while at high pH such as 12 and 13, the high concentration of hydroxide anion speeds up the hydrolysis.

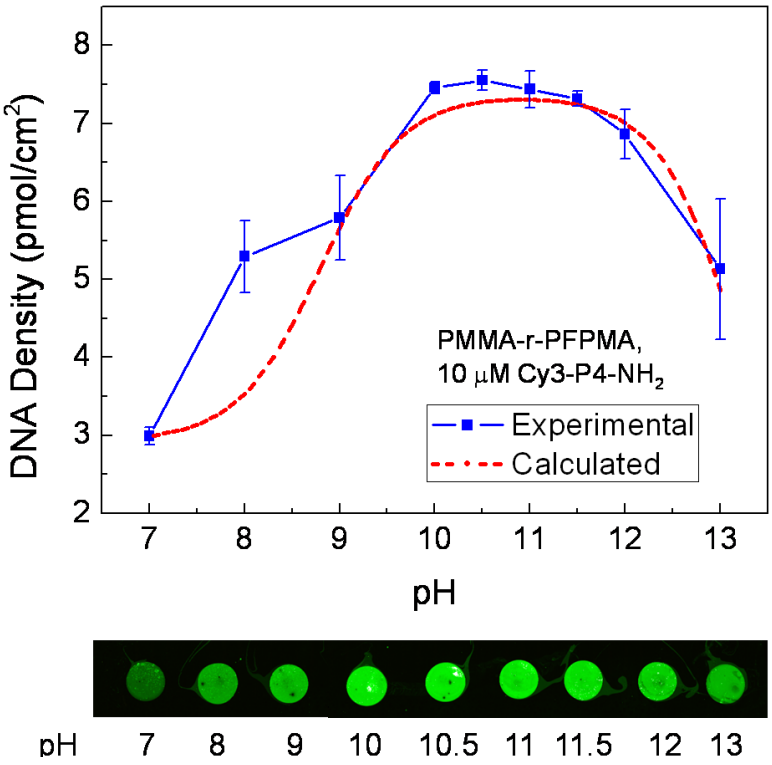

Figure 5.9 pH dependence of amine-PFPMA reaction. (Top) The conjugation reaction was conducted at different pH, and the resultant DNA surface density was plotted together with calculation results based on rate model. (Bottom) The Corresponding fluorescence images at PMT 500.

In addition to pH, the DNA conjugation yield was found to depend significantly on salt concentration. Figure 5.10 shows the conjugation of 10 μM DNA onto PMMA-r-PFPMA at different buffer and salt concentrations. Conjugation in 100 mM pH 10 buffer gave a DNA density of 6.7 pmol/cm^2, more than twice as much as the DNA density at 10 mM buffer concentration (3.1 pmol/cm^2). Measurements of pH indicated that all of the buffers had pH around 10 (10.02-10.11). Therefore, the difference in conjugation yield is not attributable to pH variation. Interestingly, simply adding NaCl salt at constant carbonate buffer concentration enhanced the conjugation yield as well. We speculate that the enhancement effect is due to the screening of DNA strand repulsion at high ionic

strength, as DNA strands are negatively charged at normal conjugation pH. Such ionic effect should be independent of the types of conjugation chemistry. Indeed, a similar effect was also observed in thiol-maleimide chemistry (Figure 5.16) and reported in thiol-gold conjugation.[88]

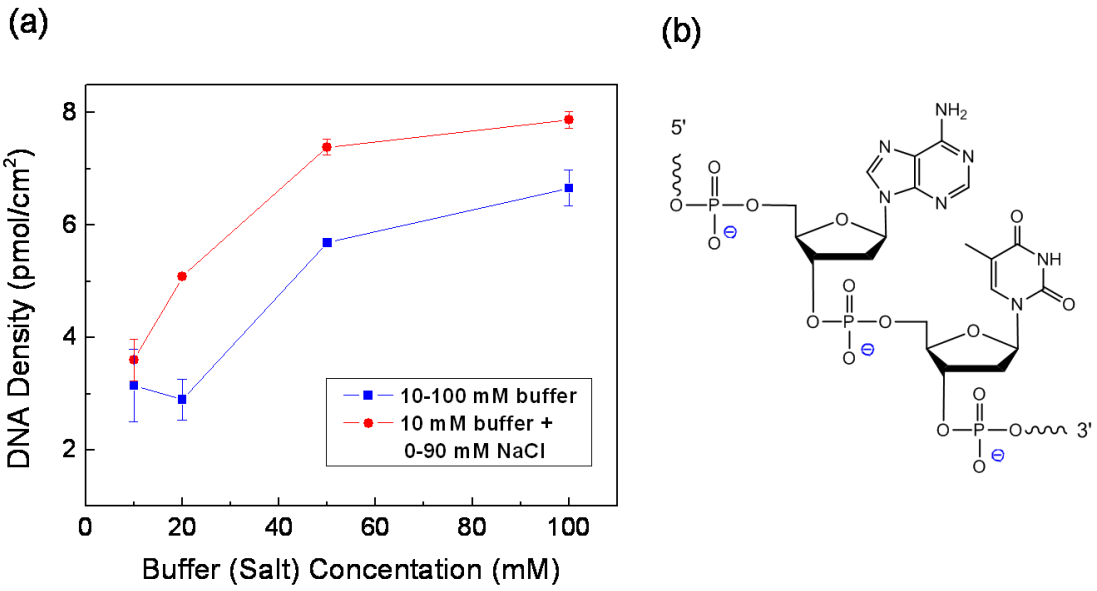

Figure 5.10 Salt concentration dependence of DNA conjugation. (a) Conjugation of 10 μM Cy3-P4-NH_2 to PMMA-r-PFPMA was conducted in 10, 20, 50, and 100 mM pH 10 carbonate buffer (blue square) or in 10 mM pH 10 buffer plus 0, 10, 40, 90 mM NaCl (red dot). The buffer of the first blue square and the first red dot were essentially the same, and the resultant DNA conjugation yields were within error, indicating good reproducibility. (b) Illustration of negative charge in DNA backbone.

5.3.2 EDC Coupling

Carbodiimides are important condensation reagents for amide formation. In carbodiimide-mediated coupling, the carbodiimide first reacts with from carboxylic acid, forming the highly reactive O-acylisourea in situ. Then the amine displaces the O-acylisourea, giving the amide product and a urea byproduct (Figure 5.11a). The reaction is often conducted in anhydrous organic solvents, however, the water-soluble reagent 1-

ethyl-3-(3-dimethylaminopropyl)carbodiimide (EDC) can be used for aqueous media reaction as well.

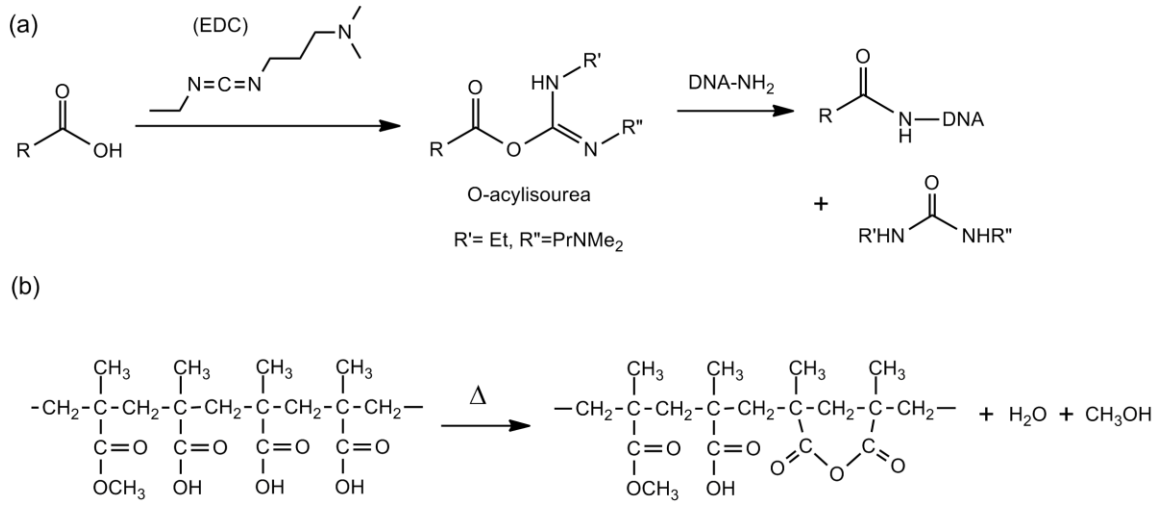

Figure 5.11 (a) DNA-conjugation scheme using EDC coupling. (b) Formation of methacrylic anhydride upon baking of PMMA-r-MAA copolymer.

DNA conjugation to the methacrylic acid copolymer PMMA-r-MAA was investigated. It is known that PMMA-r-MAA forms anhydride after baking (Figure 5.11b).[89, 90] Although anhydride reacts with amine in principle, it may be sensitive to hydrolysis and thus not provide enough reactivity for DNA conjugation at low DNA concentrations. A pre-hydrolysis step in pH 8 buffer overnight was found to increase the conjugation yield by about two-fold (Figure 5.12). The EDC concentration was also varied to find the optimal EDC loading. The highest DNA conjugation yield was achieved at 20 mM EDC concentration for both as-baked and hydrolyzed polymer film.

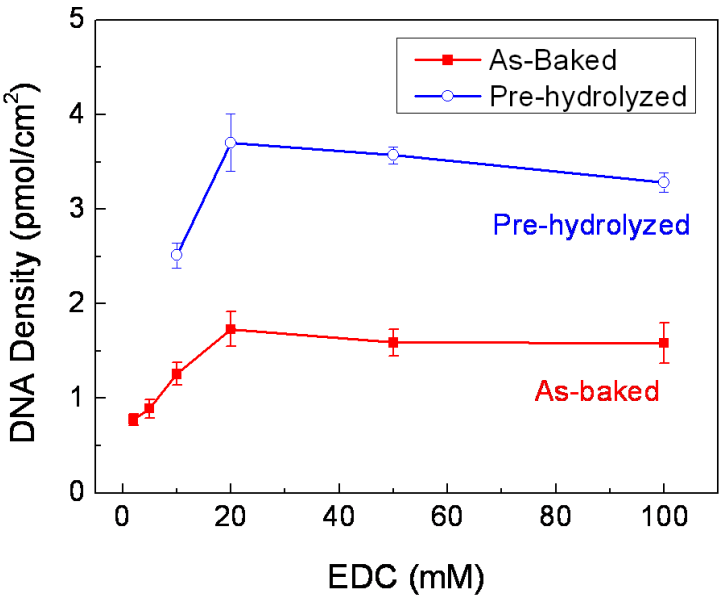

Figure 5.12 Conjugation of 10 μM HEX-A3-NH_2 to PMMA-r-MAA using EDC coupling. The reaction was conducted in 100 mM pH 4.5 MES buffer with 2 mM to 100 mM EDC concentration. Red squares: polymer as-baked at 130 °C for 30 min. Blue circles: polymer baked at 130 °C for 30 min, and then hydrolyzed in 100 mM pH 8 phosphate buffer overnight.

In contrast to the direct reaction between amine and active ester, EDC coupling gives better yield at mildly acidic conditions. The formation of the O-acylisourea intermediate was shown to be general acid catalyzed.[91] Figure 5.13 shows the pH dependence of DNA conjugation using EDC coupling. The DNA density was higher at pH 3 and pH 4.5, and started to drop at pH > 5. However, the fact that DNA may decompose at low pH also needs to be considered. It was reported that DNA depurination rate increases exponentially with decreasing pH.[92] Therefore, a pH of 4.5 to 5 was selected in EDC coupling of DNA.

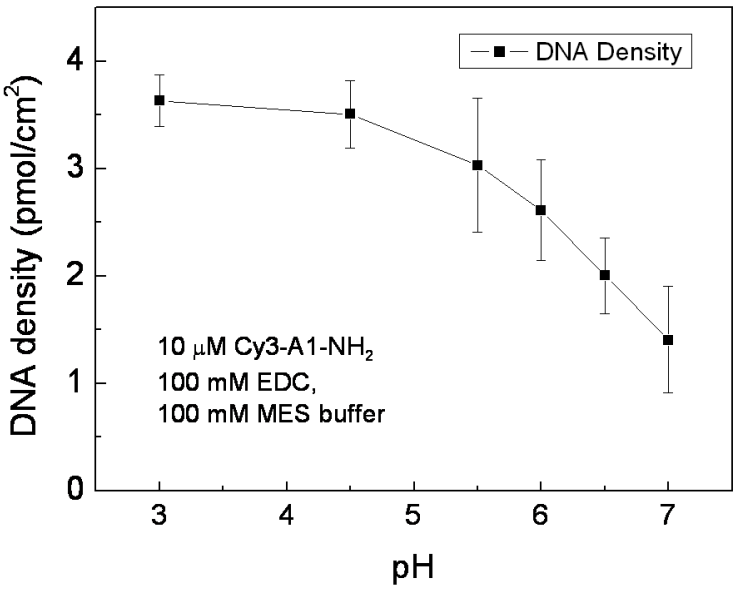

Figure 5.13 pH dependence of EDC coupling. The reaction was conducted in 100 mM MES buffer with varying pH, 100 mM EDC, and 10 μM Cy3-A1-NH_2. The PMMA-r-MAA polymer was baked at 140 °C for 30 min, and prehydrolyzed as described.

5.3.3 Thiol-Maleimide Chemistry

Thiol modification of DNA is available in disulfide form (Figure 5.14). The disulfide needs to be converted to thiol by treating with reducing agents such as dithiothreitol (DTT) or tris(2-carboxyethyl)phosphine (TCEP). After reduction, the thiol-modified DNA reacts readily with maleimide, forming a stable thioether bond. The conjugation of the DNA HEX-A50-SH to PMMA-r-MEMA was studied in this section.

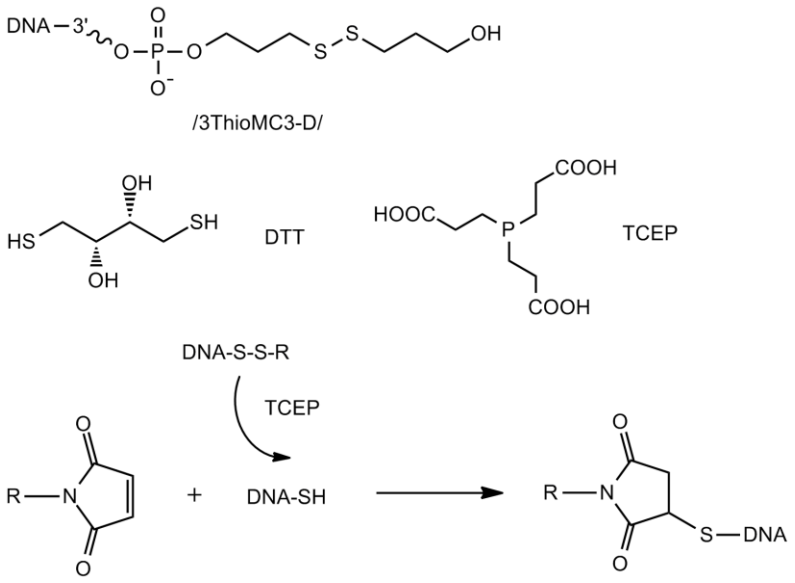

Figure 5.14 DNA-conjugation scheme using thiol-maleimide addition. The structures of thiol modifier, and two reducing agents DTT and TCEP are also shown.

The thiol-maleimide reaction proceeds optimally near neutral pH,[93] which is confirmed in Figure 5.15a. The reaction showed little variance from pH 6 to 8. However, the reaction was rather sensitive to the selection of buffer media, as thiol is susceptible to oxidation by both ambient oxygen and oxidizers such as nitrate and sulfate. SSC (saline-sodium citrate) buffer was found to the best buffer among the three buffers tested (Figure 5.15b). Sodium citrate itself is a weak reducing agent[94]; therefore, it may improve the stability of thiol in the conjugation solution. In stark contrast, the reaction failed completely in HEPES buffer (4-(2-hydroxyethyl)-1-piperazineethanesulfonic acid), possibly due to the oxidation of thiol by HEPES.

Thiol-maleimide conjugation also depends strongly on salt concentration, similar to the situation in Figure 5.10 for amine-active ester conjugation. The conjugation yield in 5 × SSC was four-fold higher than the yield in 1 × SSC (Figure 5.15b). The salt enhancement effect was further confirmed by simply adding salt into 1 × SSC (Figure 5.16).

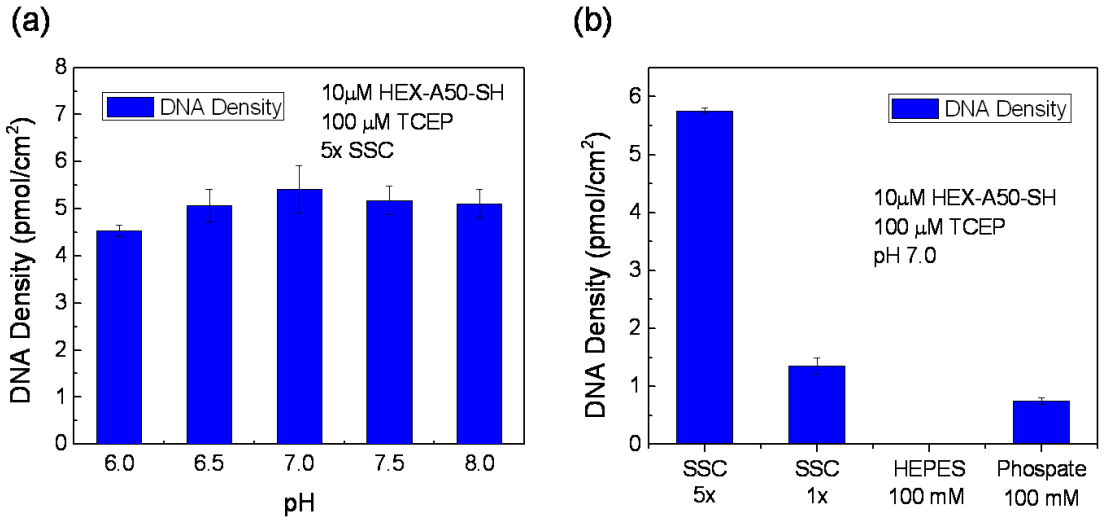

Figure 5.15 Effect of conjugation conditions for thiol-maleimide reaction. (a) pH, (b) choice of buffer.

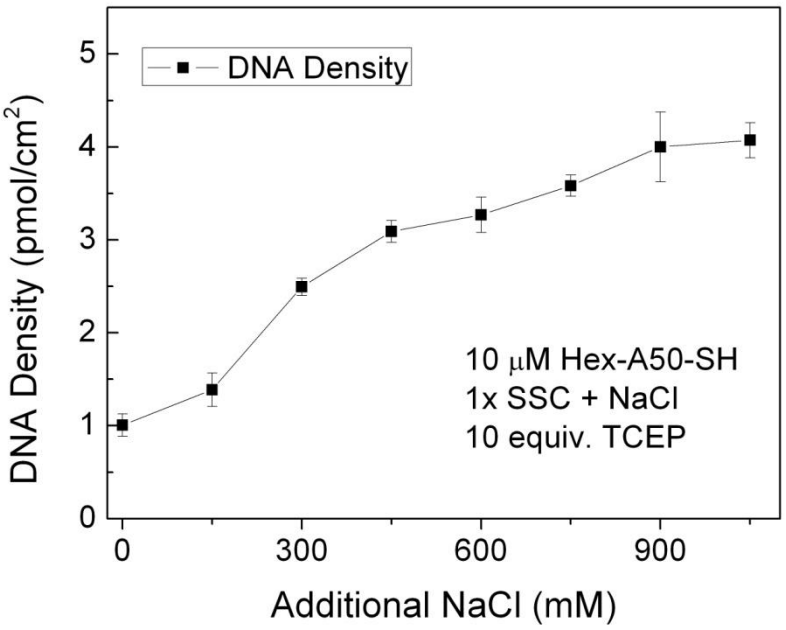

Figure 5.16 Effect of salt concentration on thiol-maleimide conjugation.

Figure 5.17 shows the effect of different reduction conditions on conjugation yield. Reduction by TCEP provided better conjugation yield than DTT (Figure 5.17a). The poor conjugation yield of DTT reduction may be caused by oxidation of DTT by ambient oxygen. The use of TCEP as reducing agent has two advantages. First, TCEP is more stable than DTT; The half-life of TCEP in most common aqueous buffers is over three weeks, while the half-life of DTT is less than 22 h.[95] Furthermore, TCEP interferes the thiol-maleimide addition only marginally, and therefore TCEP-containing DNA-SH solution can be used directly for conjugation reaction. As shown in Figure 5.16a, a 10-fold excess of did not decrease the conjugation yield, while a 100-fold excess decreased the yield by about half.

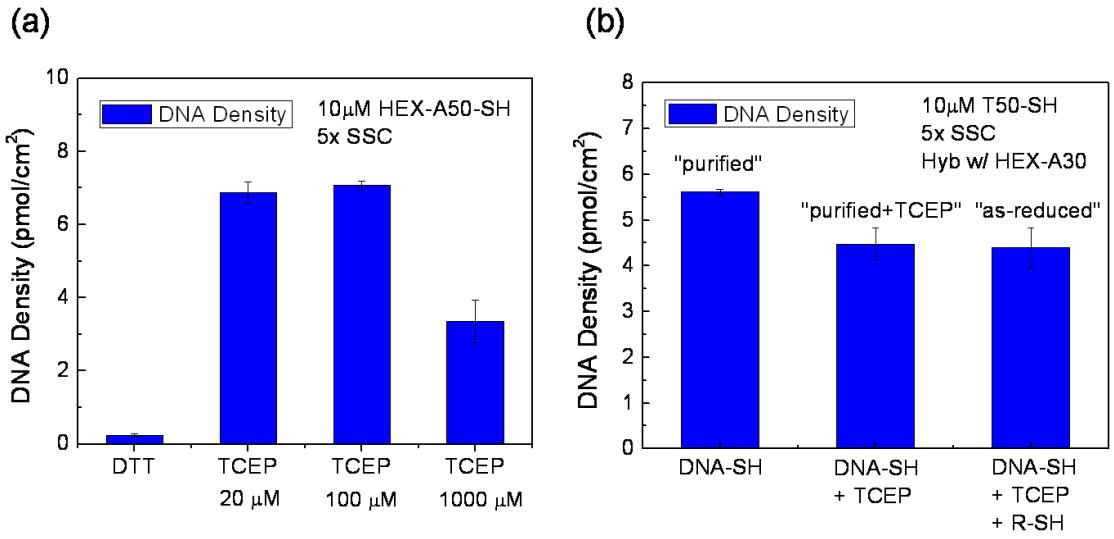

Figure 5.17 (a) Selection of reducing conditions for thiol-maleimide reaction. DTT immobilized on polyacrylamide gel (Reductacryl) was used for disulfide reduction with DTT. For TCEP reduction, the as-reduced solution was used directly. (b) Effect of purification on conjugation yield. The as-reduced mixture was purified by size-exclusion chromatography. The PMMA-r-MEMA was first conjugated with DNA T50-SH without fluorescent label, and then a fluorescent labeled complement Hex-A30 was hybridized. A hydridization ratio of 1.43 was assumed in calculation of ssDNA density (see section 5.4).

The effect of TCEP interference was further clarified by purification of the reduction mixture (Figure 5.16b). The crude reduction product contains DNA-SH, excess TCEP, and a thiol byproduct (3-mercapto-1-propanol, MPA). The smaller TCEP and MPA molecules can be removed from DNA using size-exclusion chromatography. Purified DNA-SH gave 28% higher DNA density than the crude reduction product. Although the purification improved the conjugation yield moderately, the as-reduced mixture was used directly for conjugation reaction in most experiments because chromatographic DNA purification would require large volumes of DNA.

5.3.4 Click Chemistry

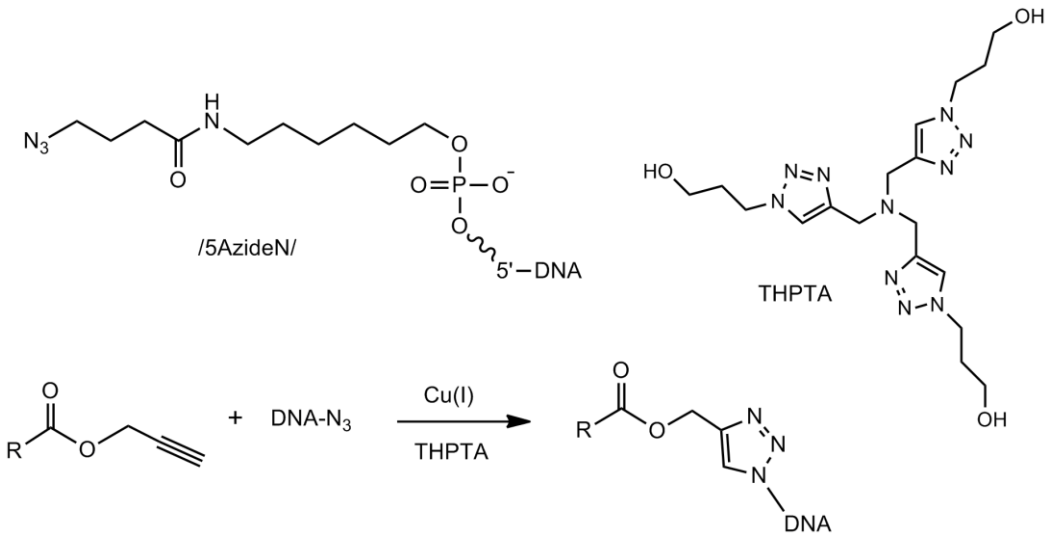

Figure 5.18 DNA-conjugation scheme using click chemistry. The structures of azide modifier and the copper ligand THPTA are shown.

One of the recent development in bioconjugation chemistry is the 1,3-dipolar cycloaddition between azides and alkynes, often referred to as “click chemistry”. [96] Click chemistry is very specific and offer high yields under mild conditions. [97] The common catalyst for this reaction, Cu(I), may cause degradation of DNA.[98] Cu(I)-

binding ligands such as tris-hydroxypropyltriazolylamine (THPTA) have been developed to prevent DNA degradation. The conjugation scheme of azide-modified DNA is shown in Figure 5.18.

Figure 5.19 shows the effect of THPTA ligand on DNA conjugation. The DNA density was 4.9 pmol/cm^2 without THPTA. Loading of one equivalent of THPTA versus the copper(I) catalyst $Cu(MeCN)_4PF_6$ increased the DNA density to 7.4 pmol/cm^2 (a 51% increase). The copper(I) catalyst can also be generated in situ using copper (II) chloride and sodium ascorbate, which gave a comparable DNA density of 7.1 pmol/cm^2. An excess of the THPTA ligand suppressed the reaction yield, and in the presence of EDTA, the reaction with completely inhibited, possibly due to the tight binding of Cu(I) with EDTA.

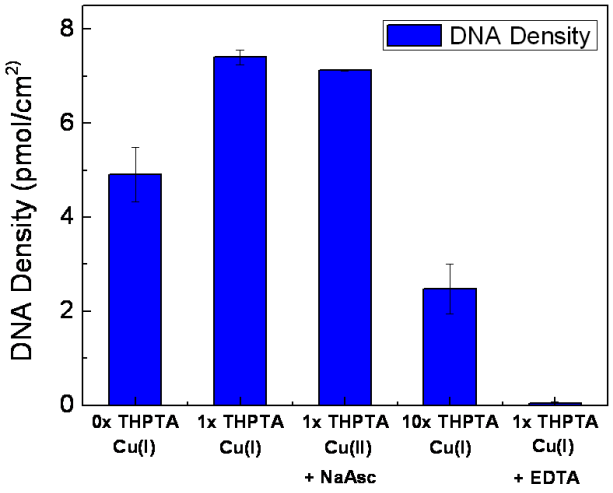

Figure 5.19 Conjugation of 10 μM Cy3-B6-N_3 to PMMA-r-PMA using click chemistry. The catalyst loading was 0.5 mM $Cu(MeCN)_4PF_6$, denoted in the graph as "Cu(I)", or 0.5 mM $CuCl_2$ "Cu(II)" + 0.5 M sodium ascorbate (NaAsc). 1 × THPTA corresponds to 0.5 mM (copper catalyst loading).

5.3.5 Summary of Conjugation Chemistry

Figure 5.20a shows the optimal DNA density for the six copolymers tested. PFPMA provided the best conjugation yield among the four conjugation methods using amine-modified DNAs. The thiol-maleimide chemistry, and azide-alkyne click chemistry, gave comparable yields with amine-PFP ester chemistry. Figure 5.20b plots the DNA density with photosensitivity (defined as the inverse of dose to clear, $1/Q_f$). It is unfortunate that the most photosensitive polymer, PMMA-r-NHSMA, provided the lowest DNA conjugation reactivity, and one of the most reactive copolymers, PMMA-r-PMA, was essentially unpatternable in our exposure setup (Figure 4.15). Considering both photopatterning and DNA conjugation properties, the PFPMA, MAA, and MEMA copolymers were investigated further for their potential in particle fabrication.

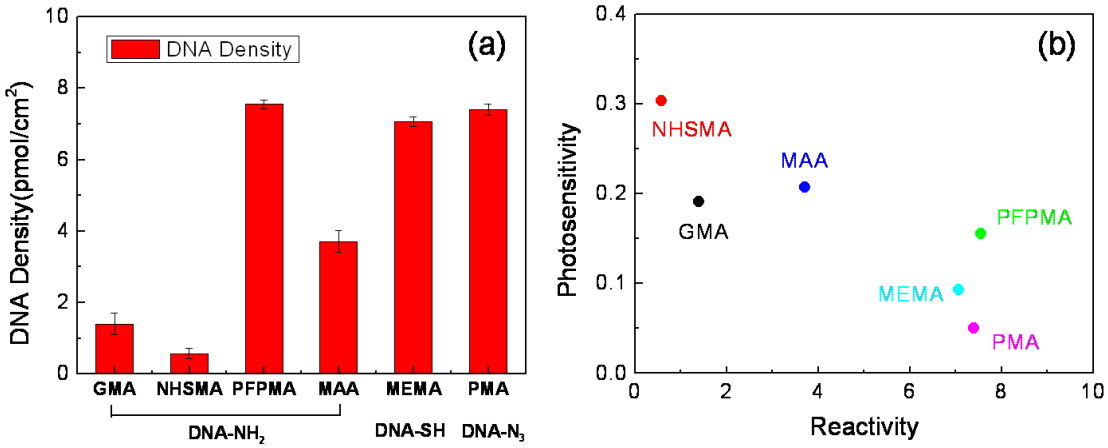

Figure 5.20 (a) Optimal DNA density of the six copolymers. (b) Plot of reactivity (DNA density) with photosensitivity ($1/Q_f$).

5.4 DNA Hybridization

5.4.1 DNA Melting Temperature

The binding of two single-strand DNAs (ssDNAs) into a double-strand DNA (dsDNA) can be treated as a chemical equilibrium:

$$A + B \underset{}{\overset{K}{\rightleftharpoons}} AB$$

where A and B are two ssDNAs, and AB is a dsDNA. The equilibrium constant K of hybridization can be expressed by:

$$\ln K = -\frac{\Delta G^\circ}{RT} = -\frac{\Delta H^\circ}{RT} + \frac{\Delta S^\circ}{R} \tag{5.1}$$

Taking the derivative over temperature gives the van't-Hoff equation:

$$\frac{d \ln K}{dT} = \frac{\Delta H^\circ}{RT^2} \tag{5.2}$$

DNA hybridization is exothermic ($\Delta H°<0$). Therefore, at high temperature K decreases and the process favors dissociation into ssDNAs. The dissociation is often described by biochemists as "DNA melting". A DNA melting curve can be measured by dsDNA-specific fluorescent dyes such as SYBR Green I.[99] The fluorescence intensity of SYBR Green I decreases as the dsDNA dissociates at high temperature. Figure 5.21 shows a sample DNA melting curve measured by the fluorescence method. The DNA dissociation proceeds gradually over a temperature range over 10°C.

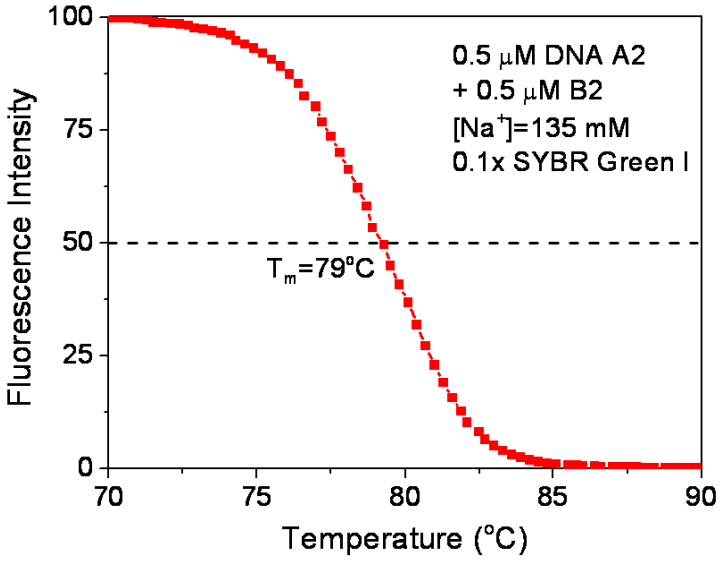

Figure 5.21 DNA melting curve of the A2-B2 dsDNA measured by fluorescence method using SYBR Green I. The fluorescence intensity has been corrected and normalized.

DNA melting point (T_m) is widely adopted as a simple metric for DNA duplex stability. DNA melting point is defined as the temperature where 50% of the dsDNA dissociates into ssDNA. For example, T_m was 79°C for DNA A2-B2 in Figure 5.21. DNA melting point is directly related to the thermodynamics of DNA duplex formation. Let *c* denotes the total DNA concentration counted as ssDNA. The concentration of fully hybridized A-B duplex will be *c/2*. At DNA melting point when half of the duplex dissociates, [A] = [B] = [AB] = *c/4*, and we have

$$K = \frac{[AB]}{[A][B]} = \frac{1}{c/4},$$

$$\Delta G^\circ = \Delta H^\circ - T\Delta S^\circ = -RT\ln K = RT\ln(\frac{c}{4})$$

Solving T gives

$$T_m = \frac{\Delta H^\circ}{\Delta S^\circ + R\ln(\frac{c}{4})} \qquad (5.3)$$

DNA melting point increases with DNA length and GC content. As discussed briefly in section 4.1, the A-T pair has two hydrogen bonds, while the G-C pair has three hydrogen bonds. Therefore, a G-C pair contributes a larger free energy gain than an A-T pair. A simple equation to estimate DNA melting point is:

$$T_m = 4\,(G + C) + 2\,(A + T)\ ^\circ C \tag{5.4}$$

Taking DNA A2-B2 in Figure 5.21 as an example, the DNA has 13 G-C pairs and 12 A-T pairs. Therefore, $T_m = 4 \times 13 + 2 \times 12 = 76\ ^\circ C$. The result is only 3°C lower than the experimentally measured 79°C.

More sophisticated methods, such as the nearest-neighbor model [100-102], consider not only the hydrogen bonding energy but also the stacking energy between bases. There are ten possible neighboring pairs: AA/TT, AT/TA, TA/AT, CA/GT, GT/CA, CT/GA, GA/CT, CG/GC, GC/CG, GG/CC. The thermodynamic parameters for all of nearest neighbor pairs have been established[100], as shown in Table 5.4. Note the more negative ΔG° of G-C pairs (-2.07 kcal/mol on average) than A-T pairs (-0.82 kcal/mol on average).

The total ΔG° of a dsDNA strand is given by:[100]

$$\Delta G^\circ = \Delta G^\circ(init) + \sum_i n_i \Delta G^\circ(i) + \Delta G^\circ(sym) \tag{5.5}$$

where $\Delta G^\circ(init)$ is the initiation term for both terminals of the dsDNA, $\Delta G^\circ(i)$ is the standard free energy change for the ten possible nearest neighbors, n_i is the number of occurences for each nearest neighbors, and $\Delta G^\circ(sym)$ is a correction term if the DNA is self-complementary. After calculation of ΔH° and ΔS° using similar formulations, the DNA melting point T_m can be determined from eqn. (5.3).

Sequence	ΔH° (kcal/mol)	ΔS° (cal/K·mol)	$\Delta G°_{37}$ (kcal/mol)
G/C initiation	0.1	-2.8	0.97
A/T initiation	2.3	4.1	1.03
AA/TT	-7.9	-22.2	-1.01
AT/TA	-7.2	-20.4	-0.87
TA/AT	-7.2	-21.3	-0.59
CA/GT	-8.5	-22.7	-1.46
GT/CA	-8.4	-22.4	-1.45
CT/GA	-7.8	-21.0	-1.29
GA/CT	-8.2	-22.2	-1.31
CG/GC	-10.6	-27.2	-2.16
GC/CG	-9.8	-24.4	-2.23
GG/CC	-8.0	-19.9	-1.83
Symmetry correction	0	-1.4	0.43

Table 5.4 Nearest-neighbor parameters of ΔH °, ΔS°, and calculated ΔG° at 37°C in 1M NaCl,. Data adapted from ref. [100].

Finally, DNA melting temperature increases with ionic strength because high salt concentration screens the electrostatic repulsion between the two ssDNA strands and stabilizes DNA duplex. The T_m and ΔG° determined from eqn. (5.5) are based on 1M NaCl concentration. The following correction equation for salt concentration has been suggested: [101]

$$T_m^{[Na^+]} = T_m^{1M} + 12.5\log[Na^+] \quad (5.6)$$

That is, a ten-fold Na^+ concentration will cause 12.5 °C difference in DNA melting point. The correction provides reasonable results for NaCl concentration between 0.1M and 1M.

Again, taking DNA A2-B2 as an example, T_m calculation by nearest neighbor method using NUPACK online server[103] gives T_m = 72.7 °C, a 6°C deviation from the

experiment value. The deviation is larger than the simple estimation method using equation (5.4)!

5.4.2 DNA Hybridization on Polymer Surface

Hybridization on polymer surface was tested to verify that the polymer-conjugated ssDNA retained the ability to hybridize with complementary DNA strands. Figure 5.22 illustrates the method of DNA hybridization analysis.

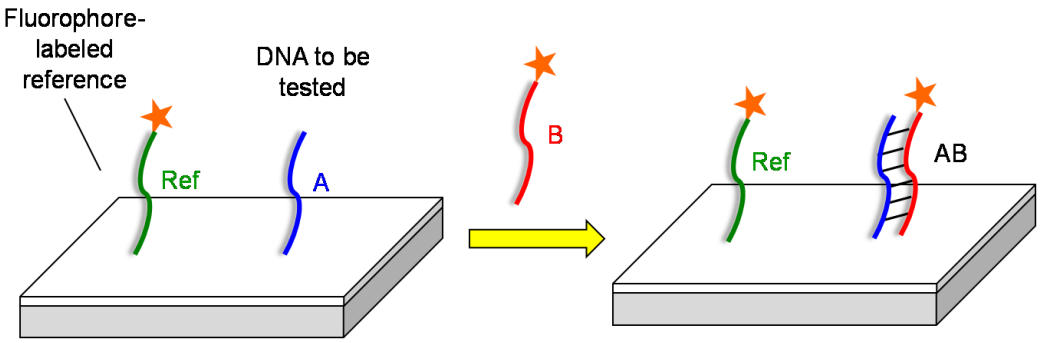

Figure 5.22 Illustration of the DNA hybridization experiment.

First, ssDNAs were conjugated to the PMMA copolymer. A fluorophore labeled DNA was also conjugated as reference for DNA surface density. The polymer slide was then immersed in a solution of complementary DNA, and the slide was scanned after rinse off of non-specifically bound DNA. The hybridization efficiency was estimated by comparing the fluorescence intensity of the hybribridized dsDNA versus the reference ssDNA.

Experimental. The DNA-immobilized polymer slide was prepared as described in section 5.2.1. The slide was first rinsed with DI water to remove incidental hybridization of reference strands. The slide was then hybridized with a solution of complementary DNA under a coverslip in a humidified chamber. A typical hybridization solution

contains 10 μM DNA, 20 mM pH 7 phosphate buffer, 1 mM EDTA, and 0.1 M NaCl. After hybridizing for 1~4 hr, the microslide was washed in 5× SSC + 0.1% SDS + 2 mM EDTA + 1 M NaCl for 5 min, and then a second wash in 0.1× SSC + 2 mM EDTA + 0.5 M NaCl for 10 min. The DNA sequences are listed in Table 5.5. Three hybridization sets were tested: a P15-T15 DNA with 15bp overlap, a 30-mer polyA with a 30-mer polyT (A30-T30), and a 50-mer polyA with a 30-mer polyT (A50-T30). The P15-T15 and A30-T30 DNAs were tested on PMMA-r-PFPMA, and the A50-T30 DNA was tested on PMMA-r-MEMA. The hybridization yield was calculated as the fluorescence intensity ratio of the DNA duplex and the reference DNA.

Name	Sequence (5' to 3')
P8-NH_2	/5AmMC6/AAAGT GCGTG TTAGT GCC
Hex-T8	/5HEX/CACGG CACTA ACACG CAC
Hex-Ref1-NH_2	/5HEX/CACGG CACTA ACACG CAC /3AmMO/
A30-NH_2	/5AmMC6/ $(AAAAA)_6$
T30-NH_2	/5AmMC6/ $(TTTTT)_6$
HEX-A30	/5HEX/$(AAAAA)_6$
A50-SH	$(AAAAA)_{10}$ /3ThioMC3-D/
T50-SH	$(TTTTT)_{10}$ /3ThioMC3-D/
HEX-Ref2-SH	/5HEX/$(AAAAA)_{10}$ /3ThioMC3-D/

Table 5.5 DNA sequence information in conjugation study.

Results. Figure 5.23 shows the fluorescence image of reference ssDNA and hybridized dsDNA. The P8/T8 hybridization gave 55% yield, while the A30/T30 hybridization gave 99.9% yield. The melting points of the two DNA strands are similar (calculated melting point: P8/T8, 61.3°C, A30/T30, 61.7°C, at 10 μM DNA concentration and 135 mM Na^+ concentration). Therefore, the better hybridization of A30/T30 may benefit from factors other than thermodynamic stability. The longer and shiftable A30/T30 strand may have

less steric hindrance during hybridization on polymer surface. The hybridization yield of A50/T30 was 143%, indicating that the longer A50 DNA can bind with two copies of the shorter T30 DNA. Non complementary DNAs (A30/A30) showed little interaction. The high hybridization yield and low non-specific binding verified that DNA conjugated to PMMA surface was fully functional in terms of binding complementary strands.

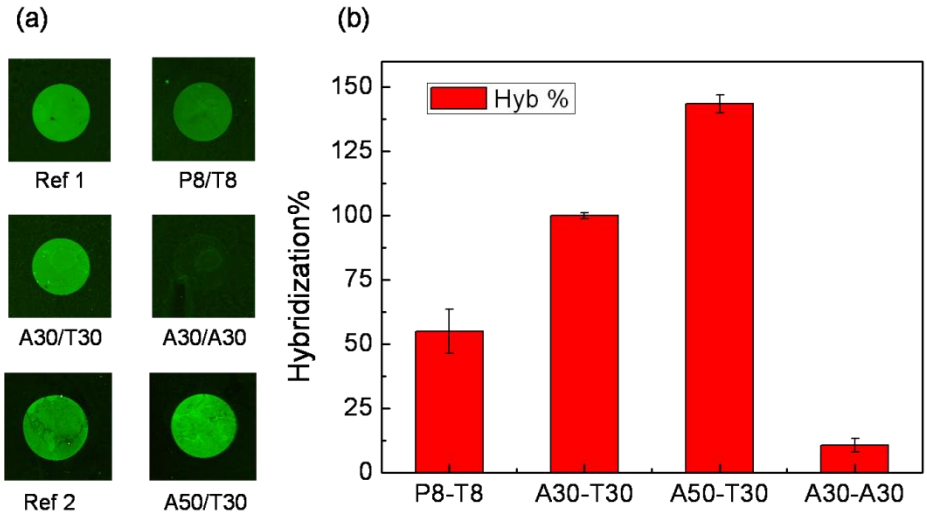

Figure 5.23 (a) Fluorecence image of reference ssDNA and hybridized dsDNA. (b) Calculated hybridization yield.

5.4.3 Binding of Microspheres to Polymer Surface

The DNA-conjugated polymer slide is also a convenient platform to test the assembly conditions of DNA-coated microspheres. The DNA density on the PMMA copolymer surface was ~7 pmol/cm^2 (Figure 5.20). Bead binding was tested to verify that such a DNA density was adequate to guide the assembly of microscale particles. Figure 5.24 illustrates the binding of microspheres to polymer surface mediated by DNA hybridization.

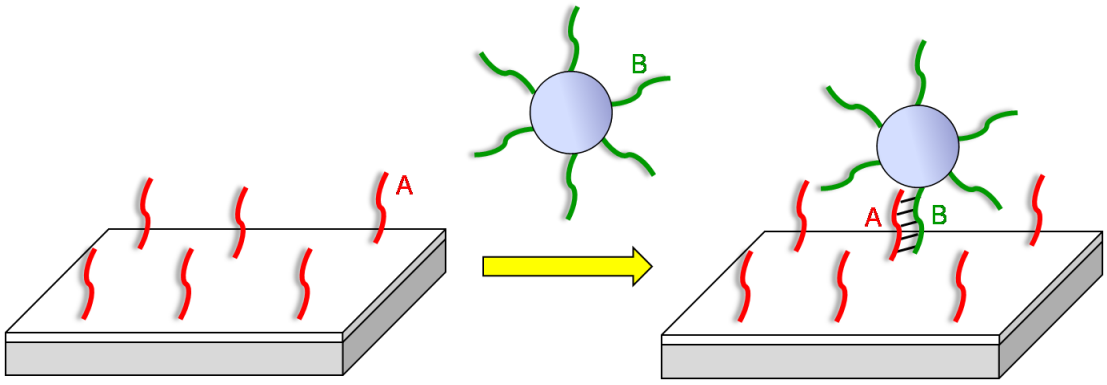

Figure 5.24 DNA-mediated assembly of microspheres to polymer surface.

Experimental. The DNA-immobilized polymer slide was prepared as described in section 5.2.1. The DNA spot location was marked by a cross sign on the back of the glass slide. Sera-Mag oligo$(dT)_{14}$ magnetic particle (1 μm diameter) was purchased from Thermo Scientific and directly used in the bead binding experiment. Streptavidin-coated polystyrene microsphere (3 μm diameter) was purchased from Bangs laboratories. Biotinylated T30 DNA (/5Biosg/$(TTTTT)_6$) was conjugated to the streptavidin-coated microspheres as follows. To an Eppendorf DNA LoBind tube was added 180 μL DI water, 20 μL of 1 wt% streptavidin-coated PS microsphere suspension, followed by 0.3 μL of 1 mM Biotin-T30. The suspension was incubated for 10 min and then centrifuged at 6000 rpm for 2 min. The supernatant was aspirated and 200 μL of 1M TEAB solution was added. The tube was vortexed, centrifuged again, and finally suspended in 20 μL of 1 M TEAB buffer. For microsphere binding to polymer surface, each DNA spot on the polymer was immersed in 20 μL of 0.1 wt% bead suspension in a binding buffer. The slide was incubated at room temperature for 1 hr and then excess beads was washed off carefully in a rinse buffer. For 1 μm magnetic bead binding, the binding buffer was 1 M TEAB + 2 mM EDTA, and the rinse buffer was 0.8 M TEAB + 2 mM EDTA + 0.1% SDS. For 3 μm PS bead binding, both the binding buffer and the rinse buffer were 0.2 M TEAB + 2 mM EDTA + 0.1% tween-20.

Results. Figure 5.25 shows the array plot and the image of microsphere-assembled polymer slides. DNA A50 and T50 were conjugated to the polymer, and then suspensions of polyT-conjugated microspheres were applied on the polymer. A rinse step differentiated the binding of A50 region and T50 region. As expected, the polyT-coated microspheres specifically binded to the A50 region. The experiment confirmed that the DNA density on the polymer surface was adequate to recruit beads with complementary DNAs. The diffuse reflection of microspheres on the polymer surface can be easily observed, and therefore, the microsphere assembly approach hold promise to provide an instrument-free detection for DNA hybridization.

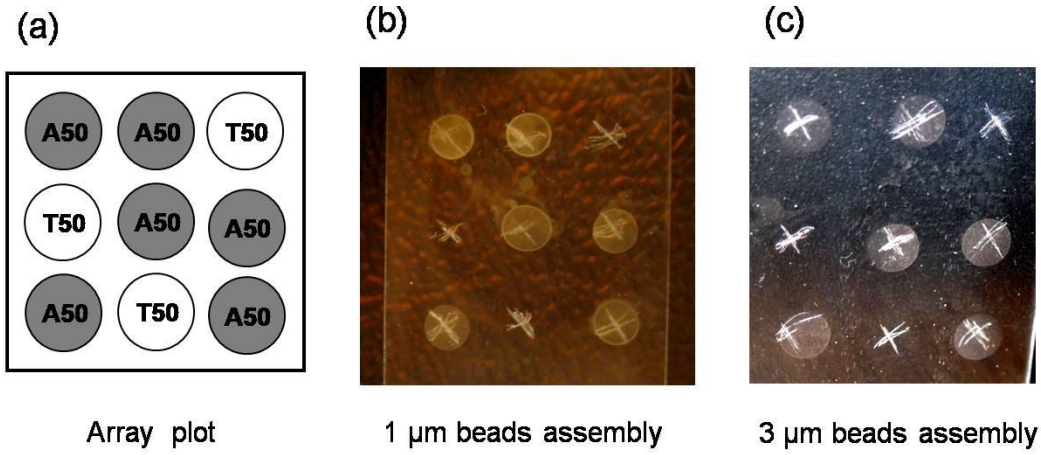

Figure 5.25 DNA-mediated assembly of microspheres to polymer film. (a) Array plot. (b) Assembly of 1 μm particles coated with 14 mer of dT. (c) Assembly of 3 μm particles coated with 30 mer of dT.

Chapter 6: DNA-Guided Self-Assembly of Microspheres

6.1 Introduction

DNA-directed self-assembly has attracted both scientific and technological interest. The use of DNA as a "smart glue" in self-assembly imparts many advantages, including high specificity, thermal reversibility, and modulation of assembly by factors such as nucleases[69] and competitive displacement[70]. Most intriguingly, studies of DNA-mediated colloidal crystallization[65, 66, 104] have shown that there may be an intimate relationship between the building block properties and the lattice parameters of the resultant self-assembled solids.

Unfortunately, it is often difficult to characterize fully the morphologies and distribution of morphologies that are created by DNA-directed assembly of particles, much less to couple the characteristics of individual particles to the yield and characteristics of larger aggregates. Many methods have been used to characterize and follow the progress of self-assembly, including UV-vis spectroscopy[65, 105], optical and fluorescence microscopy[67, 69, 70], electron microscopy[65, 66, 105, 106], light scattering[105, 106], and X-ray diffraction[66, 104]. However, these tools are largely used to characterize bulk properties rather than study individual particles in what are generally complex mixtures and distributions of assembly products and aggregates.

In this regard, flow cytometry[107] is particularly well-suited to the analysis of the self-assembled clusters of micrometer-sized particles. Flow cytometry is a cell biology

technique that rapidly measures the optical properties of individual cells. It gives statistically robust, quantitative counting results by measuring the scattering and/or fluorescence intensity form thousands of suspended particles as they pass one-by-one through an optical detector region. Soto et al.[108] previously used flow cytometry to estimate the assembly yield of submicron polystyrene (PS) particles. Recently, imaging flow cytometry[109-111], a technique combining conventional flow cytometry with high-speed microscopy, has become available. Traditional cytometry gives intensity values for each particle as a function of wavelength, but imaging flow cytometry provides these data together with a fluorescence micrograph of each particle. Therefore, imaging flow cytometry analysis of DNA-guided microsphere assembly generates a detailed report describing both the number and morphology of different types of assemblies. These data enable an analysis of the details of the assembly distribution as a function of changes in the substrate, DNA sequence, reaction conditions, etc., which can provide guidance for the production of useful, large-scale assemblies.

6.2 Experimental

Polybead® Carboxylate Microspheres were purchased from Polysciences (Warrington, PA). Fluorescein cadaverine and Texas Red cadaverine were purchased from Biotium (Hayward, CA). Imaging flow cytometry was performed on an Amnis ImageStreamX Imaging Flow Cytometer (Seattle, WA) with 488nm and 658nm laser excitation. The Grace Bio-Labs SecureSeal™ hybridization chamber for static microscopy of bead assemblies was purchased from Sigma-Aldrich (St. Louis, MO). Optical and fluorescence micrographs were taken on a Zeiss Axiovert 200 M microscope equipped with a Zeiss Axiocam fluorescence camera (Thornwood, NY).

The DNA-conjugated particles in this study were prepared via EDC coupling of carboxylate-modified PS microspheres and amine-modified DNAs. Two labeling

schemes were used to identify the microsphere. The first scheme uses DNA with both a fluorophore label and an amine modifier (Figure 6.1a). The second scheme conjugates non-fluorescent DNA first, and then conjugates fluorescent dyes to the remaining carboxylate groups on the microsphere (Figure 6.1b).

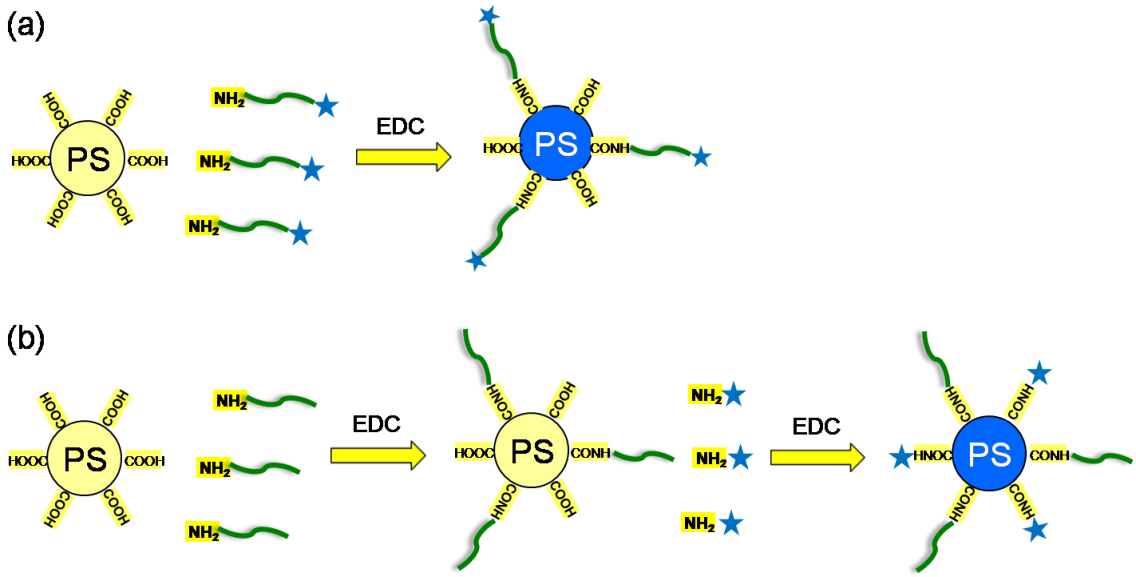

Figure 6.1 DNA conjugation and labeling schemes. (a) Scheme I: one step, double-labeled DNA. (b) Scheme II: two step, single-labeled DNA.

DNA conjugation. The as-received carboxylate bead suspension was washed by centrifugation and resuspension in sterile water three times. For conjugation scheme I, 20 µL of the washed bead suspension was added into an Eppendorf tube, followed by addition of 23 µL sterile water, 27 µL of 375 mM MES buffer (pH 4.5), 5 µL of 100 µM DNA solution, and 25 µL of 0.2 M EDC. The conjugation suspension was incubated in the dark on a shaker table at room temperature overnight. For conjugation scheme II, after DNA conjugation overnight, 35 µL of 200 µM fluorescent dye solution (Texa Red cadaverine or fluorescein cadaverine) was added to the DNA conjugation solution, followed by 25 µL of 0.2 M EDC. The bead suspension was then incubated for additional 10 h. Finally, the suspension was centrifuged and resuspended four times in 200 µL of

0.4 M TEAB + 0.1% Tween 20 + 2 mM EDTA. The DNA-conjugated beads were stored at 4°C in the dark, and their hybridization ability was stable for at least three months.

Figure 6.2 illustrates the self-assembly of PS microspheres with complementary strands, in which the polyvalent presentation of DNA on the PS microspheres generates a distribution of assemblies, including dimers, trimers, and higher-order aggregates. Four fully-complementary dsDNAs were tested (A1-B1, A2-B2, A3-B3, and A4-B4), and their sequences are listed in Table 6.1.

Name	Sequence
A1	/5AmMC6/ ATACG CACAT GCCTG TTT /3Cy3Sp/
B1	/5AmMC6/ AAACA GGCAT GTGCG TAT /3Cy5Sp/
A2	/5AmMC6/ TATGC GTATG TATGC GTGCG TGCGT
B2	/5AmMC6/ ACGCA CGCAC GCATA CATAC GCATA
A3	/56FAM/ $(AAAAA\ AAAAA)_5$ /3AmMO/
B3	/5TYE665/ $(TTTTT\ TTTTT)_5$ /3AmMO/
A4	/5FAM/CCTCC CCTTT TATGC GTATG TATGC GTGCG TGCGT /3AmMO/
B4	/5TYE665/ACGCA CGCAC GCATA CATAC GCATA AAAGG GGAGG /3AmMO/
C	/56FAM/ TACAT GCAGT GCGTC TTT /3AmMO/

Table 6.1 DNA sequences (5'→3') for microsphere assembly. The functional groups and fluorescent labels are written in the sequence format of Integrated DNA Technologies. DNA A2 and B2 were conjugated using scheme II, using fluorescein cadaverine to label A2 beads and Texas Red cadaverine to label B2 beads. Strand C is a mismatch sequence as a negative control.

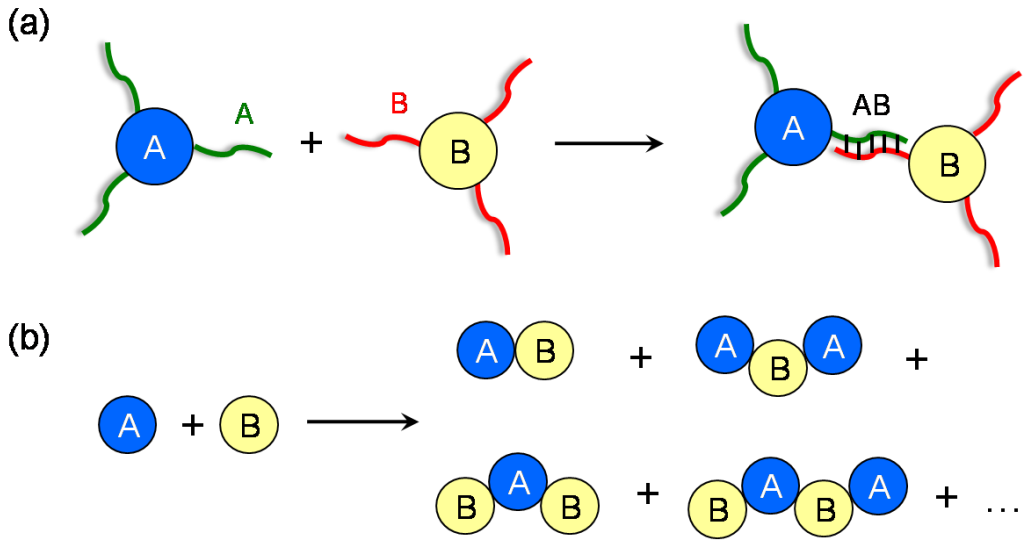

Figure 6.2 Assembly scheme of polyvalent PS microspheres using DNA. (a) Complementary DNA strands (A and B) were conjugated onto PS microspheres. (b) The polyvalent nature of these PS microspheres yields a mixture of aggregates, including dimer (AB), trimer (A_2B and AB_2), tetramer (A_2B_2), etc. DNA strands were omitted in this graph for clarity.

Flow cytometry. PS beads with the desired DNA sequences were mixed and incubated in 0.4M TEAB + 0.1% Tween 20 for three minutes on a shaker table. The bead sample was then injected into the flow cytometer. After the flow stabilized, at least 2000 images were acquired for analysis. Flow cytometry data was processed using IDEAS 5.0 software supplied by Amnis.

Fluorescence compensation. Fluorescence intensities in different wavelength channels often have crosstalking with each other due to spectra overlap. The crosstalk can be reduced by fluorescence compensation. For a pair of fluorophores 1 and 2, their compensated fluorescence intensity I_1', I_2' is calculated using the following equations:

$$I_1^{'} = \frac{1}{1-\alpha_{12}\alpha_{21}} I_1 - \frac{\alpha_{12}}{1-\alpha_{12}\alpha_{21}} I_2 \tag{6.1a}$$

$$I_2^{'} = -\frac{\alpha_{21}}{1-\alpha_{12}\alpha_{21}} I_1 + \frac{1}{1-\alpha_{12}\alpha_{21}} I_2 \tag{6.1b}$$

where I_1, I_2 is the measured fluorescence intensity without compensation, α_{12} and α_{21} are constants describing the coupling of the two fluorophores.

Figure 6.3 shows an example of fluorescence compensation. In Figure 6.3(a), the flow cytometry fluorescence scattering diagram was plotted with uncompensated fluorescence intensity, while in Figure 6.3(b) it was plotted with compensated fluorescence intensity. The removal of crosstalk facilitates data processing and the assignments of assembly populations.

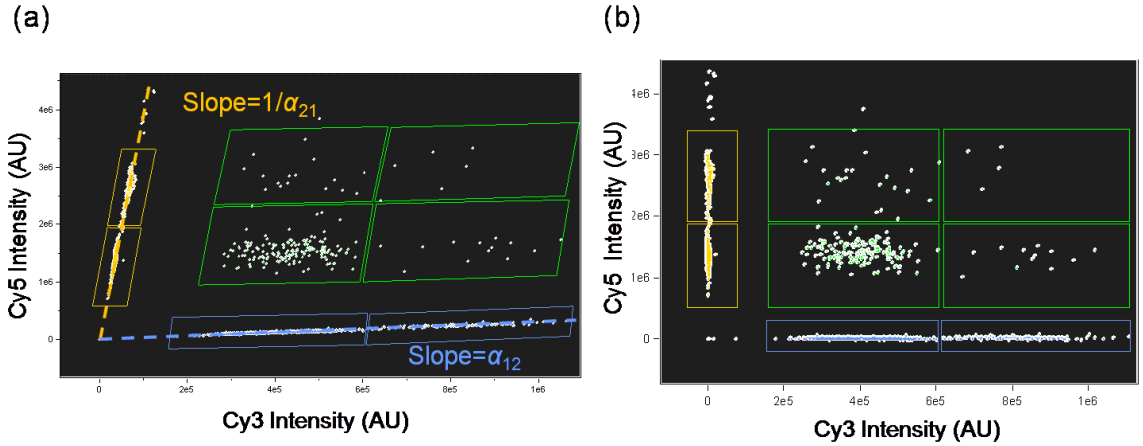

Figure 6.3 Effect of fluorescence compensation. (a) Flow cytometry diagram with uncompensated fluorescence intensity. (b) The diagram with compensated fluorescence intensity.

Definitions. Assembly yield is defined as the number of A-B assemblies divided by total number of particles and particle clusters:

$$Yield = \frac{n(A_m B_n)}{n(A_m B_n) + n(A_m) + n(B_n)}, \; m, n \geq 1 \tag{6.2}$$

Conversion of A (or B) is defined by the number of A-B assemblies divided by number of all the A- (or B-) containing particles:

$$Conversion(A) = \frac{n(A_m B_n)}{n(A_m B_n) + n(A_m)},\ m, n \geq 1 \tag{6.3a}$$

$$Conversion(B) = \frac{n(A_m B_n)}{n(A_m B_n) + n(B_n)},\ m, n \geq 1 \tag{6.3b}$$

The stoichiometry of beads is estimated from compensated fluorescence intensities by the following equation:

$$\frac{A}{B} = \frac{I_A / I_{A0}}{I_B / I_{B0}} \tag{6.4}$$

where I_A, I_B is the total fluorescence intensities of the assembly mixture at two wavelength channels , I_{A0} and I_{B0} are the average fluorescence intensity for A monomer and B monomer, respectively.

6.3 Results and Discussion

6.3.1 Double-Fluorescence Plot

Dual-color fluorescent labeling was employed, allowing different self-assembled microsphere aggregates to be readily distinguished. Figure 6.4 shows a double-fluorescence scatter plot and fluorescent micrographs for an experiment in which 6μm-diameter PS beads conjugated with the complementary DNA strands A1 and B1 were assembled.

In the double-fluorescence scatter plot, the fluorescence intensities at two different wavelengths are plotted against each other for each particle cluster. For example, unbound A1 beads (blue color) reside near the *x* axis because they have a high Cy3 fluorescence intensity but almost zero Cy 5 intensity. Likewise, the B1 beads (yellow color) reside near the *y* axis. The A1-B1 assemblies reside in the middle of the plot and

can be further resolved into distinct subpopulations, including dimers (AB), trimers (A_2B and AB_2), and tetramers (A_2B_2).

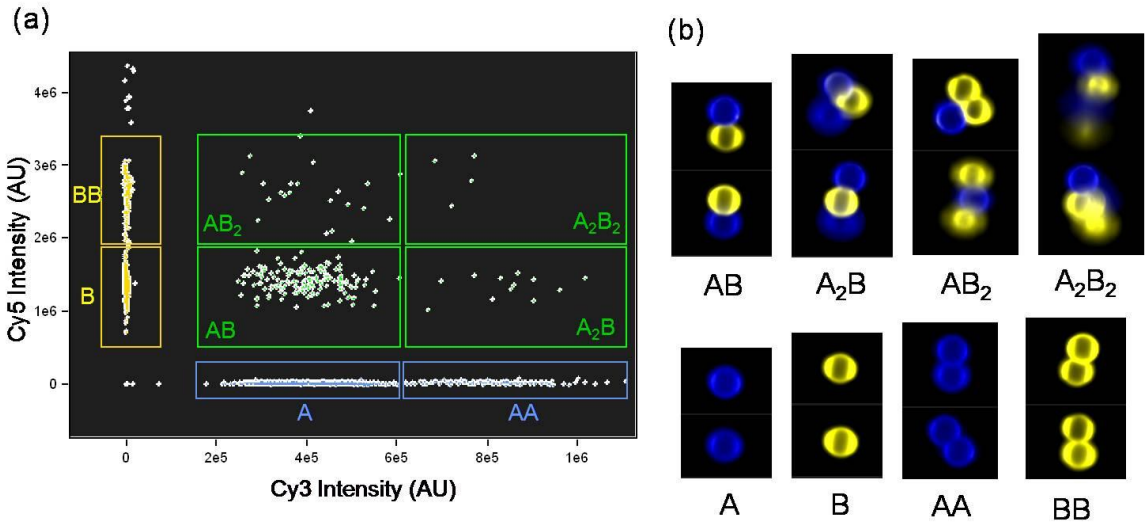

Figure 6.4 (a) Imaging flow cytometry chart of 6μm-diameter PS beads assembly. The beads were conjugated with DNA strands A1 (Cy3 fluorophore, blue color) and B1 (Cy5 fluorophore, yellow color). The fluorescence intensities have been compensated. (b) Representative fluorescent micrographs of beads in each assigned region.

The validity of the assignments within the plot was confirmed by studying the fluorescence micrographs in Figure 6.4b. The yield of each type of aggregate was established in this manner. In this experiment, the assembly produced mainly dimers, with few trimer and tetramer assemblies (171 AB, 6.7%; 12 A_2B, 0.5%; 21 AB_2, 0.8%; 4 A_2B_2, 0.2%). We also noticed a significant number of homodimers (126 AA, 4.9% and 179 BB, 7.0%), which may result from the formation of secondary structures formed by partial overlap of DNA strands (Figure 6.5). The formation of secondary structures decreases the specificity of bead assembly, and therefore, care must be taken in DNA sequence design to minimize the potential self-binding of DNA strands.

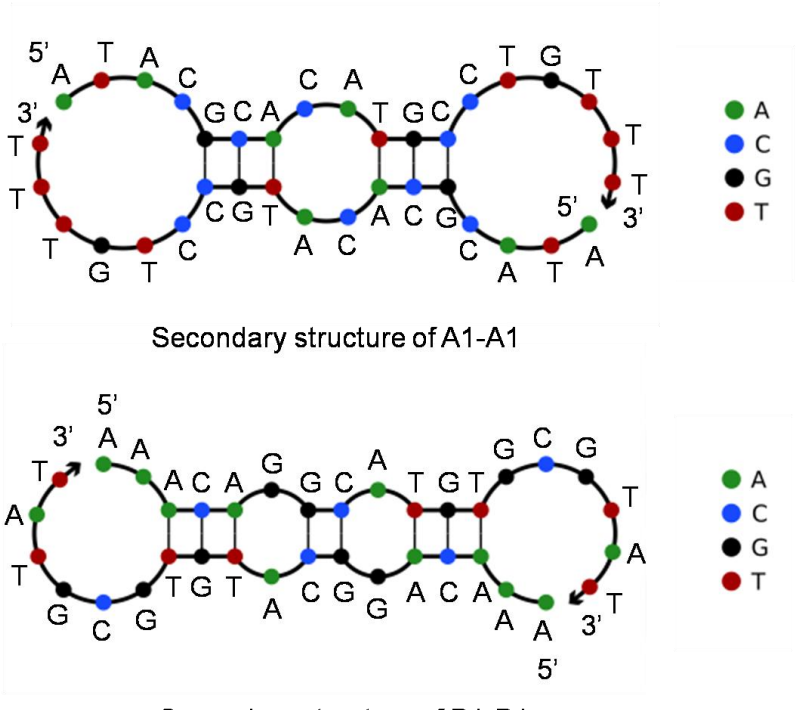

Figure 6.5 Secondary structure formed by self binding of A1-A1 and B1-B1.

It has been reported that DNA complementarity as short as 12 bp was adequate to drive the assembly of 1 μm and 2 μm beads[112]. While fully-complementary 18 bp strands A1 and B1 can drive the assembly of 6μm beads in a static fluorescence microscopy setup (Figure 6.6), the 18 bp complement provides only a low assembly yield in flow cytometry. The majority of the assembly products fail to survive the shear force in the flow environment. These data provide important input to those who are designing large macroscopic structures that are to be generated by DNA-mediated self-assembly.

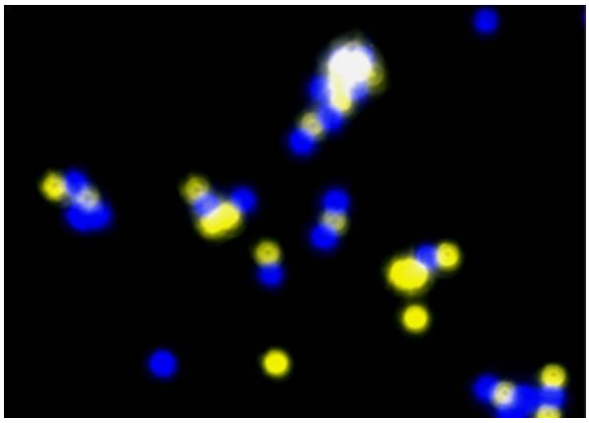

Figure 6.6 Fluorescence micrograph of the assembly of 6 μm A1 beads (blue color) and 6 μm B1 beads (yellow color) in a static hybridization chamber.

6.3.2 DNA Sequence

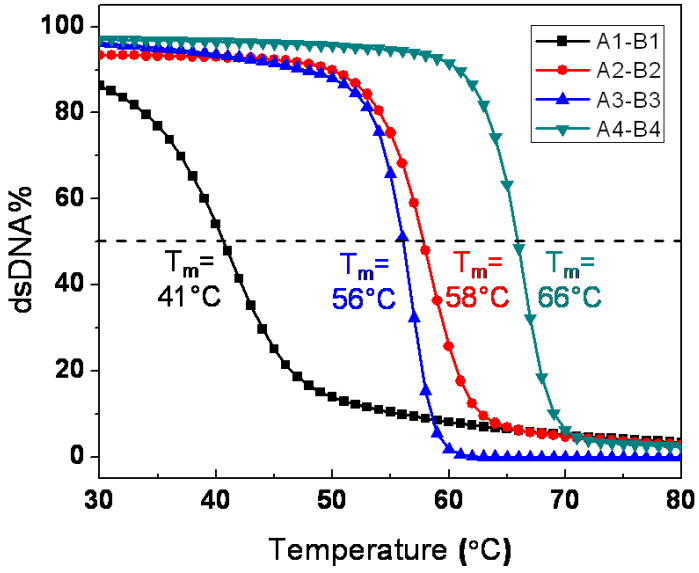

Figure 6.7 Calculated melting curve of DNA A1-B1, A2-B2, A3-B3, and A4-B4. The calculation was based on nearest neighbor model at 10 pM DNA concentration and 0.1M Na^+ concentration.

Imaging flow cytometry was used to investigate the effect of DNA length and melting point on the assembly yield. The calculated melting curves of the four dsDNAs are shown in Figure 6.7. The 18 bp A1-B1 duplex has the lowest melting point of 41 °C. The 25 bp A2-B2 duplex has a melting point of 59 °C, and the 35 bp A4-B4 duplex has the highest melting point of 66 °C. The longest 50 bp A3-B3 DNA duplex has only a melting point of 56 °C because it is entirely composed of adenosine and thymidine.

The double-fluorescence plots and micrographs of the A2-B2, A3-B3, and A4-B4 bead assemblies are shown in Figure 6.8 to Figure 6.10. All three sets of beads gave much larger populations of A-B assemblies than the A1-B1 beads. Moreover, fractions of higher-order assemblies were observed, including clusters with tens of beads in the case of A4-B4 assembly (Figure 6.10). Through examination of the fluorescent micrographs, flow cytometry enabled verification of the fact that these clusters had a precise, alternating arrangement of the two beads. The formation of large clusters indicates that the DNA hybridization force overcame the flow shear. However, the fact that the majority of assemblies were elongated along the flow direction suggests that the shear forces were still comparable with the DNA hybridization force. [113]

Sequence	Length (bp)	mp (°C)	Yield (%)
A1+B1	18+18	41	8.3
A2+B2	25+25	58	62.4
A3+B3	50+50	56	58.9
A4+B4	35+35	66	77.8
B3+C	50+18	NA	0.7

Table 6.2 DNA sequence and assembly yield. The diameter of microspheres was 6 μm and their stoichiometry was 1:1.

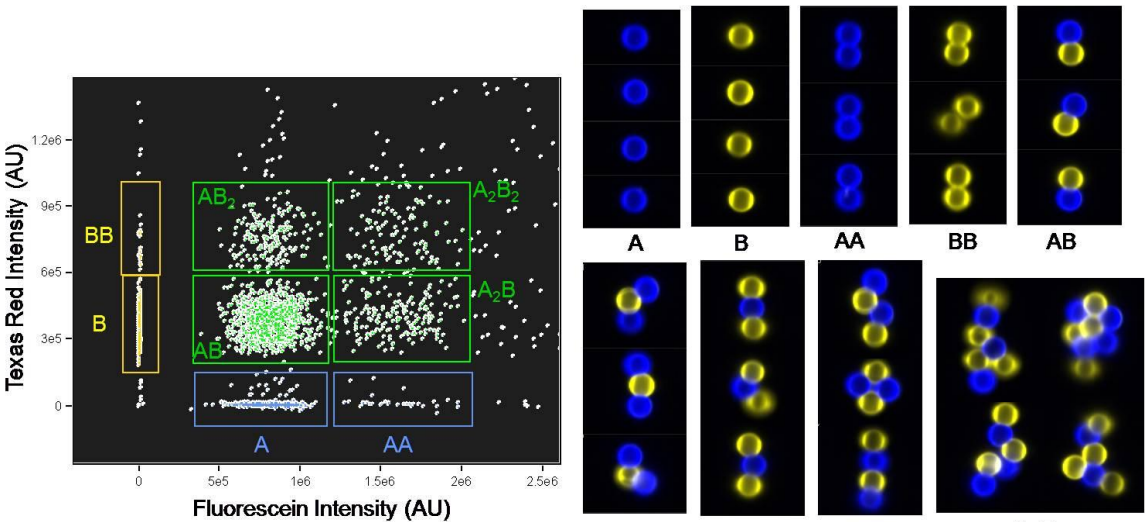

Figure 6.8 Imaging flow cytometry chart and fluorescence micrographs of 6 μm A2-B2 bead assembly. The A2 beads were labeled with fluorescein (blue color) and the B2 beads were labeled with Texas Red (yellow color). The A_mB_n region extends beyond the upright corner, and only part of the region is shown here for clarity.

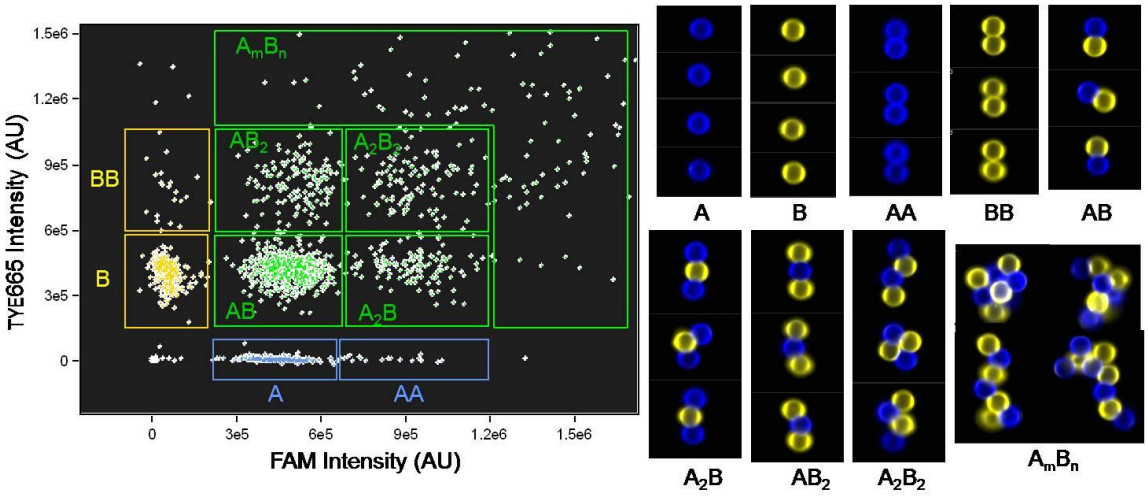

Figure 6.9 Imaging flow cytometry chart and fluorescence micrographs of 6 μm A3-B3 bead assembly. The A3 beads were labeled with FAM (blue color) and the B3 beads were labeled with TYE665 (yellow color). Only part of the A_mB_n region is shown for clarity.

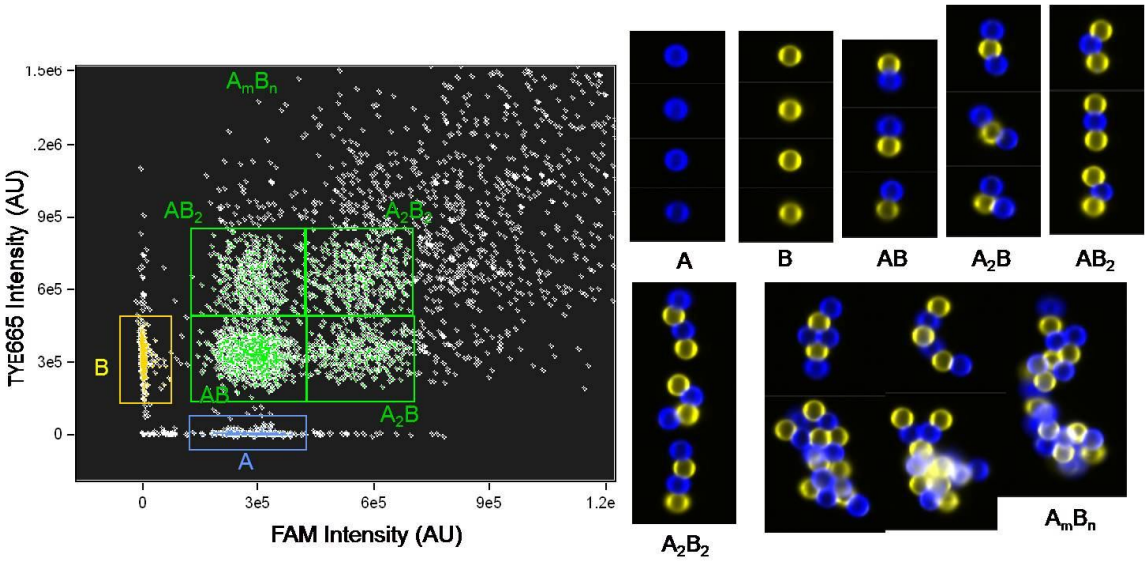

Figure 6.10 Imaging flow cytometry chart and fluorescence micrographs of 6 μm A4-B4 bead assembly. The A4 beads were labeled with FAM (blue color) and the B4 beads were labeled with TYE665 (yellow color). Only part of the A_mB_n region is shown for clarity.

Table 6.2 summarizes the overall assembly yield of the four bead sets. The assembly yield correlates well with DNA melting point. The A1-B1 assembly with the lowest DNA melting point gave an assembly yield of 8.3%; the A2-B2 assembly and A3-B3 assembly with intermediate DNA melting points gave assembly yields of 62.4% and 58.9%, respectively. The A4-B4 assembly with the highest DNA melting point gave the highest assembly yield of 77.8%. Therefore, DNA melting point seems to be an important factor that should be considered in the design of DNA-guided self-assembly of microspheres. It is also important to report that as expected, mixtures of beads with non-complementary sequences showed very little binding to one another (Figure 6.11).

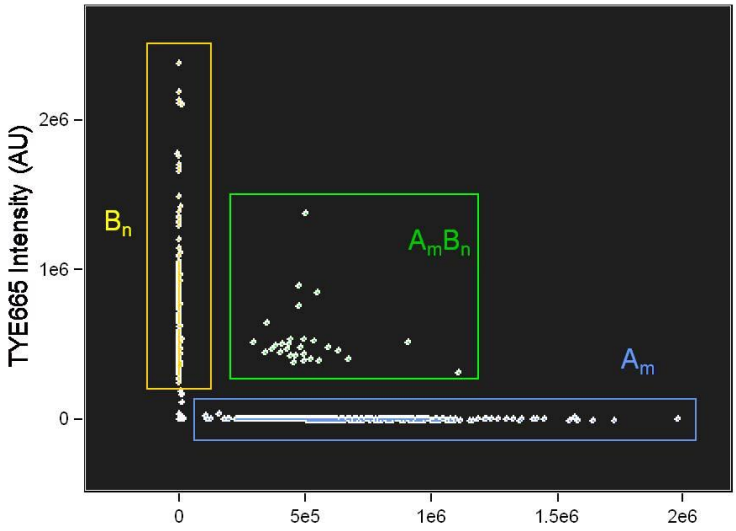

Figure 6.11 Imaging flow cytometry chart of 6 μm B3-C bead assembly as a negative control. Very small assembly fraction was observed (0.7%).

Sequence	A	B	AA	BB	AB	A_2B	AB_2	A_2B_2
A1+B1	37.6%	42.3%	4.9%	7.0%	6.7%	0.5%	0.8%	0.2%
A2+B2	18.8%	16.5%	1.3%	1.0%	38.6%	7.2%	7.1%	4.2%
A3+B3	20.4%	18.8%	0.9%	1.0%	32.1%	6.5%	7.4%	5.5%
A4+B4	10.7%	10.6%	0.4%	0.5%	20.9%	7.1%	7.8%	8.1%

Table 6.3 Detailed yield of each subpopuplations.

The fractions of each subpopulation were counted to gain further insight of the microsphere assembly. Table 6.3 lists the fractions for the four sets of bead assembly. It can be concluded from both Table 6.3 and the flow cytometry diagrams that the bead identity A and B are roughly exchangeable. For example, $[A] \approx [B]$, $[A_2B] \approx [AB_2]$. Therefore, to simplify the analysis, the bead identity is neglected and the bead assemblies are simply identified by the aggregation number:

$[M_1] = [A] + [B]$, $[M_2] = [AB]$, $[M_3] = [A_2B] + [AB_2]$, $[M_4] = [A_2B_2] + [A_3B] + [AB_3]$.

An equilibrium-based reaction scheme is proposed. The equilibrium constant is assumed to be K for all steps except for the first step, where an additional factor α is introduced.

$$M + M \underset{}{\overset{\alpha K}{\rightleftharpoons}} M_2$$
$$M_2 + M \underset{}{\overset{K}{\rightleftharpoons}} M_3$$
$$M_3 + M \underset{}{\overset{K}{\rightleftharpoons}} M_4$$

The fractions for each aggregation size can be calculated as follows:

$$[M_2] = \alpha K[M]^2 \tag{6.4a}$$

$$[M_3] = K[M][M_2] = \alpha K^2[M]^3 \tag{6.4b}$$

$$[M_4] = K[M][M_3] = \alpha K^3[M]^4 \tag{6.4c}$$

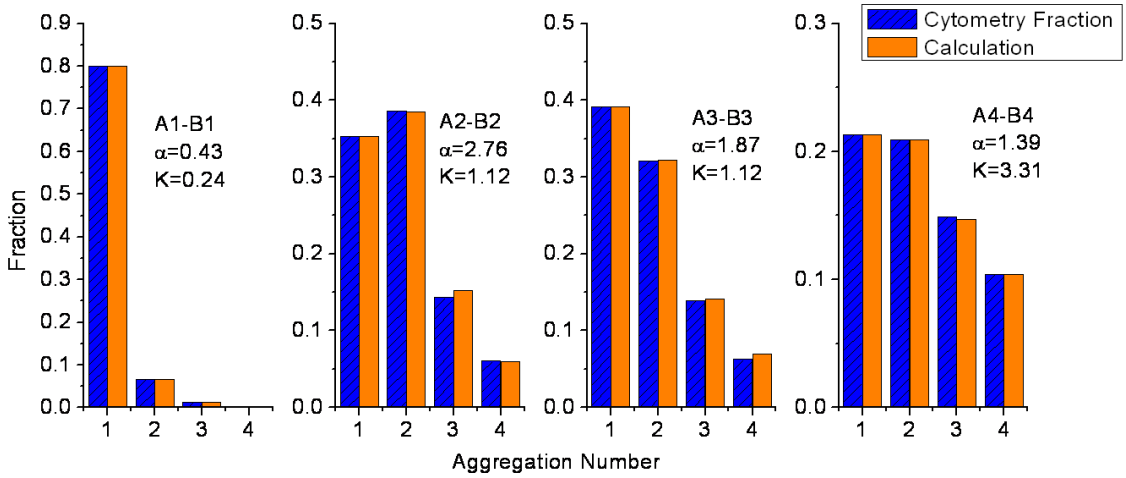

Figure 6.12 Fitting flow cytometry fractions of A1-B1, A2-B2, A3-B3, and A4-B4 bead assembly with equations (6.4a-c).

Interestingly, the flow cytometry fraction data of all the four sets of bead assembly can be fitted well using the simple two-parameter model. The extracted equilibrium constant *K* showed good correlation with DNA melting point. *K* was 0.24 for A1-B1 which has the lowest melting point, and it was 3.31 for A4-B4 which has the highest melting point.

It is somewhat surprising that the equilibrium constant *K* was equal for the second and third step, as one may expect *K* would be larger for a particle cluster with larger surface area. We speculate that the larger particle clusters are also subject to larger shear forces in the flow environment, and thus rendering the apparent *K*s similar for different reaction steps.

6.3.3 Bead Size

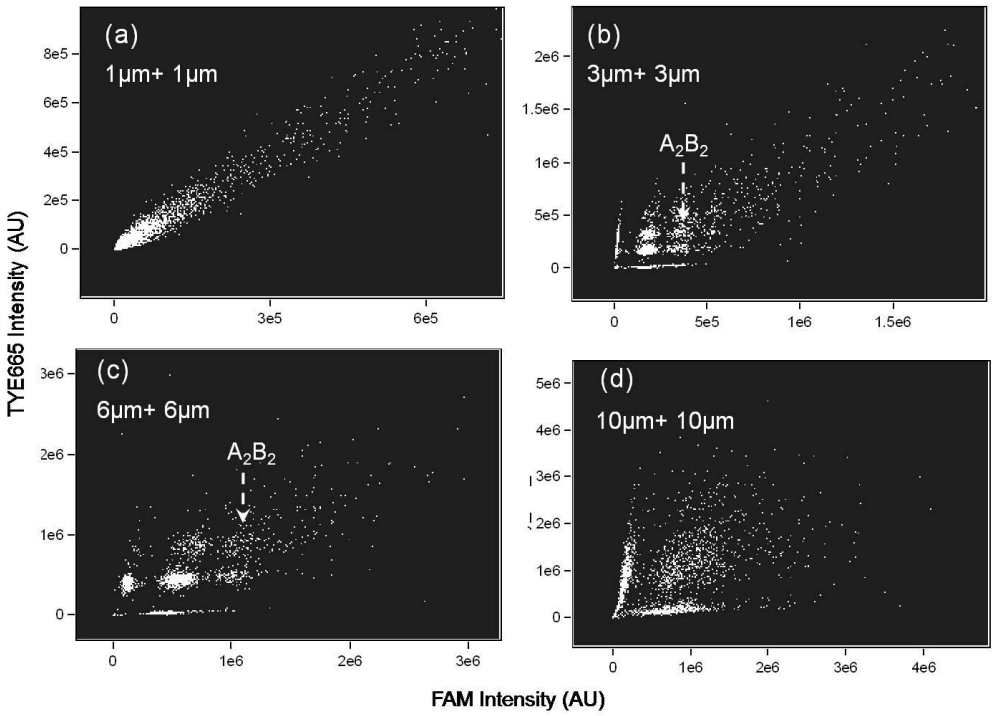

Figure 6.13 Double-fluorescence plot of A3-B3 bead assemblies. (a) 1 µm + 1 µm, (b) 3 µm + 3 µm, (c) 6 µm + 6 µm, (d) 10 µm + 10 µm. The fluorescence intensities were not compensated.

Figure 6.13 shows the double-fluorescence plot of A3-B3 bead assembly with different bead sizes. The above described assembly of 6 μm beads assembly produced significant populations of AB, A_2B, AB_2 and A_2B_2, plus some diffuse population of higher-order assemblies A_mB_n. (Figure 6.13c). The assembly of 3 μm A3-B3 beads gave a similar distribution of AB, A_2B, AB_2 and A_2B_2 (Figure 6.13b), with the A_mB_n region extending further upright, indicating the formation of larger clusters. The assembly populations of 1 μm A3-B3 beads were not well resolved; however, the even longer extension of A_mB_n region indicated the formation of very large clusters. On the other direction, increasing the bead size to 10 μm produced mainly AB dimers (Figure 6.13d). The observation from double-fluorescence plot is further supported by the corresponding fluorescence micrographs (Figure 6.14).

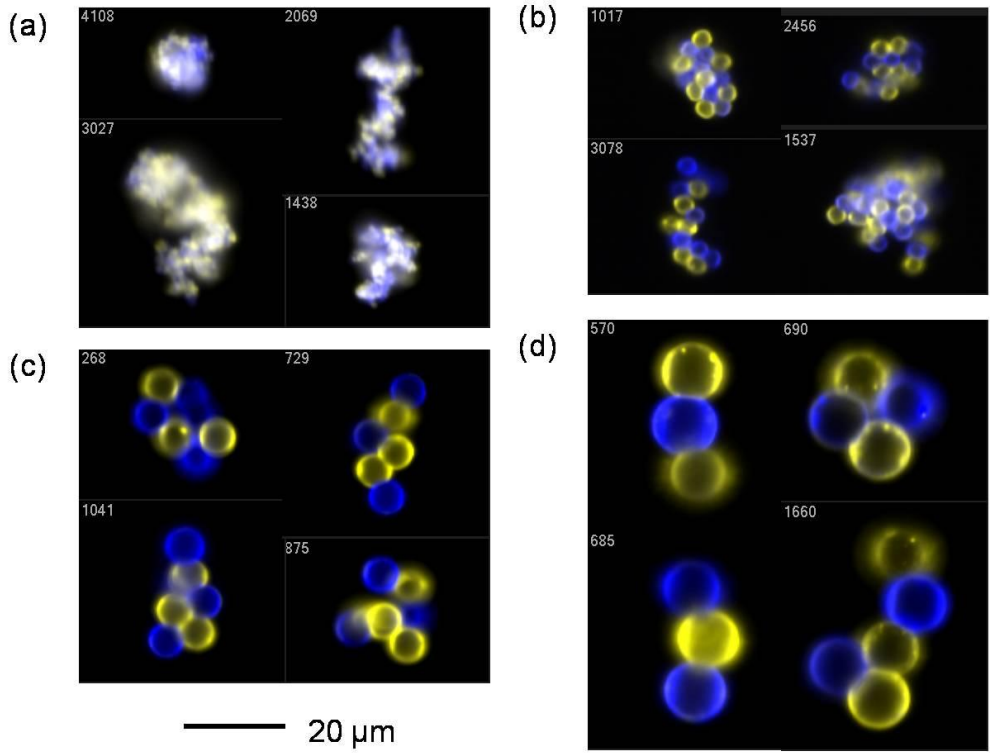

Figure 6.14 Fluorescent micrographs of A3-B3 microspheres with different diameter. (a) 1 μm + 1 μm, (b) 3 μm + 3 μm, (c) 6 μm + 6 μm, (d) 10 μm + 10 μm.

The decrease of particle aggregation number with large beads suggests that flow shear become more dominant at larger scale. As the particle size a increase, flow induced shear force increases with the second power of size:[113]

$$F_{shear} \sim 6\pi\mu\gamma a^2$$

where μ is the viscosity of the fluid media, and γ is the shear rate.

The total DNA hybridization force is proportional to the contact area between two spheres. Due to geometric constraints, the effective contact area does not scale the same as the overall surface area. Considering two spheres in close contact, the effective contact area approachable by DNA strands of length l is given by:

$$A = 2\pi la \text{ , when } l << a$$

Hence,

$$F_{DNA} \sim 2\pi la$$

The slower increase of DNA hybridization force with bead size suggests that mesoscale DNA-guided self-assembly require stronger DNA hybridization interactions. As illustrated by the DNA sequence study described in section 6.3.2, DNA strands with longer length and high melting point are more efficient in driving the self-assembly of micron-sized beads.

6.3.4 Stoichiometry

The success of fitting the assembly fractions with equilibrium conditions (Figure 6.12) suggests that the conversion of bead assembly may be tuned by changing the stoichiometric ratio. Therefore, the effect of bead stoichiometry was tested. Figure 6.15 shows the change in assembly populations that occurred when different ratios of 6 μm A3 and B3 beads were mixed. An excess of A3 bead was found to drive the assembly nearly to completion in a manner similar to Le Chatelier's principle. At an A/B ratio of 0.6, the conversion of B into assemblies was 54.9%, while at an A/B ratio of 9.6, the conversion

of B increased to 98.1%. Increasing the A/B ratio also had a profound effect on the structure of the assembly. When the A/B ratio was close to 1, the major population of the assembly was AB_n (Figure 6.15a,b). As the A/B ratio increased, the population of A_2B_n and A_3B_n began to exceed that of AB_n (Figure 6.15c) and finally became predominant (Figure 6.15d, e).

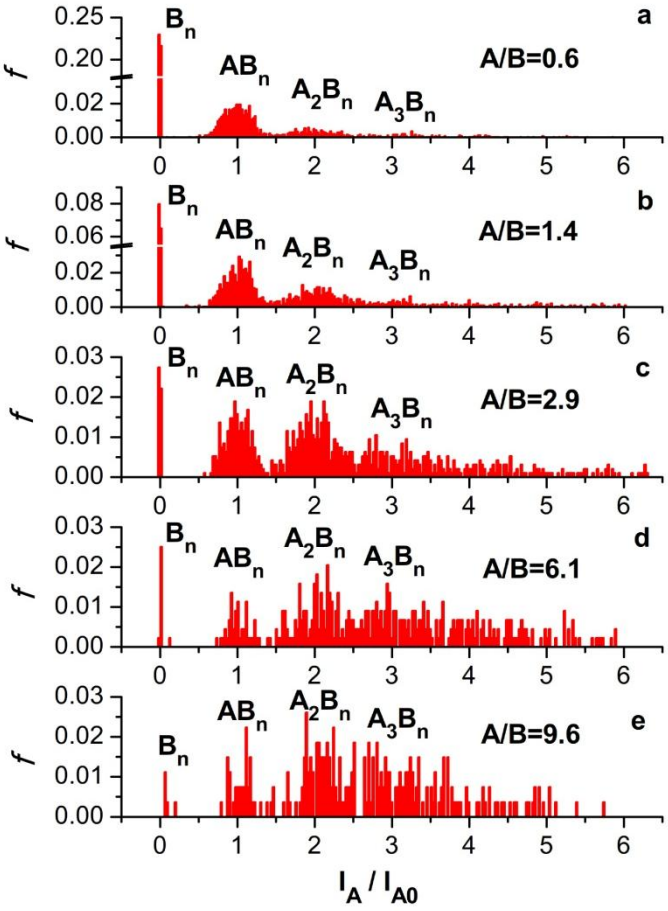

Figure 6.15 FAM fluorescence intensity histogram of assembly products from 6 μm A3 and 6 μm B3 beads. (a) A3/B3 = 0.6, (b) A3/B3 = 1.4, (c) A3/B3 = 2.9, (d) A3/B3 = 6.1, (e) A3/B3 = 9.6. *f*: relative frequency. I_A: FAM fluorescence intensity. I_{A0}: average FAM fluorescence intensity of A3 bead monomer. The ratio I_A/I_{A0} roughly indicates the number of A3 bead in a bead cluster.

6.4 Summary

DNA-guided self-assembly of microspheres was studied using imaging flow cytometry as an analytical tool. Imaging flow cytometry enables quantitative analysis of the assembly process and provides detailed information on the effect of structural and process variables on the assembly yield. The effect of DNA sequence, bead size, and bead stoichiometry was analyzed. The yield of microsphere assembly was found to be dependent on the melting point of DNA. The use of 25bp to 50 bp DNA was sufficient to drive the assembly of microspheres to high yields, forming not only dimers but also chain-like structures. The fractions of assembly products can be explained by chemical equilibrium. An excess of bead "reactant" was able to drive the assembly nearly to completion. The analysis demonstrated that DNA-mediated self-assembly can assemble microspheres of 1-10 μm size and thereby provided important guidelines for the assembly of lithographically patterned particles in the next chapter.

Chapter 7: Fabrication and Self-Assembly of Lithographically Patterned Microparticles

7.1 Process Development

7.1.1 Photomask

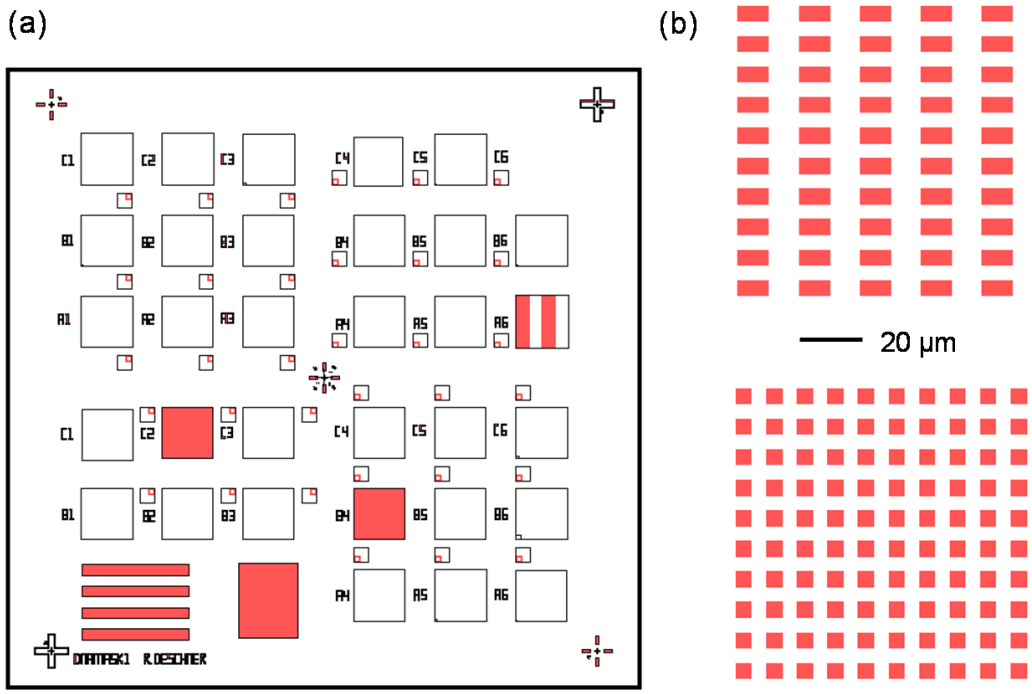

Figure 7.1 Design of photomask. (a) Overview of the mask layout. (b) Arrays of 10 μm × 5 μm rectangles and 5 μm × 5 μm squares.

A chrome-on-quartz photomask was designed to define the particle shapes (Figure 7.1). The mask contains multiple blocks of different arrays, including 10 μm × 5 μm rectangles and 5 μm × 5 μm squares. Each block is about 1 cm × 1 cm in size. In a typical exposure setup, a silicon wafer was cut into ca. 1 cm × 1 cm size to cover the area of one block.

Therefore, each exposure produced 10^5 to 10^7 particles, depending on the size of individual particle.

7.1.2 Lift-off

The photopatterned particles need to be released from the substrate and collected for self-assembly study. As shown in Figure 7.2, a sacrificial lift-off layer was used to facilitate the release and collection of particles.

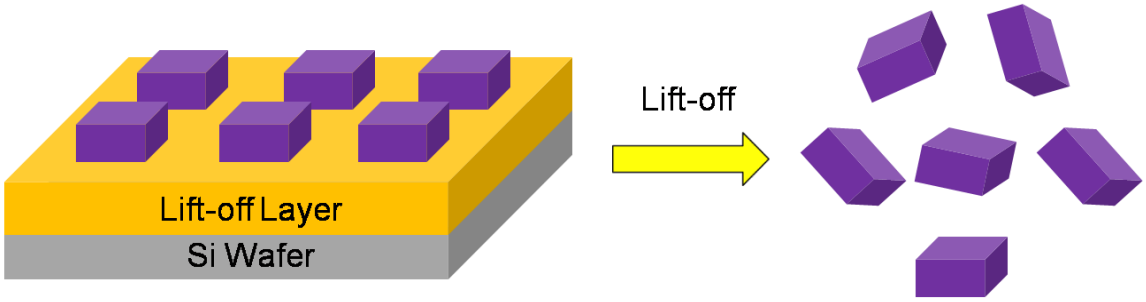

Figure 7.2 The lift-off process. The PMMA copolymer was coated on a lift-off layer and patterned with photolithography. The particles were released from the wafer substrate after dissolving the lift-off layer in an appropriate solvent.

There are several requirements for an ideal lift-off layer. First, it needs to have an orthogonal solvent to PMMA. That is, the casting solvent to spin-coat PMMA does not dissolve the lift-off layer, and the solvent to dissolve the lift-off layer does not dissolve PMMA. There are several non-solvents for PMMA such as water, hexane, alcohols, and diethyl ether, so a water soluble polymer that does not dissolve in common organic solvents will fit this solubility criterion. Another requirement for the lift-off layer is that the polymer needs to have high enough glass transition temperature (T_g) to withstand the baking process. Table 7.1 lists the T_g of several lift-off layer candidates and their lift-off conditions.

Name	Structure	Lift-off media	T_g
poly (acrylic acid) (PAA)	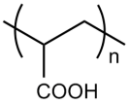	water	105°C (A), 125°C (S)[114]
poly (vinyl pyrrolidone) (PVP)	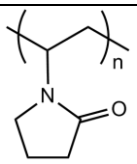	water	185°C[115]
poly (methyl glutarimide) (PMGI)	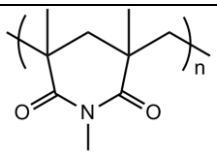	water (basic)	190°C[116]
poly(octadecyl methacrylate) (PODMA)	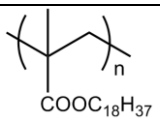	hexanes	-100°C[117]

Table 7.1 Properties of lift-off layers. A: atactic. S: syndiotactic.

The solubility of the four polymers in Table 7.1 was tested. All of the four polymers are insoluble in the PMMA casting solvent PGMEA and therefore fit the solubility criteria. However, the glass transition point (-100°C) and melting point (38°C) of PODMA was too low for spin coating and baking the film stack. PAA, PVP, and PMGI were all successful in film stack coating, exposure, and lift-off. While PAA and PVP are soluble in pure water, PMGI is only soluble in alkaline solution. The unique solubility characteristics of PMGI is particularly useful for the purpose of in situ DNA-conjugation to particles on wafer.

Figure 7.3 shows an example of lithographically patterned polymer particles that were made using the mask block of 5 μm × 5 μm squares. The lift-off layer PAA was partially soluble in the IPA-containing developer, generating the mottled background in Figure 7.3 (a). The particles on the wafer were successfully lifted-off after a water soak, and then

they were collected and concentrated by centrifugation. Figure 7.3 (b) shows a suspension of the collected particles. The particles have a shape close to a 5 μm × 5 μm × 2.5 μm rectangular prism.

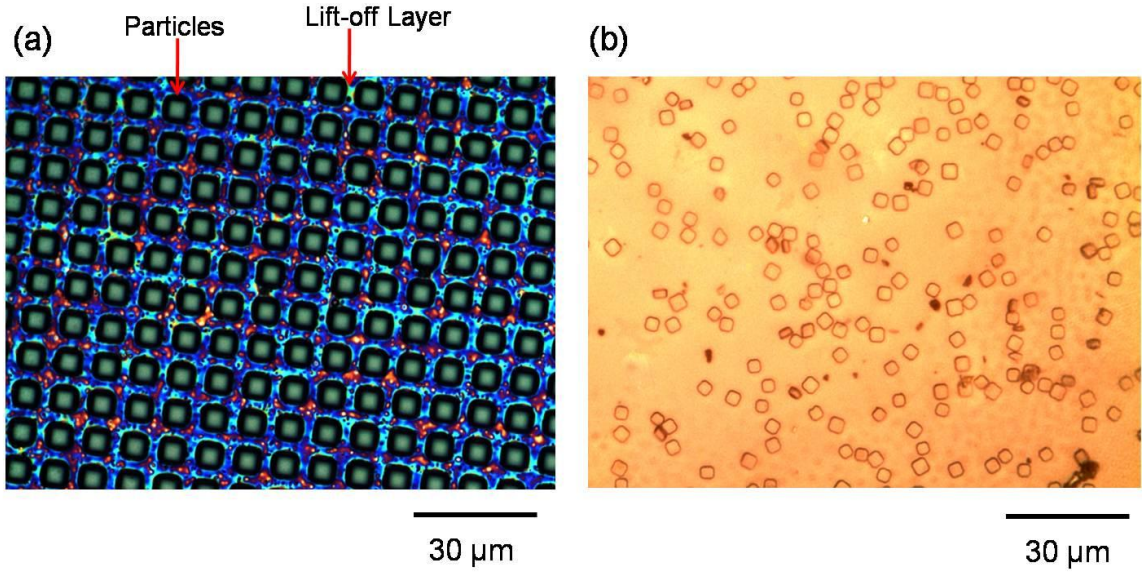

Figure 7.3 Patterning and lift-off of PMMA copolymer. The PMMA-r-PFPMA copolymer on PAA lift-off layer was patterned with the mask pattern of 5 μm × 5 μm square arrays. (a) Micrograph of photopatterned particles on wafer, after the exposure and develop step. (b) Micrograph of the collected particles suspended in water.

7.2 Self-Assembly of Rectangular Particles

7.2.1 Process Overview

A process to fabricate DNA-conjugated rectangular particles was developed (Figure 7.4). The process started with coating of PMMA-r-PFPMA onto PAA, followed by DUV exposure, develop, and lift-off. A DNA conjugation step after lift-off can attach DNA to all six faces of the rectangular particles. Although PMMA-r-PFPMA should react with amine-modified DNA directly, the use of EDC coupling for post-lithographic DNA

conjugation proved more successful. The DNA-conjugated rectangular particles were then studied for the assembly with beads as well as for the assembly between the rectangular particles.

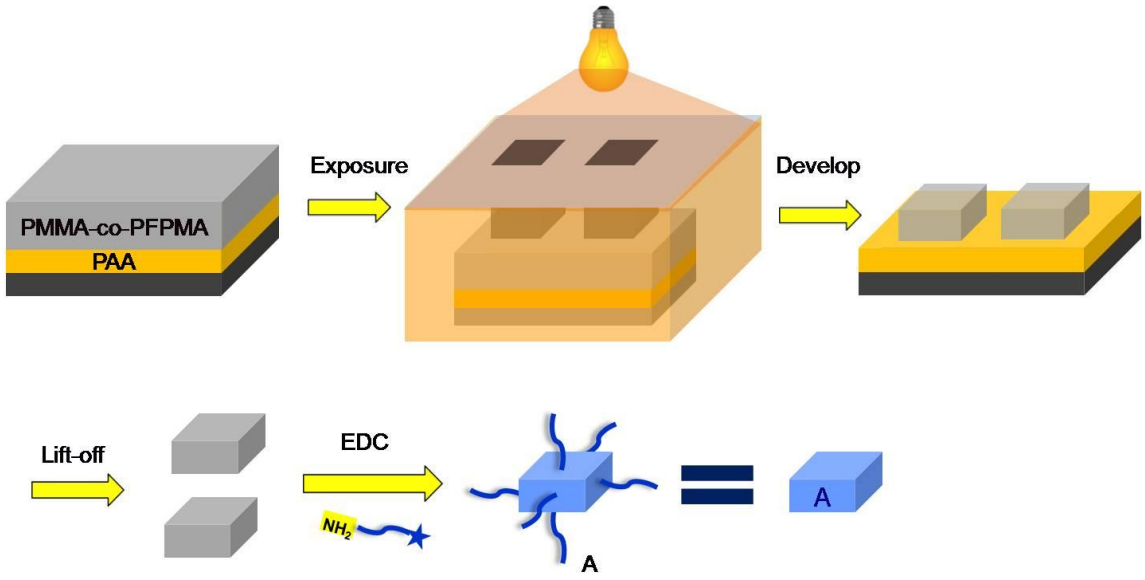

Figure 7.4 Fabrication of DNA-conjugated rectangular particles using photolithography.

7.2.2 Experimental

The lift-off layer PAA was spin-coated from water solution and baked at 110°C for 5 min. PMMA-r-PFPMA film was then spin-coated on top of PAA from a PGMEA solution. The spin-coating of PFPMA was repeated as described previously to build up a film thickness of 2.5 μm. The final film was baked at 160°C for 30 min.

The film-coated wafer was cut into ca. 1 cm × 1 cm pieces and loaded behind the desired pattern block of the mask. The wafer was then exposed to UV light from an Oriel 68810 500W mercury arc lamp. The exposed wafer was developed with 1: 3 MIBK: IPA for 2 min, rinsed briefly with IPA, and then dried under air flow. The wafer was immersed in water with gentle agitation, until the particle lift-off was complete by visual inspection.

The particle suspension contained larger debris structures produced by underexposure of the film due to the nonuniformity of the intensity across the exposure field. To remove such debris, the particle suspension was loaded onto a 30 μm pore-size spin-filter in a 1.5 ml Eppendorf tube. The filtrate was then centrifuged, yielding a visible white aggregation of particles at the bottom of the centrifuge tube. The particles were washed twice by removing the supernatant and replacing with DI water.

The particles were conjugated with amine-modified DNA using the same EDC coupling procedure described for the microspheres, using a conjugation solution containing 100 mM MES buffer (pH 5), 10 μM DNA, and 50 mM EDC. The particle suspension was incubated overnight, and then centrifuged and resuspended three times in 100 μL of 0.4 M TEAB + 0.1% Tween 20 + 2 mM EDTA.

Three other sets of particles were prepared for comparison. Direct amine conjugation was conducted in 100 mM pH 11 carbonate buffer, 10 μM FAM-A3-NH_2 DNA, and 2 mM EDTA. Control set 1 was prepared at the same condition as EDC coupling except to replace the EDC solution with same volume of DI water. Control set 2 was prepared by replacing the 10 μM FAM-A3-NH_2 solution in the direct amine conjugation method with 10 μM of non-amine-modified DNA (FAM-A2-Biotin). The particles were washed with the same procedure as described for the EDC coupling. The DNA sequences used are shown in Table 7.2.

Name	Sequence
FAM-A3-NH_2	/56FAM/ $(AAAAA\ AAAAA)_5$ /3AmMO/
Tye-B3-NH_2	/5TYE665/ $(TTTTT\ TTTTT)_5$ /3AmMO/
FAM-A2-Biotin	/56FAM/ TATGC GTATG TATGC GTGCG TGCGT /3Bio/

Table 7.2 DNA Sequences (5'→3').

For the assembly of lithographically-patterned particles, two batches of 5 μm × 5 μm × 2.5 μm PMMA-r-PFPMA particles were prepared. One batch of the particles were conjugated with FAM-A3-NH_2 by EDC coupling, and the other batch was conjugated with Tye-B3-NH_2 (A3 and B3 are complementary.) The particles were mixed together in a solution of 0.4 M TEAB + 0.1% tween 20 + 2 mM EDTA and placed on a shaker table for 5 min.

7.2.3 Results

EDC coupling was found to provide better DNA density than direct amine conjugation on lithographically patterned PMMA-r-PFPMA particles. As shown in Figure 7.5, EDC coupling gave much higher fluorescence intensities than the control groups, while direct amine conjugation yielded essentially the same fluorescence level as the control groups. The reason why EDC coupling worked better for lithographically patterned particles is not well understood yet. One possible reason is the hydrolysis of PFPMA groups during the lithography and lift-off process. The hydrolysis generates carboxylic acid groups, which are good substrates for EDC coupling.

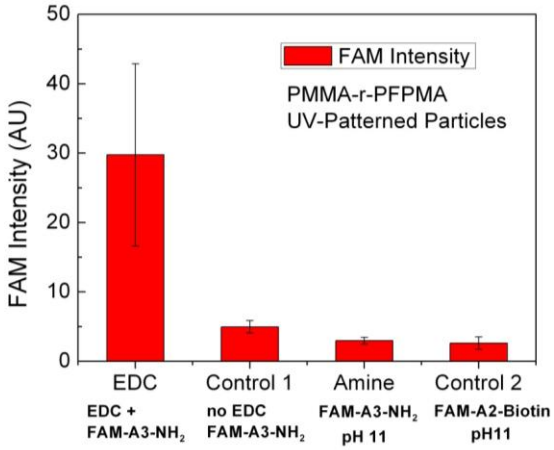

Figure 7.5 Fluorescence intensity of PMMA-r-PFPMA particles prepared with different DNA conjugation conditions.

The presence of DNA on particles prepared by EDC-coupling was further confirmed by assembly with microspheres bearing complementary DNA. As shown in Figure 7.6 (a), the 5 μm A3-conjugated rectangles successfully bound to 3 μm B3-conjugated PS beads (DNA A3 and B3 are complementary, see Table 7.2). The 5 μm rectangles were able to bind with multiple 3 μm beads in most assemble aggregates. As a negative control, the A3 rectangles interacted much less with the A3 beads with identical, non-complementary DNA strands.

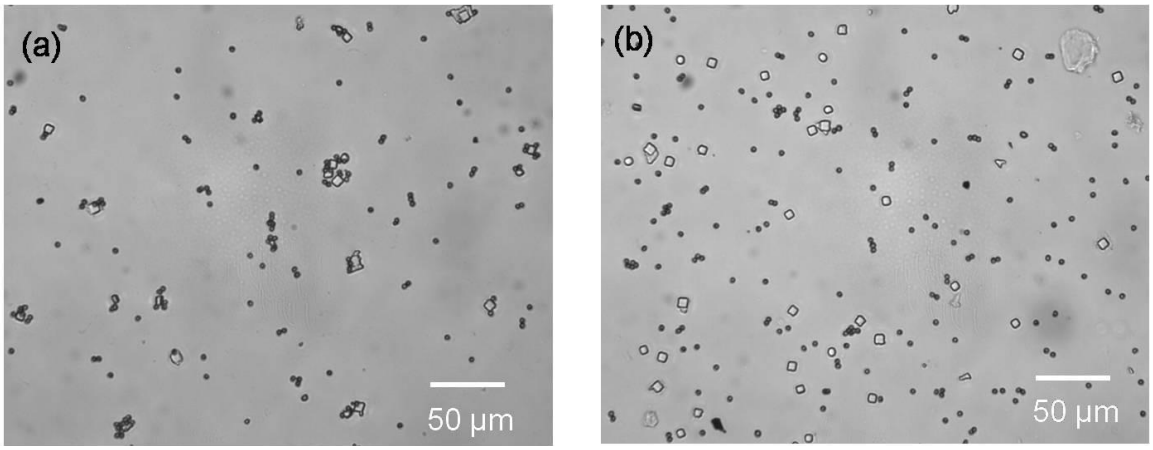

Figure 7.6 Assembly of 5 μm rectangles and 3 μm spheres. (a) Mixture of complementary A3-cubes with B3-spheres formed aggregates. (b) Mixture of non-complementary A3-cubes with A3-spheres as a negative control.

The assembly mixture of rectangles and beads was further studied by imaging flow cytometry. Figure 7.7 shows the flow cytometry plot and fluorescent micrographs of the assembly between 5 μm A3 rectangles (blue color) and 3 μm B3 beads (yellow color). As expected, the rectangles and beads formed a large population of A-B type assemblies. The overall assembly yield was 50.2%, which was comparable with the assembly yield when A3 and B3 microspheres were mixed (58.9%, Table 6.2). The A-B assembly region showed discernible populations of AB, AB_2, and AB_3. Higher-order clusters were also seen, similar to the situation of microsphere assembly. The assembly region was not well

resolved with the blue fluorescence intensity, partially due to broad particle size distribution originating from the uneven light intensity across the exposure field.

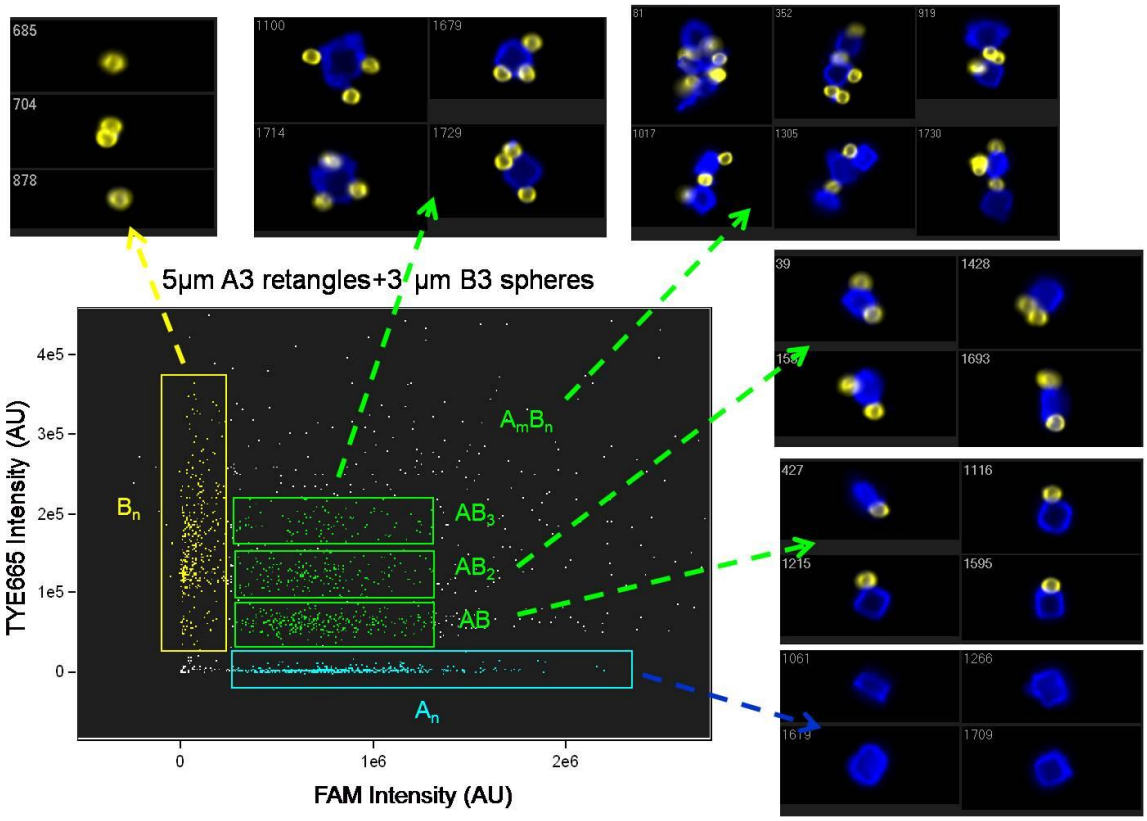

Figure 7.7 Double fluorescence plot and fluorescent micrographs of 5 μm A3-conjugated PMMA-r-PFPMA rectangular prisms assembling with 3 μm B3-conjugated microspheres.

The assembly between rectangles and rectangles was also studied. Figure 7.8 shows the imaging flow cytometry data for the assembly between 5 μm A3 rectangles (blue color) and 5 μm B3 rectangles (yellow color). The assembly population was diffuse due to the broad distribution in particle size and fluorescence intensity. Examination of the fluorescence micrographs revealed that in the majority of the clusters, the rectangles only overlapped partially with each other, rather than forming larger face-to-face contacts. The edge-preference was also observed in rectangle-bead assemblies (Figure 7.6 and 7.7). The edge-preference suggests that flow shear may affect the assembly structure significantly.

It is also possible that the lithographically-patterned particles may have larger roughness at the side walls than at the top and bottom surface, and thus have a higher DNA loading density on sidewalls. The overall assembly yield was 28.5%, which was lower than the yield of rectangle-bead assembly in Figure 7.7 (50.2%).

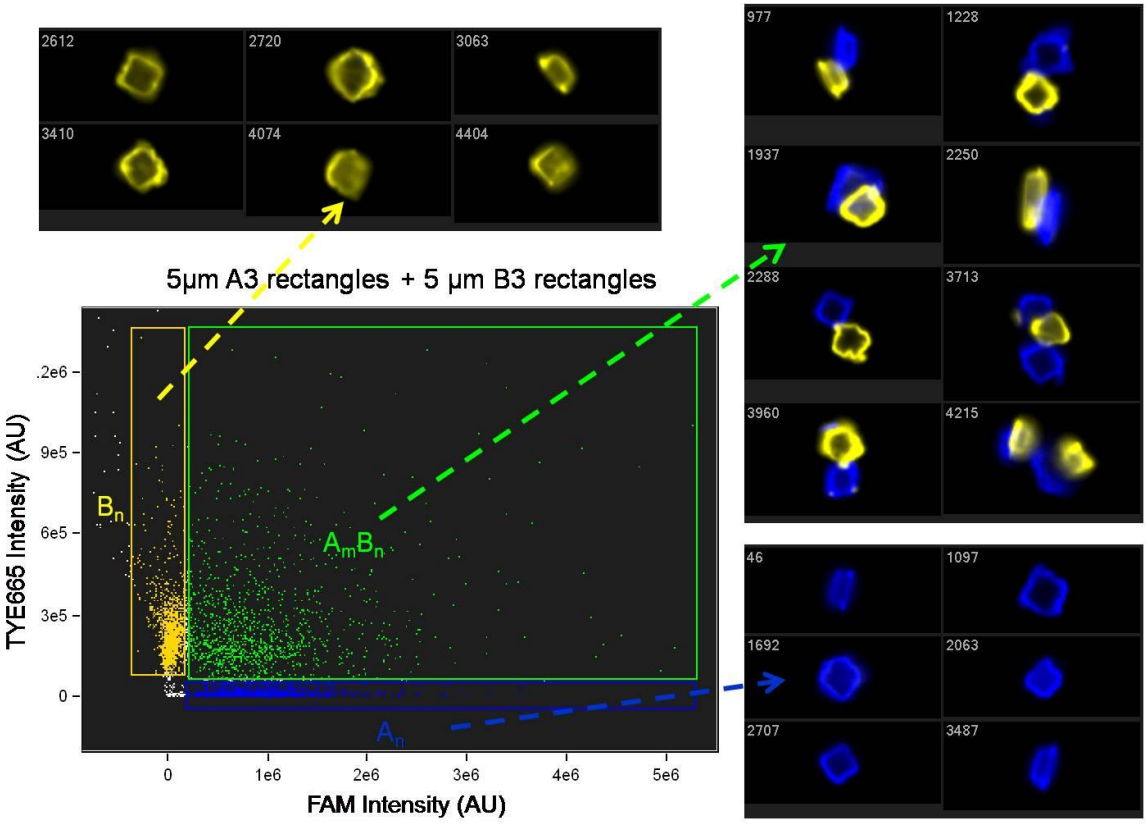

Figure 7.8 Double fluorescence plot and fluorescent micrographs of 5 μm A3-conjugated PMMA-r-PFPMA rectangular prisms assembling with 5 μm B3-conjugated rectangular prisms.

Chapter 8: Conclusions and Future Work

8.1 Conclusions for Liquid Crystalline Semiconductors

Liquid crystalline semiconductors are intriguing materials due to their self-assembly behavior and formation of large LC domains. In this project, the mobility of several LC semiconductors was tested in their LC phases to explore the charge transport behavior in the LC phase.

The LC semiconductors were synthesized by attaching alkyl chains to organic semiconductors such as anthracene and oligothiophene. The phases of these LC semiconductors were characterized by DSC and POM. The anthracenyl esters LCS1 and LCS2 have nematic phases. LCS1 also forms a SmC phase when cooled further from the nematic phase. The oligothiophene- and oligoarenethiophene-based LCs have more ordered smectic or soft crystal phases. The LC phase transition temperature was found to increase with the core size of the molecules.

The charge transport property of the LC semiconductors was measured by the SCLC method and the FET method. The SCLC measurement was performed in LC cells with ITO electrodes. The SCLC mobility of the anthracenyl esters LCS1 and LCS2 rose in their LC phases, while the SCLC mobility for LCS4 and LCS6 dropped in their LC phases. The distinct behaviors may be due to the difference in the domain size of the LCs. The nematic LCS1 and LCS2 forms large-size (>1mm^2) domains in the LC cell. The domain sizes of the smectic LCS4 and LCS6 are smaller and therefore, the mobility in the LC phase does not benefit as much from the reduction in domain boundaries.

Mobility measurements using the FET method provides more meaningful results from the perspective of application. Unfortunately, FET measurements of LCS3, LCS4, LCS6 and LCS7 in their LC phases all showed diminished mobility and degraded output curves.

Similar performance degradation has been observed for the terthiophene liquid crystal LCS3[56] . The difficulty in probing the transistor performance in LC phase may be caused by factors such as the reduced order of LC phases, spinodal dewetting, or the misalignment of LC molecules by electric field.

8.2 Future work for Liquid Crystalline Semiconductors

Mobility measurements in this dissertation were all performed in ambient atmospheres. However, many organic semiconductors, especially the ones with shallow HOMO levels, are sensitive to oxygen. Thermal oxidation at high temperatures may be an issue for LC semiconductors and contributes to the observed mobility drop in the LC phases. Mobility measurement under vacuum or nitrogen is recommended in the future to rule out the possibility of oxidation at high temperatures. Alternatively, the synthesis of room-temperature LC semiconductors can also circumvent the issue of thermal oxidation.

Liquid crystals are generally susceptible to switching by electric field. It is possible that electric field during electric measurements switches LCs into unfavorable molecular orientations. In this regard, an electrical probe station with an add-on polarized optical microscope will be a very useful tool to clarify whether the LCs switch their orientation with the applied voltage during electric measurement.

The high mobility organic semiconductor 2,7-dioctyl[1]benzothieno[3,2-b][1]benzothiophene (C8-BTBT) (Figure 2.1) was also a liquid crystal with a melting temperature near 110 °C .[118] Mobility measurement of C8-BTBT in its LC phase will be a good example for LC charge transport behavior. Importantly, C8-BTBT has high mobility and therefore, the electrical measurements can be performed with smaller voltages and reduce the possibility of orientation switch by electric field.

If the misalignment of LCs in typical FET measurement setup is confirmed by the POM, then the LC phase itself is probably not an ideal phase for transistor operation. Nevertheless, a LC semiconductor may still be useful in that it can be aligned in the LC phase and then cooled back to crystalline phase to provide better transistor operation. The development of smectic LC alignment techniques[119] and the synthesis of high mobility nematic LC semiconductors[46] may fully harvest the benefit of LC self-assembly in the future.

8.3 Conclusions for DNA-Conjugated Microparticles

In this project, photopatternable bioconjugation polymers were synthesized for DNA-guided self-assembly. The copolymerization of PMMA with reactive functionalities afforded photopatternable polymers that are reactive toward DNA conjugation. The use of photolithography in the fabrication of self-assembly building blocks was demonstrated.

The reactivity of the PMMA copolymers was tested in detail using a fluorescence-based test platform. The platform enables quick screening of DNA conjugation conditions such as pH, salt concentration, stoichiometry, etc. The optimized DNA surface density was about 7 pmol/cm^2. The DNA density was adequate to bind with DNA-coated microspheres.

The assembly between DNA-coated microspheres was studied in detail using imaging flow cytometry. The study of DNA-conjugated microspheres verified the specificity of DNA-guided self-assembly and gave important guidelines for assembly conditions such as particle size, DNA sequence, and assembly media. The upper size-limit for DNA guided self-assembly was at least 10 μm when fully complementary DNAs of 25~50 bp length were used.

The contrast curves of the PMMA copolymers were measured and compared. The PMMA-r-PMA copolymer was difficult to pattern but the rest of the copolymers were patterable. A process to fabricate DNA-conjugated rectangular particles using photolithography was developed, including film-stack coating, UV-patterning, lift-off and centrifugation. The lithographically patterned particles showed specific binding with particles with complementary DNAs, which confirms the feasibility of using lithography to fabricate self-assembly building blocks.

8.4 Future Work for DNA-Conjugated Microparticles

Many aspects of this work are worth further investigation. The current assembly yield between lithographically patterned particles is only moderate. The yield needs to be improved to realize larger scale assemblies. The current size of building block is about 5 μm. As shown in Figure 6.14, DNA-guided self-assembly was more successful with smaller particles, although smaller particles are harder to image clearly using optical microscopy. It seems that 3 μm is a good balance between optical resolution and binding interaction. The optimization of the exposure setup to uniformly pattern particles of 3 μm or even smaller size will be the first step to demonstrate a precise and high-yield assembly.

Next, the self-assembly condition can be investigated to optimize the assembly yield and specificity. In the current self-assembly setup, the particles were briefly mixed at room temperature. Thermal anneal followed by slow cooling may be a better strategy to equilibrate the particles and to improve the specificity of self-assembly. The best anneal temperature and cooling rate need to be determined.

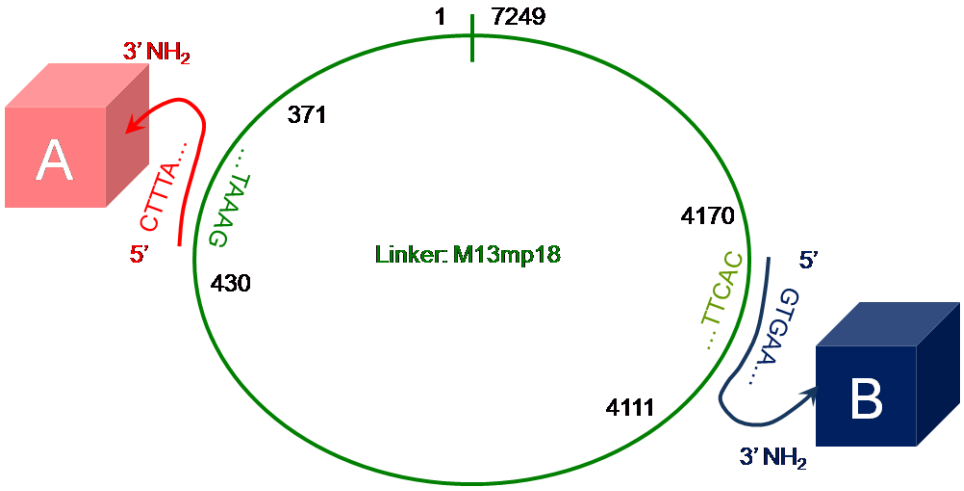

Figure 8.1 Illustration of using M13mp18 DNA as the linker for particle assembly.

Name	Sequence (5'→3')
A	CTTTA CCCTG ACTAT TATAG TCAGA AGCAA AGCGG ATTGC ATCAA AAAGA TTAAG AGGAA /3AmMO/
B	GTGAA TAACC TTGCT TCTGT AAATC GTCGC TATTA ATTAA TTTTC CCTTA GAATC CTTGA /3AmMO/
M13mp18	^{1}AATGC TACTA... ^{371}TTCCT CTTAA... CAGGG TAAAG^{430} ... ^{4111}TCAAG GATTC... GGTTATTCAC^{4170}... TTGGA TGTT^{7249}

Table 8.1 DNA sequence design using M13mp18 DNA as a linker. Superscripts in the sequence of M13mp18 indicates the position.

The current assembly scheme uses two set of particles conjugated with fully complementary DNAs. Further variations of the assembly scheme can be tested. The use of a linker DNA strand to bridge two non-complementary ssDNAs is an attractive strategy. This scheme has the advantage that longer natural DNAs instead of the synthetic DNAs are available, for example, the 7249 bp M13mp18 DNA.[120] The use of long linker DNA may increase the effective contact area between the particles and improve the

assembly yield. Figure 8.1 and Table 8.1 shows a possible DNA design using the circular M13mp18 DNA as the linker.

The creation of multi-facet Janus particles will greatly extend the realm of DNA-guided self-assembly. Several approaches of Janus particle fabrication using photolithography are possible. For example, two different PMMA copolymers can be spin coated into a double stack and it can be pattern with a single step of photolithography (Figure 8.2). If two polymers with orthogonal DNA conjugation chemistries are used, then the particle can in principle, be functionalized with two different DNAs on the top and bottom surface.

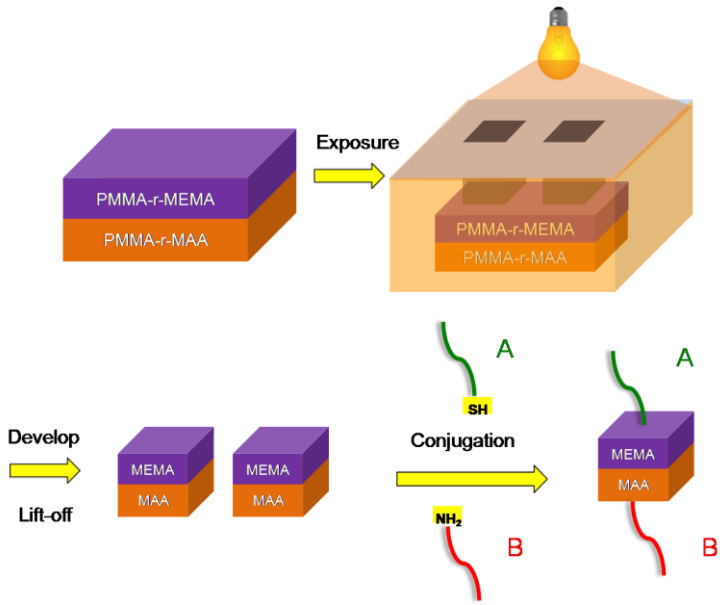

Figure 8.2 Patterning of double-stacked film with orthogonal chemistry.

The double-stack approach has mainly two challenges: layer intermixing and possible cross-functionalization. The layer intermixing problem is illustrated in Figure 8.3. In this experiment, the film stack was spin coated as follows: 570 nm of PAA as lift-off layer from water, 1050 nm of PMMA-r-MAA doped with Nile Red, 850 nm of non-doped PMMA-r-MAA as a buffer layer, and then 1180 nm of PMMA doped with Coumarin 6.

The interlayer bake was 160°C for 5 min and the final bake was at 160 °C for 25 min. The film stack was exposed under the Oriel 68810 UV lamp for 4 min with the 20 μm × 10 μm mask pattern block, and then developed in 1:3 MIBK: IPA for 1 min. The particles were lifted-off in water, collected and imaged by imaging flow cytometry.

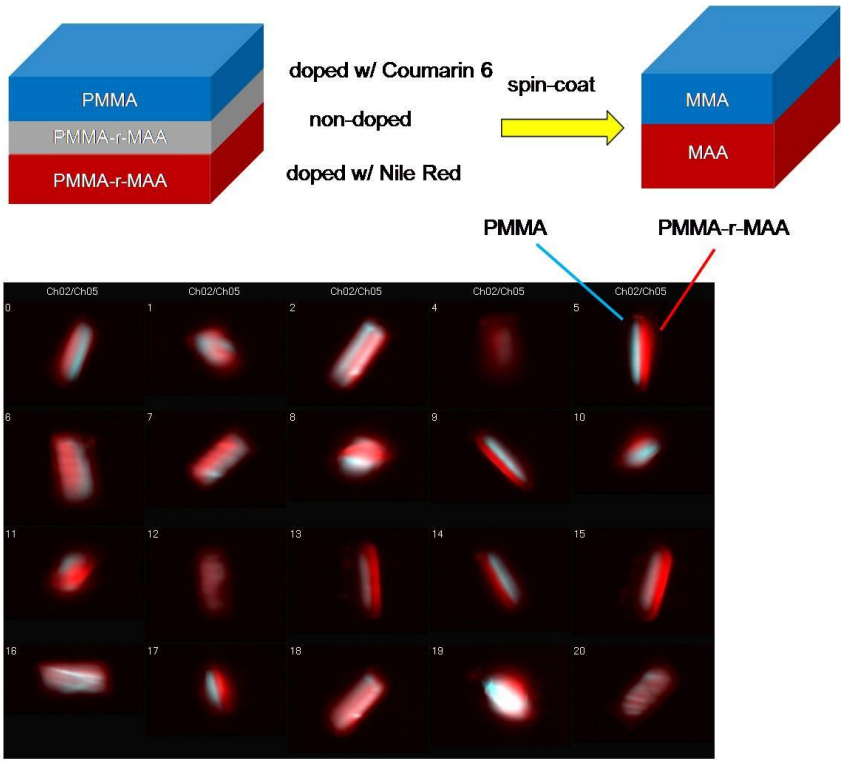

Figure 8.3 Fluorescent micrographs from imaging flow cytometry showing the printed double stack of PMMA and PMMA-r-MAA. A non-doped PMMA-r-MAA layer was used to reduce intermixing.

A dark non-fluorescent layer should be seen if no interlayer mixing happens. However, the flow cytometry micrographs in Figure 8.3 did not reveal the non-fluorescent buffer layer, indicating significant intermixing or diffusion happened during the spin coating and baking process. Nevertheless, the presence of two distinct layers in a particle suggests that lithographical patterning of double-stack Janus particles is feasible. The

spin-coating solvent, baking temperature, and developer need to be further optimized in the future to minimize the intermixing problem.

The issue of cross hybridization is shown in Figure 8.4. In this experiment, the patterning of PMMA-r-MEMA and PMMA-r-MAA double layer (Figure 8.2) was attempted to check the possibility to attach HEX-DNA-SH exclusively to the PMMA-r-MEMA layer and to attach Cy5-DNA-NH_2 exclusively to the PMMA-r-MAA layer. Figure 8.4a shows the bright field optical micrograph of the MEMA/MAA particles. The particles have a "rimmed" appearance with the MEMA layer having a larger area than the MAA layer, which is caused by the higher photosensitivity and dissolution rate of the MAA layer than the MEMA layer (Figure 4.14 and 4.15). An ssDNA with Cy5 and amine modification was then conjugated to the Janus particle. One may expect that the EDC coupling of Cy5-DNA-NH_2 would be more successful on the MAA layer. However, it was found that more DNA was conjugated to the MEMA layer instead (Figure 8.4b). The unexpected conjugation of amine-modified DNA to PMMA-r-MEMA under the EDC coupling condition is not well understood yet.

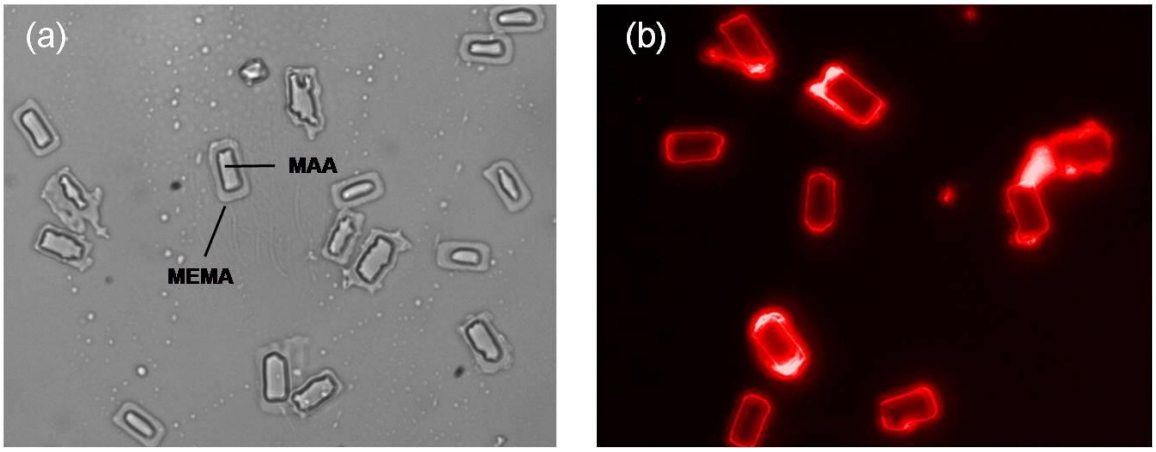

Figure 8.4 (a) Bright field micrograph and (b) Fluorescent micrograph of the PMMA-r-MEMA/PMMA-r-MAA double stack particles. The two images were taken at different sample locations.

The stepwise patterning and DNA conjugation approach to fabricate Janus particles was also attempted. The major challenges of this approach include the blocking of the remaining functionality groups after DNA conjugation, and the possible degradation of DNA and the DNA-conjugation functionality under UV-light. The importance of blocking is explained in Figure 8.5. The yield of DNA conjugation reaction is usually not 100%. Therefore, the residual sites need to be blocked before the next DNA conjugation reaction.

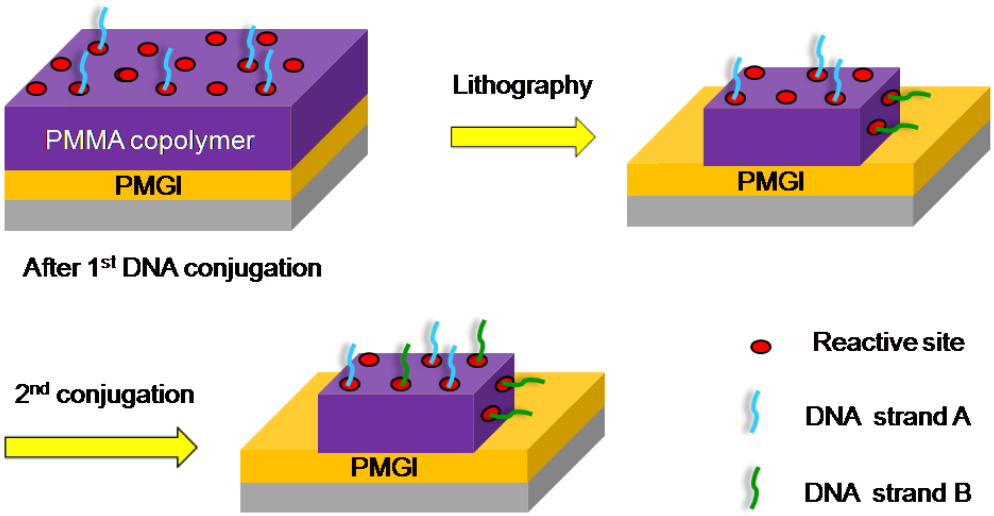

Figure 8.5 Blocking of residual reactive sites is generally required in the stepwise patterning and DNA conjugation approach.

The blocking of the three copolymers with good photopatterning and DNA conjugation properties was investigated, namely, PMMA-r-MEMA, PMMA-r-PFPMA, and PMMA-r-MAA. Figure 8.6 shows the blocking efficiency and the corresponding fluorescent scanning graphs of the blocking experiment. PMMA-r-MEMA was easily blockable with various thiols, for example, 11-mercapto-1-undecanol. The direct reactivity with amine of PMMA-r-PFPMA is blockable with amines such as n-pentylamine. However, the blocking of the PMMA-r-PFPMA is complicated by the fact that EDC coupling was actually used for the DNA conjugation to lithographically patterned particles. The n-

pentylamine treatment with PMMA-r-PFPMA was found to be inadequate to block EDC coupling. No efficient blocking formulation of the EDC coupling reaction to the PMMA-r-MAA polymer has been found yet. The reaction was marginally blockable with ethyleneglycol vinylether. The blocking of the EDC coupling reaction requires further investigation in the future.

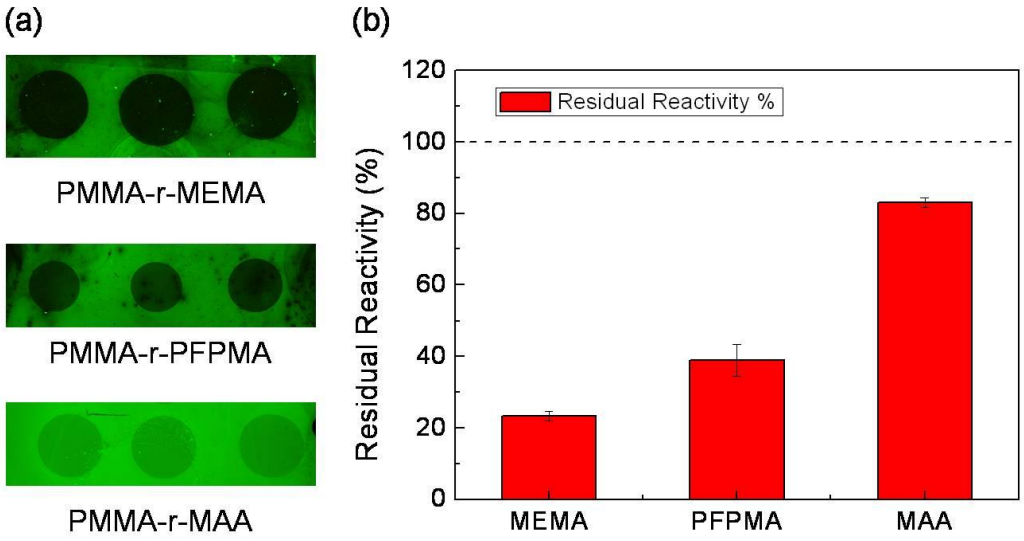

Figure 8.6 Blocking test on the polymers coated on microslides. In this experiment, the polymer was first treated with the blocking solution. (a) Fluorescent scanning images. (b) Quantified ratio of the remaining fluorescence intensity after blocking. Blocking conditions: PMMA-r-MEMA: 0.5 mM 11-mercapto-1-undecanol, 1× SSC, 2 mM EDTA, 10 μM TCEP. PMMA-r-PFPMA: 5 mM n-pentylamine, 0.1 M pH 11 buffer. PMMA-r-MAA: 1 M ethyleneglycol vinylether, 1 mM p-toluenesulfonic acid.

Figure 8.7 shows a process flow to fabricate particles with different DNAs on the top and the side surface. The blockable polymer PMMA-r-MEMA was selected for the process. After the fabrication of the particles, the assembly with complementary beads was tested. The flow cytometry diagram and fluorescent micrographs are shown in Figure 8.8. Essentially no bead binding was observed to the top surface (yield 0.34%). The binding of beads to the side surface was also quite moderate (yield 9.9%). The low binding yield

at the top surface suggests that the DNA on the top surface failed to survive the UV patterning. The DNA degradation may be due to substrate heating or scattered UV irradiation in the lithography process. The development of more photosensitive polymers may be necessary for the successful patterning of DNA-conjugated polymer films. A better temperature control system or the use of anti-reflective coatings on the substrate may also reduce the thermal or photochemical degradation of DNA.

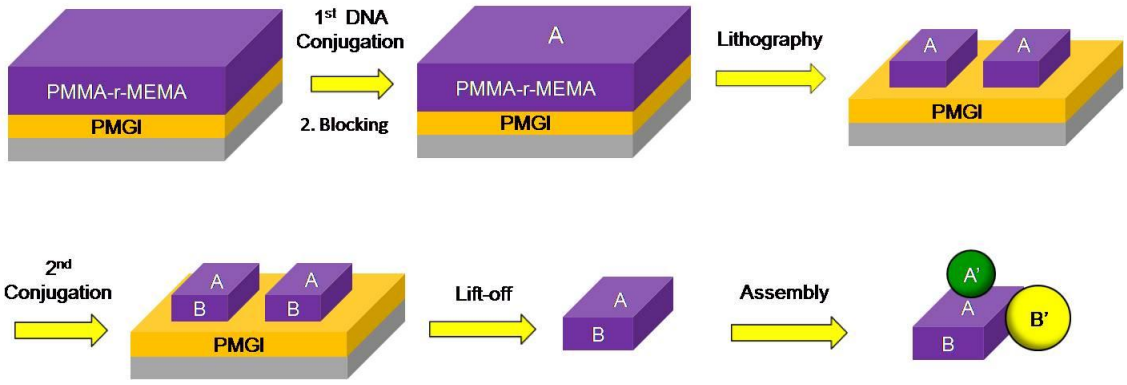

Figure 8.7 A process flow to fabricate particles with distinct top and side surfaces. The DNA sequences are shown in Table 8.2. The PMMA-r-MEMA polymer was doped with coumarin 314.

Name	Sequence (5'→3')
A	$(TTTTT\ TTTTT)_5$ /3ThioMC3-D/
B	/5FAM/CCTCC CCTTT TATGC GTATG TATGC GTGCG TGCGT /3ThioMC3-D /
A'	/56FAM/ $(AAAAA\ AAAAA)_5$ /3AmMO/
B'	/5TYE665/ACGCA CGCAC GCATA CATAC GCATA AAAGG GGAGG /3AmMO/

Table 8.2 DNA sequences used in the stepwise lithography and DNA conjugation approach in Figure 8.7.

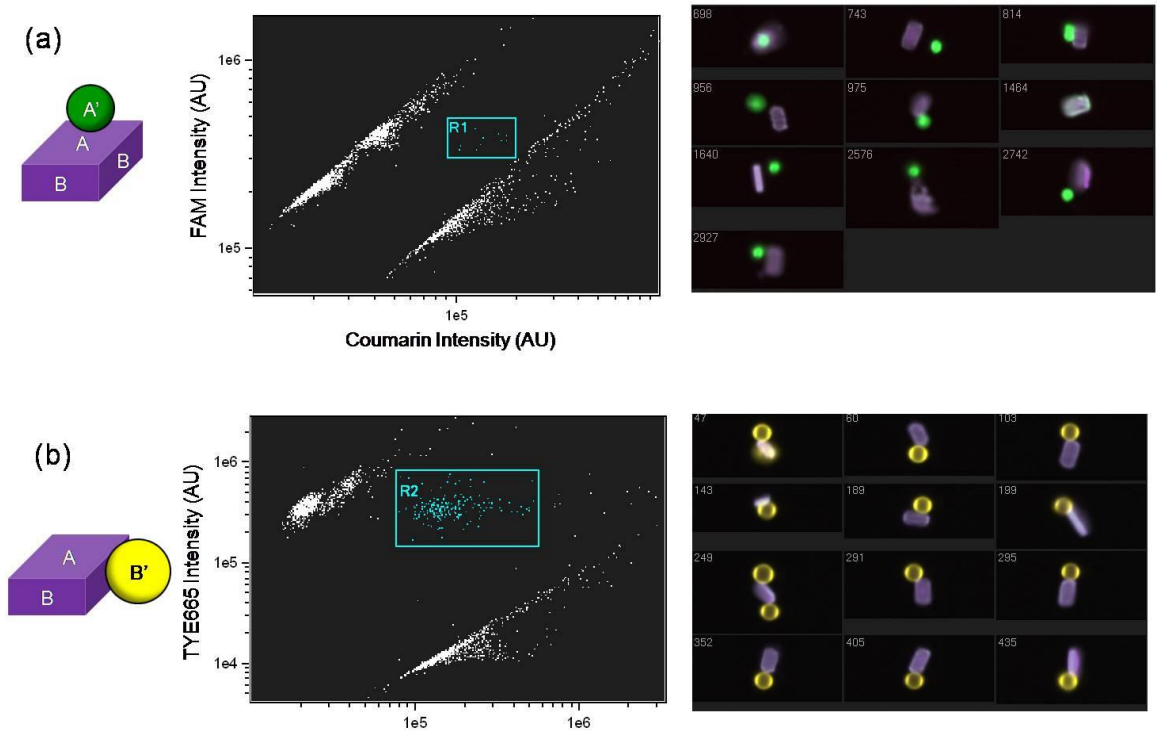

Figure 8.8 Binding of 10 μm × 5 μm topA-sideB particles with (a) 3 μm A' microspheres and (b) 6 μm B' microspheres.

When the assembly of particle dimers is achieved with high yield and specificity, the DNA-guided self-assembly strategy may be extended to achieve larger scale and more complex structures. The self-assembled structures will provide access to a broad spectrum of applications. For example, the porous nature of the microsphere assembly may provide a path to low-k dielectric materials for microelectronics[121]. Self-assembled amorphous materials are also receiving a great deal of attention as battery electrodes[122] and hydrogen storage materials[123]. The concept of metamaterials based on the continuous tuning of mesoscale building blocks has been proposed,[124] giving exotic properties such as invisible cloaking[125] and optical illusion.[126] The precise manipulation of building blocks with DNA may be useful to the fabrication of such metamaterials.

Appendix A: Synthesis Procedures for Organic Semiconductors

General. All reagents and chemicals were purchased from commercial sources and used as received unless specified. Dry dichloromethane (DCM), toluene, pyridine, and triethylamine (TEA) were obtained by distillation over CaH_2. Dry methanol, diethyl ether, tetrahydrofuran (THF), and dimethylformamide (DMF) were obtained from a solvent delivery system under argon atmosphere. Nuclear magnetic resonance (NMR) spectra were recorded on a Varian Unity +300 spectrometer. Chemical shifts (δ) were reported in parts per million, and the residual solvent peak was used as an internal standard. 5,5"-dioctyl-2,2':5',2"-terthiophene[127] (LCS3) and 2,6-anthracenyl bistriflate[128] was synthesized according to literature procedures. 5,5'"-dioctyl-2,2':5',2":5",2'"-quaterthiophene (LCS4) was kindly supplied by Dr. Patrice Rannou with CEA-Grenoble, France.

Anthracene-2,6-diol (3.2). Anthraflavic acid (5.0 g, 20.8 mmol) was suspended in 250 ml 0.4M aqueous Na_2CO_3 solution, and sodium borohydride (9.0 g, 238 mmol) was added portionwise. The suspension was heated to boiling for 5 min and then cooled to 80°C. An additional fraction of sodium borohydride (1.0 g, 26.4 mmol) was added and the reaction mixture was stirred for 5 min. The reaction was cooled to 0°C and carefully acidified with cold concentrated HCl. A yellow precipitate formed and it was collected by filtration, washed thoroughly with water, and dried (3.0g, 68%). The product was stored under nitrogen at 4°C. ^{1}H NMR (300 MHz, d_6-acetone): 8.78 (b, 2H), 8.14 (s, 2H), 7.84 (d, 2H), 7.23 (s, 2H), 7.13 (dd, 2H); ^{13}C NMR (300 MHz, d_6-DMSO): 154.3, 131.5, 129.8, 128.5, 123.7, 121.1, 107.4. HRMS: calcd. 210.0681, found 210.0682.

Anthracene-2,6-diyl bis(4-(octyloxy)benzoate) (3.4, LCS1). 4-(octyloxy)benzoic acid (0.7 g, 2.4 mmol) was dissolved in 4.4 ml thionyl chloride and refluxed under nitrogen for 3 hr. Excess thionyl chloride was removed by rotary evaporation to give crude 4-

(octyloxy)benzoyl chloride **(3.3)**. Anthracene-2,6-diol (0.25 g, 1.2 mmol) was dissolved in 4 ml dry pyridine, and the benzoyl chloride **3.3** was added dropwise, followed by 0.8 ml of dry TEA. After heating at 95°C overnight, the reaction mixture was cooled to room temperature, poured into 150 ml 2% HCl, and extracted with DCM three times. The combined organic extract was washed with aqueous Na_2CO_3, water, brine, dried over $MgSO_4$, and evaporated to dryness. Column chromatography on silica gel (hexanes: DCM 3: 2→ 1: 2) followed by recrystallization in chloroform: methanol yielded yellow crystals (192 mg, 24%). ^{1}H NMR (300 MHz, $CDCl_3$): 8.41 (s, 2H), 8.19 (d, 4H), 8.02 (d, 2H), 7.82 (d, 2H), 7.35 (dd, 2H), 6.99 (d, 4H), 4.05 (t, 4H), 1.82 (m, 4H), 1.5-1.2 (b, 20H), 0.88 (t, 6H). HRMS: calcd. 674.3607, found 674.3616. DSC data was reported on page 22.

2,6-bis(octyloxy)anthracene-9,10-dione (3.5) and 2-hydroxy-6-(octyloxy)anthracene-9,10-dione (3.6). A suspension of anthraflavic acid (2.0 g, 8.3 mmol), octyl bromide (1.44 ml, 8.3 mmol), potassium carbonate (1.15 g, 8.3 mmol) and potassium iodide (16 mg, 0.1 mmol) in DMF (130 ml) was refluxed overnight under nitrogen. After cooling, the mixture was poured into 1M HCl, extracted with DCM, washed with water, brine, dried over $MgSO_4$, and concentrated. The crude solid was purified by column chromatography (hexanes: DCM 2: 3, then DCM: acetone 2: 1) to give **3.5** as yellow crystals (1.23 g, 32%) and **3.6** as a yellow solid (0.40 g, 14%). **3.5.** m.p. 104~106°C (Lit.[129] 105~106°C). ^{1}H NMR (300 MHz, $CDCl_3$): 8.20 (d, 2H), 7.68 (d, 2H), 7.19 (dd, 2H), 4.12 (t, 4H), 1.81 (m, 4H), 1.5-1.2 (b, 20H), 0.86 (t, 6H). HRMS: calcd. 464.2927, found 464.2917. **3.6.** m.p. 141~142°C. ^{1}H NMR (300 MHz, d_6-DMSO): 11.01 (s, 1H), 8.05 (m, 2H), 7.52 (s, 1H), 7.47 (s, 1H), 7.35 (d, 1H), 7.18(d, 1H), 4.14 (t, 2H), 2.01 (m, 2H), 1.45-1.15 (b, 10H), 0.84 (t, 3H). HRMS: calcd. 352.1675, found 352.1669.

6-(octyloxy)anthracen-2-ol (3.7). 2-hydroxy-6-(octyloxy)anthracene-9,10-dione (0.4 g, 1.14 mmol) was dissolved in 10 ml IPA and 20 ml aqueous 1M Na_2CO_3. Sodium borohydride (0.8 g, 21.1 mmol) was added and the reaction mixture was heated to 80°C

for 2h under nitrogen. The reaction was cooled to 0°C and carefully acidified with cold concentrated HCl. A yellow precipitate formed and it was collected by filtration, washed thoroughly with water, and dried (0.26 g, 71%). m.p. 138~139 °C (decomposition). ^{1}H NMR (400 MHz, d_6-DMSO): 9.73 (s, 1H), 8.24(s, 1H), 8.17(s, 1H), 7.85 (m, 2H), 7.28 (s, 1H), 7.16 (s, 1H), 7.11(s, 1H), 7.09 (s, 1H), 4.08 (t, 2H), 1.78 (m, 2H), 1.55-1.2 (b, 10H), 0.86 (t, 3H). HRMS: calcd. 322.1933, found 322.1932.

6-(octyloxy)anthracen-2-yl 4-heptylbenzoate (3.8, LCS2). 6-(octyloxy)anthracen-2-ol (0.25 g, 0.78 mmol) was dissolved in 20 ml dry pyridine under nitrogen atmosphere. 4-heptylbenzoyl chloride (0.25 ml, 1.05 mmol) was added, followed by 1 ml of dry TEA. After heating at 95°C overnight, the reaction mixture was cooled to room temperature and concentrated. DCM was added, and the organic layer was washed sequentially with dilute HCl, aqueous Na_2CO_3, water, and brine, dried over $MgSO_4$, and evaporated to dryness. The crude product was purified by silica gel column chromatography (hexanes: toluene 2: 1) and recrystallized from acetone to give **3.8** as light yellow crystals (0.27 g, 55%). ^{1}H NMR (400 MHz, $CDCl_3$): 8.29 (d, 2H), 8.18 (d, 2H), 7.99 (d, 1H), 7.88 (d, 1H), 7.78 (d, 1H), 7.30-7.36 (m, 3H), 7.16-7.20 (m, 2H), 4.12 (t, 2H), 2.72 (t, 2H), 1.88 (m, 2H), 1.67 (m, 2H), 1.53 (m, 2H), 1.25-1.45 (b, 16H), 0.90 (m, 6H). HRMS: calcd. 524.3290, found 524.3297. DSC data was reported on page 22.

1,4-bis(5-hexylthiophen-2-yl)benzene (3.9, LCS5). To a round bottom flask was added 1,4-dibromobenzene (236 mg, 1 mmol) and K_3PO_4 (637 mg, 3 mmol). Tetrakis(triphenylphosphine)palladium(0) ($Pd(PPh_3)_4$) , 116 mg, 0.1 mmol) was added to the flask in a glovebox under argon. A solution of 5-hexyl-2-thiopheneboronic acid pinacol ester (0.9 ml, 3 mmol) in 50 ml dioxane was degassed through 3 freeze-pump-thaw cycles, and then tranfered to the reaction mixture. The reaction was refluxed under nitrogen for 2 days, cooled to room temperature, concentrated, and diluted with DCM. The DCM solution was washed with water, 1M HCl, and brine, dried over $MgSO_4$, and concentrated. The concentrate was purified by silica gel column chromatography

(hexanes: DCM 9: 1) and recrystallized twice from ethyl acetate: ethanol to give **3.9** as white crystals (140 mg, 34%). ^{1}H NMR (300 MHz, $CDCl_3$): 7.54 (s, 4H), 7.13 (d, 2H), 6.75 (d, 2H), 2.82 (t, 4H), 1.71 (m, 4H), 1.24-1.46 (b, 12H), 0.91 (t, 6H). ^{13}C NMR (300 MHz, $CDCl_3$): 146.0, 141.5, 133.6, 126.0, 125.3, 122.8, 31.9, 30.5, 29.1, 22.8, 14.4. HRMS: calcd. 410.2102, found 410.2101. DSC data was reported on page 23.

2,6-bis(5-hexylthiophen-2-yl)naphthalene (3.10, LCS6). To a round bottom flask was added 2,6-dibromonaphthalene (429 mg, 1.5 mmol) and Na_2CO_3 (477 mg, 4.5 mmol). $Pd(PPh_3)_4$ (87 mg, 0.075 mmol) was added to the flask in a glovebox under argon. A solution of 5-hexyl-2-thiopheneboronic acid pinacol ester (1.35 ml, 4.5 mmol) in 40 ml dimethoxyethane and 15ml water was degassed through 3 freeze-pump-thaw cycles, and then tranfered to the reaction mixture. The reaction was refluxed under nitrogen for 3 days, cooled to room temperature, and poured into dilute HCl. The mixture was extracted with DCM 3 times, and the organic layer was washed with aqueous Na_2CO_3 and dilute HCl, dried over $MgSO_4$, and concentrated. The concentrate was purified by silica gel column chromatography (hexanes: DCM 6: 1) and recrystallized from hexanes to give **3.10** as white crystals (480 mg, 70%). ^{1}H NMR (400 MHz, $CDCl_3$): 7.95 (s, 2H), 7.81 (d, 2H), 7.72 (dd, 2H), 7.27 (d, 2H), 6.80 (d, 2H), 2.87 (t, 4H), 1.75 (m, 4H), 1.30-1.48 (b, 12H), 0.93 (t, 6H). ^{13}C NMR (300 MHz, $CDCl_3$): 146.3, 141.9, 133.0, 132.3, 128.6, 125.4, 124.9, 123.5, 123.3, 31.9, 30.6, 29.1, 22.8, 14.4. HRMS: calcd. 460.2258, found 460.2257. DSC data was reported on page 23.

2,6-bis(5-hexylthiophen-2-yl)anthracene (3.12, LCS7). To a round bottom flask was added 2,6-anthracenyl bistriflate (285mg, 0.6 mmol), 5-hexyl-2-thiopheneboronic acid pinacol ester (0.54 ml, 1.8 mmol), $Pd(PPh_3)_4$ (28 mg, 0.024 mmol), KBr (157mg, 1.32 mmol), and K_3PO_4 (382 mg, 1.8 mmol). The flask was pumped and refilled three times, followed by adding 25 ml degassed dioxane. After refluxing overnight, a second batch of $Pd(PPh_3)_4$ (28 mg, 0.024 mmol) was added, and the reaction was refluxed again overnight. After cooling down, the reaction mixture was poured into 50 ml methanol, and

the yellow precipitate was filtered off, washed with water, methanol, and then acetone three times. The crude product was purifed by silica gel column chromatography (hexanes: DCM 1: 1) and recrystallized from xylenes to give **3.12** as yellow crystals (170 mg, 55%). ^{1}H NMR (300 MHz, $CDCl_3$): 8.37 (s, 2H), 8.14(s, 2H), 8.00 (d, 2H), 7.75 (d, 2H), 7.34 (m, 2H), 6.85 (d, 2H), 2.90 (t, 4H), 1.76 (m, 4H), 1.26-1.52 (b, 12H), 0.94 (t, 6H). HRMS: calcd. 510.2415, found 510.2410. DSC data was reported on page 23.

Appendix B: HOMO-LUMO Calculations

Efficient carrier injection from electrodes into organic semiconductors is a prerequisite to achieve high mobility. As a rough estimation, the height of the Schottky barrier formed at the metal-semiconductor interface can be calculated by $\phi_{MS}=\phi_{HOMO}-\phi_{M}$ for p-type organic semiconductors, where ϕ_{HOMO} is the depth of HOMO level of the organic semiconductor, and ϕ_{M} is the work function of the electrode.

Compound	Calculated			Experimental		
	HOMO	LUMO	E_g	HOMO	LUMO	E_g
LCS1	-5.33	-1.85	3.48			
LCS2	-5.29	-1.76	3.53			
LCS3	-5.20	-1.69	3.51			
LCS4	-5.01	-2.02	2.99			
LCS5	-5.44	-1.49	3.95			
LCS6	-5.40	-1.66	3.74			
LCS7	-5.22	-2.07	3.15			
anthracene	-5.47	-1.89	3.58	NA	NA	3.22[a]
tetracene	-5.10	-2.33	2.77	-5.36[b]	-2.78[b]	2.58[b]/2.45[b]
pentacene	-4.84	-2.64	2.20	NA	NA	2.08[c]

Table B1 Calculated HOMO, LUMO energy levels. Unit: eV. The Calculations were performed by Spartan '06 using B3LYP functional and 6-311G* basis sets. [a]Estimated from absorbance edge (385 nm). [b]Estimated from cyclic voltammetry and absorbance edge data in ref. [130]. [c]Estimated from data in ref. [131].

To predict whether LCS1 through LCS7 are good candidates for p-type organic semiconductors, the molecular orbitals (MOs) were calculated by density functional theory (DFT) method. The results are shown in Figure B1 and Table B1. The MOs of anthracene, tetracene and pentacene were also calculated for references, and comparison

with experimental data showed that the error of DFT calculation was about 0.3 eV. The HOMO level of anthracene (-5.47eV) can be regarded as the limit of HOMO level to allow efficient hole injection. The calculation revealed that all the LCSs have acceptable HOMO levels higher than -5.47eV.

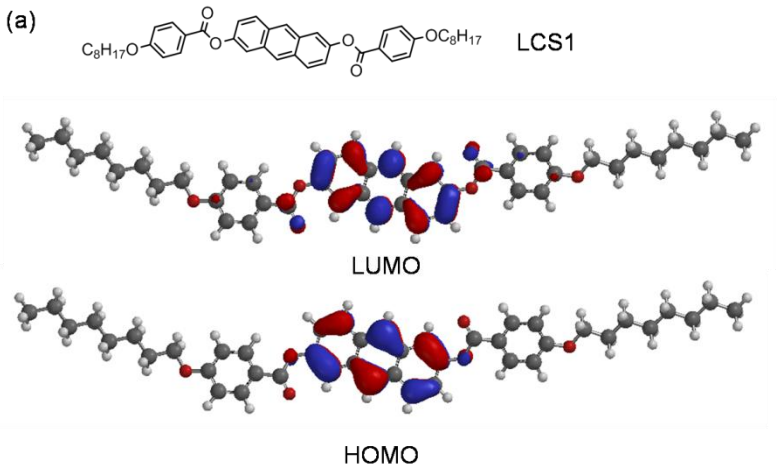

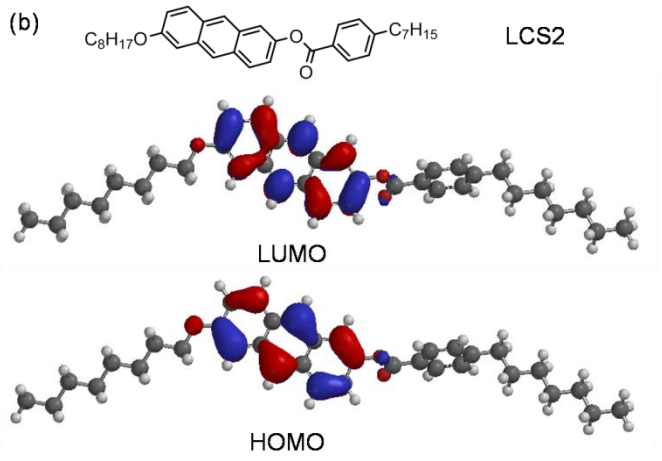

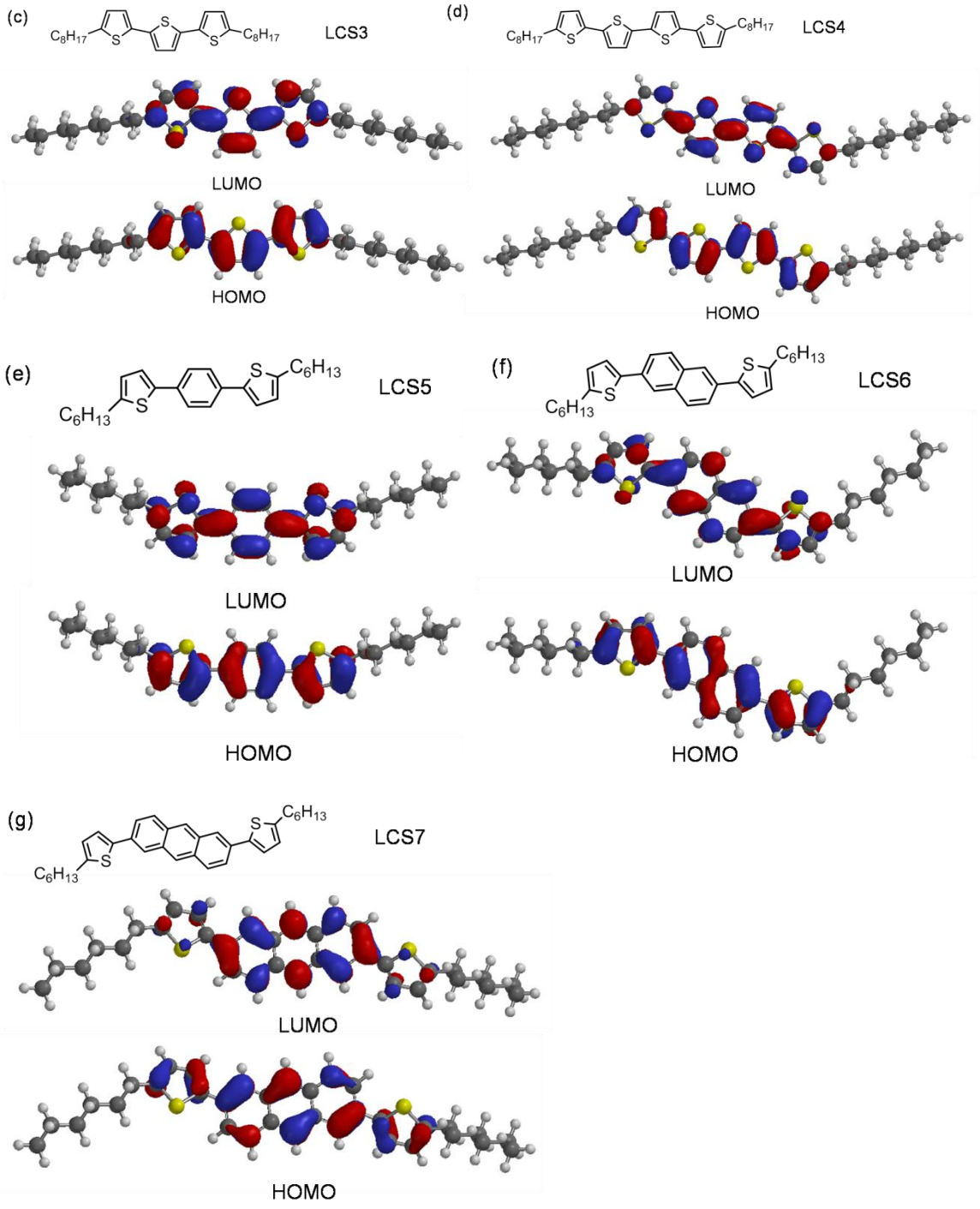

Figure B1 Calculated HOMOs and LUMOs of LCS1 through LCS7.

Appendix C: Synthetic Details for PMMA Copolymers

Reagents. Azobisisobutyronitrile (AIBN) was purified by recrystallization from methanol. Commercial monomers were stirred with basic alumina and anhydrous calcium sulfate to remove inhibitors and moisture before use. Tris-((1-(3-hydroxypropyl)-1,2,3-triazol-4-yl)methyl)-amine (THPTA)[132] were synthesized according to literature procedures.

N-Hydroxysuccinimide methacrylate (NHSMA). N-hydroxysuccinimide (11.5 g, 100 mmol) and triethylamine (14.0 ml, 100 mmol) was dissolved in 100 ml of dichloromethane and the solution was cooled to 0°C. Methacryloyl chloride (10.8 ml, 110 mmol) was added dropwise, and the reaction was stirred at 0°C for 30 min. The reaction was quenched with 100 ml ice-cold water. The organic layer was separated and washed with additional water, brine, dried over $MgSO_4$, and then concentrated with a rotary evaporator. The crude product was recrystallized in hexane/ethyl acetate (3:1) to give a white crystal (12.7 g, 69%). m.p. 99-100 °C (Lit.[133] 100.9 °C). ^{1}H NMR (300 MHz, $CDCl_3$): 6.39 (s, 1H), 5.86 (s, 1H), 2.84 (s, 4H), 2.03 (s, 3H); ^{13}C NMR (300 MHz, $CDCl_3$): 169.6, 162.4, 132.1, 130.7, 25.8, 18.4. HRMS: calcd. $[M+H]^+$ 184.0610, found 184.0611.

Pentafluorophenyl methacrylate (PFPMA). Pentafluorophenol (9.2 g, 50.0 mmol) and pyridine (4.5 ml, 57.9 mmol) was dissolved in 130 ml of anhydrous diethyl ether and the solution was cooled to 0°C. A solution of methacryloyl chloride (5.6 ml, 57.3 mmol) in 70 ml ether was added dropwise, and then the reaction was warmed up to room temperature and stirred for 4 hr. The pyridinium chloride precipitate was filtered off and washed with ether. The combined filtrate solution was washed sequentially with 3% HCl, 3% $NaHCO_3$, and brine. The washed ether solution was dried over $MgSO_4$ and concentrated with a rotary evaporator. The crude product was purified by distillation at 54℃/6 mmHg to afford a colorless liquid (10.5 g, 83%). ^{1}H NMR (400 MHz, $CDCl_3$):

6.453 (s, 1H), 5.912 (s, 1H), 2.090 (s, 3H); ^{13}C NMR (300 MHz, $CDCl_3$): 163.3, 143.2, 141.3, 139.8, 138.0, 136.5, 133.9, 130.1, 125.6, 18.4; ^{19}F NMR (300 MHz, $CDCl_3$): -153.4 (d, 2F), -158.9 (t, 1F), -163.2 (dd, 2F). HRMS: calcd. $[M+H]^+$ 253.0288, found 253.0289.

2-(3,6-Epoxy-1,2,3,6-tetrahydrophthalimido)ethanol (PE). To a dried 3-neck round bottom flask with reflux condenser was added 3,6-epoxy-1,2,3,6-tetrahydrophthalic anhydride (30.0 g, 181 mmol), followed by dry methanol (60 mL) and ethanolamine (10.9 ml, 194 mmol). The solution turned orange upon addition of ethanolamine. The mixture was stirred at room temperature for 30 minutes and then refluxed for 24 hours. The mixture was cooled to room temperature, stayed still for 2 hours, and then stored in a freezer overnight. The product crystallized, and the precipitated crystals were collected by filtration. The filtrate was concentrated and a second crop of crystals were collected and washed with cold methanol (combined 20.5 g, 54%). m.p. 134~136°C (decomposition). (Lit.[134] 135~136°C) ^{1}H NMR (300 MHz, DMSO-d_6): 6.535 (s, 2H), 5.107 (s, 2H), 4.767 (t, 1H), 3.401 (m, 4H), 2.911 (s, 2H); ^{13}C NMR (DMSO-d_6): 176.5, 136.5, 80.3, 57.3, 47.1, 40.6. HRMS: calcd. 209.0688, found 209.0687.

2-(3,6-Epoxy-1,2,3,6-tetrahydrophthalimido)ethyl methacrylate (PEMA). To a dry flask was added PE (5.0 g, 23.9 mmol), Et_3N (3.8 ml, 27.3 mmol) and dry THF (100 ml). The solution was cooled to 0°C, and methacryloyl chloride (2.4 ml, 24.6 mmol) was added dropwise. The reaction was shielded from light, warmed up to room temperature and stirred overnight. The ammonium salt was filtered off, and the filtrate was washed with 0.1M HCl, 0.1M $NaHCO_3$, and brine. The organic layer was dried over $MgSO_4$, filtered, and 250 μL of 2 mg/ml 2,6-Di-tert-butyl-4-methylphenol (BHT) in toluene was added as an radical inhibitor. The solution was concentrated and then purified by silica gel column chromatography (hexanes: ethyl acetate 1:1) to give the product as a white solid (4.0 g, 63%). m.p. 66~68°C. ^{1}H NMR (400 MHz, $CDCl_3$): 6.501 (s, 2H), 6.055 (s, 1H), 5.545 (s, 1H), 5.245 (s, 2H), 4.273 (t, 2H), 3.796 (t, 2H), 2.854 (s, 2H), 1.888 (s,

3H); ^{13}C NMR (300 MHz, $CDCl_3$): 176.2, 167.2, 136.8, 136.1, 126.3, 81.1, 61.1, 47.7, 38.0, 18.4. HRMS: calcd. 277.0950, found 277.0951.

Poly(methyl methacrylate-r-pentafluorophenyl methacrylate) (PMMA-r-PFPMA). To a dry round bottom flask with a reflux condenser, AIBN (39 mg, 0.24 mmol) was added, and the apparatus was evacuated and refilled with nitrogen three times. Dry THF (40 ml) was added, followed by methyl methacrylate (4.26 ml, 40.0 mmol) and pentafluorophenyl methacrylate (1.40 ml, 8.0 mmol). The flask was evacuated and refilled with nitrogen three more times, and then transferred to a preheated oil bath. After refluxing overnight, the solution was cooled to room temperature and added dropwise to 400 ml hexane. The precipitated polymer was collected by filtration and dried under vacuum (4.7 g, 78%).

Poly(methyl methacrylate-r-glycidyl methacrylate) (PMMA-r-GMA). PMMA-r-GMA was prepared using a similar procedure with MMA (5.0 ml, 46.9 mmol), GMA (1.25 ml, 9.39 mmol), AIBN (42 mg, 0.26 mmol) and THF (40 ml). The polymer was precipitated in methanol (4.8 g, 80%).

Poly(methyl methacrylate-r-N-hydroxysuccinimide methacrylate) (PMMA-r-NHSMA). PMMA-r-NHSMA was prepared using a similar procedure with MMA (3.83 ml, 36 mmol), NHSMA (1.32 g, 9.39 mmol), AIBN (141 mg, 0.86 mmol) and THF (40 ml). The polymer was precipitated in hexane (4.5 g, 92%).

Poly(methyl methacrylate-r-methacrylic acid) (PMMA-r-MAA). PMMA-r-MAA was prepared using a similar procedure with MMA (10.6 ml, 100 mmol), MAA (1.7 ml, 20 mmol), AIBN (40 mg, 0.24 mmol) and THF (100 ml). The polymer was precipitated in hexane (8.0 g, 68%).

Poly(methyl methacrylate-r-2-(3,6-epoxy-1,2,3,6-tetrahydro-phthalimido)ethyl methacrylate) (PMMA-r-PEMA). PMMA-r-PEMA was prepared using a similar procedure with MMA (5.0 ml, 46.9 mmol), PEMA (2.6 g, 9.38 mmol), AIBN (46 mg, 0.28 mmol) and THF (50 ml). The polymerization mixture was refluxed with the silicone oil bath set to 70°C. The polymer was precipitated in methanol (5.4 g, 74%).

Poly(methyl methacrylate-r-2-maleimidoethyl methacrylate) (PMMA-r-MEMA). PMMA-r-MEMA was obtained by heating PMMA-r-PEMA under vacuum at 130°C for 4 hr.

Poly(methyl methacrylate-r-propargyl methacrylate) (PMMA-r-PMA). PMMA-r-PMA was prepared using a similar procedure with MMA (10.6 ml, 100 mmol), PMA (2.51 ml, 20 mmol), AIBN (100 mg, 0.6 mmol) and THF (125 ml).. The polymerization mixture was refluxed with the silicone oil bath set to 70°C. The polymer was precipitated in methanol (9.4g, 75%).

Appendix D: Buffer Abbreviations and Formulations

EDTA: ethylenediaminetetraacetic acid.

SSPE: saline-sodium phosphate-EDTA. 1 × SSPE buffer contains 10 mM NaH_2PO_4, 150 mM NaCl, and 1 mM EDTA (pH 7.4).

SSC: saline-sodium citrate. 1 × SSC buffer contains 15 mM trisodium citrate, and 150 mM NaCl (pH 7.0).

MES: 2-(N-morpholino)ethanesulfonic acid. MES buffer was prepared by dissolving MES hemisodium salt in water and adjusted to the target pH using HCl or NaOH solution.

HEPES: 4-(2-hydroxyethyl)-1-piperazineethanesulfonic acid.

TEAB: triethylammonium bicarbonate. 1M TEAB buffer was prepared by bubbling CO_2 from dry ice into a 1M triethylamine solution at 0°C until its pH dropped below 8. The buffer was stored at 4°C.

The buffers used for amine-active ester chemsitry is shown in Table D1.

Nominal pH	Measured pH	Content
6	5.98	KH_2PO_4 + NaOH
7	7.11	KH_2PO_4 + K_2HPO_4
8	8.04	KH_2PO_4 + K_2HPO_4
9	9.06	K_2HPO_4 + NaOH
10	9.98	$NaHCO_3$ + Na_2CO_3
10.5	10.41	$NaHCO_3$ + Na_2CO_3
11	10.99	$NaHCO_3$ + Na_2CO_3
11.5	11.57	K_2HPO_4 + NaOH
12	12.08	K_3PO_4
13	13.04	NaOH

Table D1 Buffers to control pH in amine-active ester chemistry.

Appendix E: Calculation of Amine-Active Ester Chemistry

The competition between the amine-active ester reaction and the hydrolysis of the active ester can be described as follows:

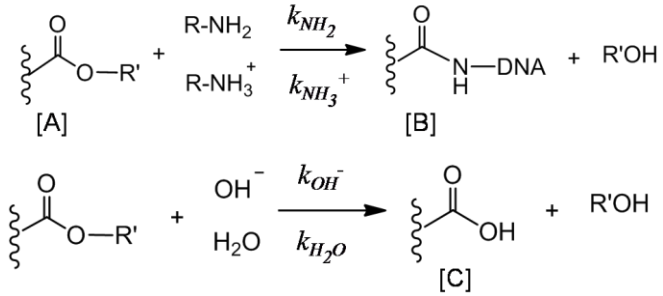

Let A denote the active ester, B the desired amide conjugation product, and C the hydrolyzed side product, then:

$$A + RNH_2 \xrightarrow{k_{NH_2}} B$$

$$A + RNH_3^+ \xrightarrow{k_{NH_3^+}} B$$

$$A + OH^- \xrightarrow{k_{OH^-}} C$$

$$A + H_2O \xrightarrow{k_{H_2O}} C$$

The reaction rates can be given by:

$$\frac{d[A]}{dt} = -k_{NH_2}[A][RNH_2] - k_{NH_3^+}[A][RNH_3^+] - k_{OH^-}[A][OH^-] - k_{H_2O}[A][H_2O] \qquad \text{(E.1)}$$

$$\frac{d[B]}{dt} = k_{NH_2}[A][RNH_2] + k_{NH_3^+}[A][RNH_3^+] \qquad \text{(E.2)}$$

$$\frac{d[R]}{dt} = -k_{NH_2}[A][RNH_2] - k_{NH_3^+}[A][RNH_3^+] \qquad \text{(E.3)}$$

where k_{NH2}, k_{NH3+}, k_{OH-} and k_{H2O} is the rate constant of the active ester reacting with free amine, protonated amine, hydroxide, and water, respectively. Typically, $k_{NH2} >> k_{NH3+}$ and $k_{OH-} >> k_{H2O}$.

In dilute aqueous solution, the water concentration is nearly constant (about 55.5 M), and the hydroxide concentration is:

$$[OH^-] = 10^{(pH-14)} \tag{E.4}$$

The concentrations of free amine and of protonated amine are:

$$[RNH_2] = \frac{[R]}{1+10^{(pK_a-pH)}} \tag{E.5a}$$

$$[RNH_3^+] = \frac{[R]}{1+10^{(pH-pK_a)}} \tag{E.5b}$$

where pK_a is the logarithmic acid dissociation constant of the protonated amine, and [R] is the total concentration of the amine.

Equations (E.1) through (E.5) can be solved together numerically if all the rate constants and the initial concentrations are known.

Initial concentrations. Considering the PMMA-r-PFPMA polymer of a 5:1 component ratio, an equivalent molecular weight of the PFP ester is about 752. Assume that the polymer has a density close to PMMA (1.16g/cm^2). The 3D density of PFP ester group in the polymer is:

$$c_{3D} = \frac{\rho}{M} = \frac{1.16\ g/cm^3}{752\ g/mol} = 1.54\times10^{-3}\ mol/cm^3$$

Assume that the reaction only takes place at the polymer surface. A monolayer of PMMA is about 1.5 nm thick.[135] Therefore, the 2D density of PFP ester group is:

$$c_{2D} = c_{3D} \bullet t = 231\ pmol/cm^2$$

If half of the PFP ester group is in a conformation that is accessible to the amine in the solution, then the surface density of pentafluorophenyl ester group, $[A]_0$, can be assumed to be 116 pmol/cm^2.

A typical conjugation solution is 10 μL of 10 μM of DNA, and the spot size is about 0.12 cm^2. A 100% conjugation yield based on DNA concentration will give a DNA surface density of 833 pmol/cm^2. Therefore, it can be assumed that $[R]_0 \approx 7.2\ [A]_0$.

Calculation results. The rest of the parameters, including pK_a, k_{NH2}, k_{NH3+}, k_{OH-}, and k_{H2O} are assigned arbitrarily to test the effect of these parameters on the conjugation yield. The optimal pH of DNA conjugation largely depends on the pK_a of the amine (protonated), as shown in Figure E1. If the pK_a of the amine is 8 to 9, the conjugation yield has a large plateau region and a low onset pH. A higher pK_a of amine will require higher pH to achieve good conjugation yield.

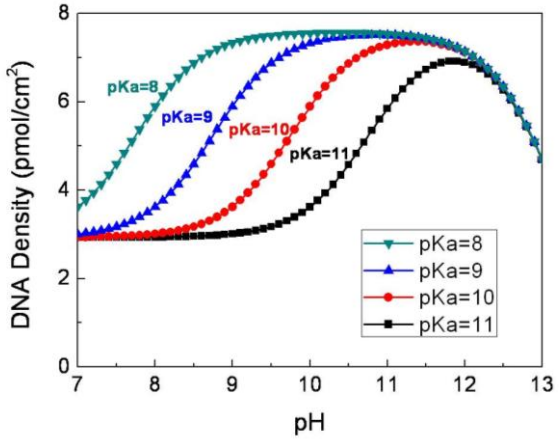

Figure E1 Effect of the pK_a of the amine on the conjugation yield. Other parameters: $k_{NH2} = 4.5$, $k_{NH3+} = 1$, $k_{OH-} = 40$, and $k_{H2O} = 0.05$.

Changing the reactivity of protonated amine k_{NH3+} mainly affects the conjugation yield at low pH, as shown in Figure E2. The reactivity of free amine k_{NH2} is a major factor for the conjugation yield, as shown in Figure E3.

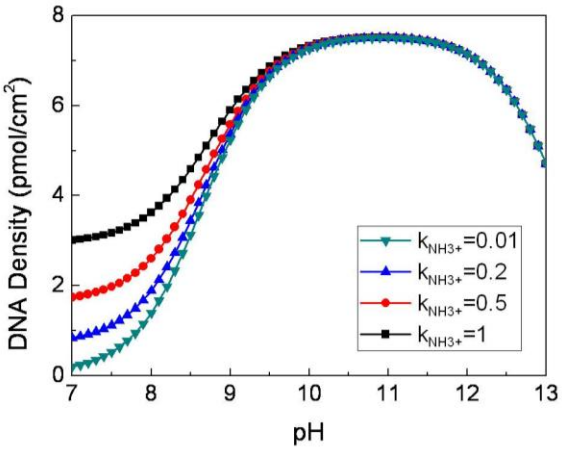

Figure E2 Effect of k_{NH3+} on the conjugation yield. Other parameters: pK_a = 9, k_{NH2} = 4.5, k_{OH-} = 40, and k_{H2O} = 0.05.

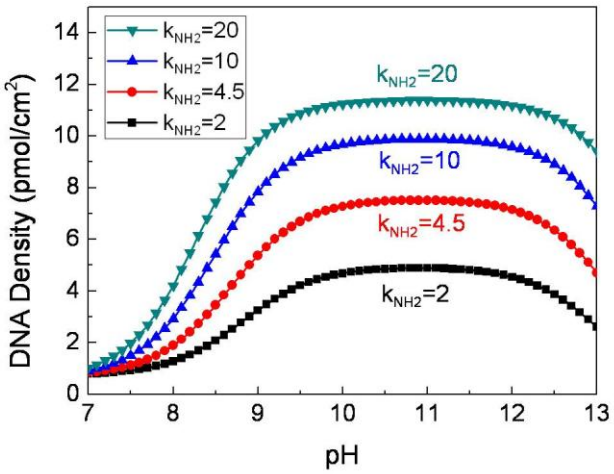

Figure E3 Effect of k_{NH2} on the conjugation yield. Other parameters: pK_a = 9, k_{NH3+} = 0.2, k_{OH-} = 40, and k_{H2O} = 0.05.

The hydrolysis rate with water k_{H2O} is another factor that affects the conjugation yield significantly. Increasing k_{H2O} leads to rapid decrease in conjugation yield (Figure E4). The hydrolysis rate of hydroxide k_{OH-} mainly affects the conjugation yield at high pH, as shown in Figure E5. The best fit with experiment data (Figure 5.9) was calculated at pK_a = 9.1, k_{NH3+} = 1, k_{NH2} = 4.5, k_{OH-} = 40, and k_{H2O} = 0.05.

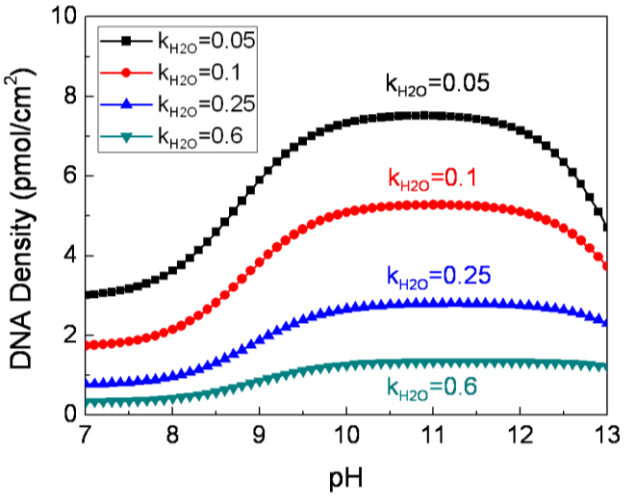

Figure E4 Effect of k_{H2O} on the conjugation yield. Other parameters: pK_a = 9, k_{NH3+} = 1, k_{NH2} = 4.5, and k_{OH-} = 40.

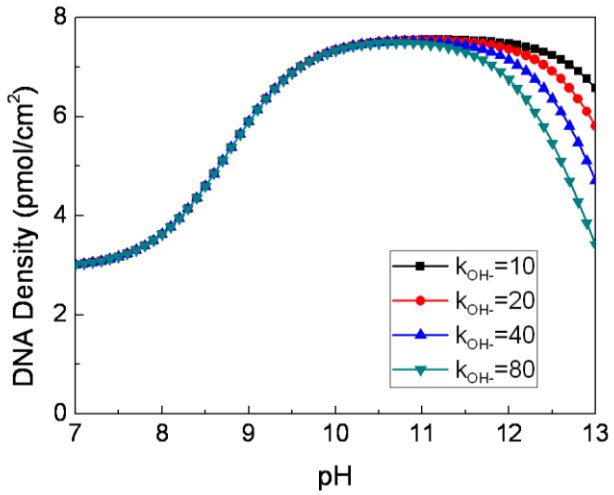

Figure E5 Effect of k_{OH-} on the conjugation yield. Other parameters: pK_a = 9, k_{NH3+} = 1, k_{NH2} = 4.5, and k_{H2O} = 0.05.

References

1. G. M. Whitesides, M. Boncheva, Beyond molecules: self-assembly of mesoscopic and macroscopic components. *Proceedings of the National Academy of Sciences of the United States of America* **99**, 4769 (2002).
2. R. Groβ, M. Dorigo, Self-Assembly at the macroscopic scale. *Proceedings of the IEEE* **96**, 1490 (2008).
3. D. B. Levitt *et al.*, Identification and Evaluation of High-Performance EOR Surfactants. *SPE Reservoir Evaluation and Engineering* **12**, 243 (2006).
4. J. N. Israelachvili, D. J. Mitchell, B. W. Ninham, Theory of self-assembly of hydrocarbon amphiphiles into micelles and bilayers. *Journal of the Chemical Society, Faraday Transactions 2: Molecular and Chemical Physics* **72**, 1525 (1976).
5. L. Zhang *et al.*, Nanoparticles in Medicine: Therapeutic Applications and Developments. *Clin Pharmacol Ther* **83**, 761 (2007).
6. P. S. Pershan, Lyotropic liquid crystals. *Physics Today* **35**, 34 (1982).
7. C. R. Safinya, Structures of lipid–DNA complexes: supramolecular assembly and gene delivery. *Current Opinion in Structural Biology* **11**, 440 (2001).
8. C. Tros de Ilarduya, Y. Sun, N. Düzgüneş, Gene delivery by lipoplexes and polyplexes. *European Journal of Pharmaceutical Sciences* **40**, 159 (2010).
9. C. M. Bates *et al.*, Polymeric Cross-Linked Surface Treatments for Controlling Block Copolymer Orientation in Thin Films. *Langmuir : the ACS journal of surfaces and colloids* **27**, 2000 (2011).
10. F. S. Bates *et al.*, Multiblock Polymers: Panacea or Pandora's Box? *Science* **336**, 434 (2012).
11. S. B. Darling, Directing the self-assembly of block copolymers. *Progress in Polymer Science* **32**, 1152 (2007).
12. J. D. Cushen *et al.*, Oligosaccharide/Silicon-Containing Block Copolymers with 5 nm Features for Lithographic Applications. *ACS nano* **6**, 3424 (2012).
13. S. M. George, Atomic Layer Deposition: An Overview. *Chemical Reviews* **110**, 111 (2009).
14. J. W. Elam *et al.*, Mechanism for zirconium oxide atomic layer deposition using bis(methylcyclopentadienyl)methoxymethyl zirconium. *Applied Physics Letters* **91**, 253123 (2007).
15. C.-a. Di, Y. Liu, G. Yu, D. Zhu, Interface Engineering: An Effective Approach toward High-Performance Organic Field-Effect Transistors. *Accounts of Chemical Research* **42**, 1573 (2009).
16. Y. Don Park, J. A. Lim, H. S. Lee, K. Cho, Interface engineering in organic transistors. *Materials Today* **10**, 46 (2007).
17. M. Colburn *et al.*, Step and flash imprint lithography: a new approach to high-resolution patterning. *Proceedings of SPIE* **3676**, 379 (1999).

18. K. Wu, T. C. Bailey, C. G. Willson, J. G. Ekerdt, Surface Hydration and Its Effect on Fluorinated SAM Formation on SiO2 Surfaces. *Langmuir : the ACS journal of surfaces and colloids* **21**, 11795 (2005).
19. M. C. Pirrung, How to Make a DNA Chip. *Angewandte Chemie International Edition* **41**, 1276 (2002).
20. S. H. Park, Y. Xia, Assembly of Mesoscale Particles over Large Areas and Its Application in Fabricating Tunable Optical Filters. *Langmuir : the ACS journal of surfaces and colloids* **15**, 266 (1999).
21. K. Hosokawa, I. Shimoyama, H. Miura, Dynamics of Self-Assembling Systems: Analogy with Chemical Kinetics. *Artificial Life* **1**, 413 (1994).
22. K. Liu *et al.*, Step-Growth Polymerization of Inorganic Nanoparticles. *Science* **329**, 197 (2010).
23. Q. Chen, S. C. Bae, S. Granick, Directed self-assembly of a colloidal kagome lattice. *Nature* **469**, 381 (2011).
24. P. W. Rothemund, Folding DNA to create nanoscale shapes and patterns. *Nature* **440**, 297 (2006).
25. S. J. Riedl, W. Li, Y. Chao, R. Schwarzenbacher, Y. Shi, Structure of the apoptotic protease-activating factor 1 bound to ADP. *Nature* **434**, 926 (2005).
26. E. P. Diamandis, T. K. Christopoulos, The biotin-(strept)avidin system: principles and applications in biotechnology. *Clinical Chemistry* **37**, 625 (1991).
27. K. Keren, R. S. Berman, E. Buchstab, U. Sivan, E. Braun, DNA-Templated Carbon Nanotube Field-Effect Transistor. *Science* **302**, 1380 (2003).
28. H. Shirakawa, E. J. Louis, A. G. MacDiarmid, C. K. Chiang, A. J. Heeger, Synthesis of electrically conducting organic polymers: halogen derivatives of polyacetylene, (CH). *Journal of the Chemical Society, Chemical Communications*, 578 (1977).
29. A. Tsumura, H. Koezuka, T. Ando, Macromolecular electronic device: Field-effect transistor with a polythiophene thin film. *Applied Physics Letters* **49**, 1210 (1986).
30. B. J. de Gans, P. C. Duineveld, U. S. Schubert, Inkjet Printing of Polymers: State of the Art and Future Developments. *Advanced Materials* **16**, 203 (2004).
31. H. Minemawari *et al.*, Inkjet printing of single-crystal films. *Nature* **475**, 364 (2011).
32. K. Jain, M. Klosner, M. Zemel, S. Raghunandan, Flexible Electronics and Displays: High-Resolution, Roll-to-Roll, Projection Lithography and Photoablation Processing Technologies for High-Throughput Production. *Proceedings of the IEEE* **93**, 1500 (2005).
33. M. Irimia-Vladu *et al.*, Biocompatible and Biodegradable Materials for Organic Field-Effect Transistors. *Advanced Functional Materials* **20**, 4069 (2010).
34. M. Kitamura, Y. Arakawa, Pentacene-based organic field-effect transistors. *Journal of Physics: Condensed Matter* **20**, 184011 (2008).
35. R. A. Marcus, N. Sutin, Electron transfers in chemistry and biology. *Biochimica et Biophysica Acta (BBA) - Reviews on Bioenergetics* **811**, 265 (1985).

36. Z. Shuai, L. Wang, C. Song, *Theory of Charge Transport in Carbon Electronic Materials*. (Springer, 2012).
37. F. V. Farmakis *et al.*, On-current modeling of large-grain polycrystalline silicon thin-film transistors. *Electron Devices, IEEE Transactions on* **48**, 701 (2001).
38. V. C. Sundar *et al.*, Elastomeric transistor stamps: reversible probing of charge transport in organic crystals. *Science* **303**, 1644 (2004).
39. S. Liu *et al.*, Patterning of α-Sexithiophene Single Crystals with Precisely Controlled Sizes and Shapes. *Chemistry of Materials* **21**, 15 (2009).
40. R. W. I. de Boer, M. E. Gershenson, A. F. Morpurgo, V. Podzorov, Organic single-crystal field-effect transistors. *physica status solidi (a)* **201**, 1302 (2004).
41. H. Sirringhaus *et al.*, Mobility enhancement in conjugated polymer field-effect transistors through chain alignment in a liquid-crystalline phase. *Applied Physics Letters* **77**, 406 (2000).
42. T. Fujiwara, J. Locklin, Z. Bao, Solution deposited liquid crystalline semiconductors on a photoalignment layer for organic thin-film transistors. *Applied Physics Letters* **90**, 232108 (2007).
43. I. O. Shklyarevskiy *et al.*, High anisotropy of the field-effect transistor mobility in magnetically aligned discotic liquid-crystalline semiconductors. *Journal of the American Chemical Society* **127**, 16233 (2005).
44. P. J. Collings, *Liquid Crystals: Nature's Delicate Phase of Matter, Second Edition*. (Princeton University Press, 2001).
45. J. J. Reczek, K. R. Villazor, V. Lynch, T. M. Swager, B. L. Iverson, Tunable Columnar Mesophases Utilizing C2 Symmetric Aromatic Donor−Acceptor Complexes. *Journal of the American Chemical Society* **128**, 7995 (2006).
46. A. J. van Breemen *et al.*, Large area liquid crystal monodomain field-effect transistors. *Journal of the American Chemical Society* **128**, 2336 (2006).
47. C. Tschierske, Micro-segregation, molecular shape and molecular topology - partners for the design of liquid crystalline materials with complex mesophase morphologies. *Journal of Materials Chemistry* **11**, 2647 (2001).
48. The term nematic comes from the greek word "νήματος" which means thread, because nematic liquid crystals may have thread-like defect lines under polarized microscopy. The term smectic comes from the greek word "σμηγμα" which means soap, owing to the fact that smectic liquid crystals have soap-like mechanical properties.
49. G. W. Gray, J. W. G. Goodby, *Smectic liquid crystals: textures and structures*. (Leonard Hill, 1984).
50. I. Dierking, *Textures of Liquid Crystals*. (John Wiley & Sons, 2006).
51. H. Kawamoto, The history of liquid-crystal displays. *Proceedings of the IEEE* **90**, 460 (2002).
52. D. Pauluth, K. Tarumi, Optimization of liquid crystals for television. *Journal of the Society for Information Display* **13**, 693 (2005).
53. P. Kirsch *et al.*, Super-Fluorinated Liquid Crystals: Towards the Limits of Polarity. *European Journal of Organic Chemistry* **2008**, 3479 (2008).

54. S. Norvez, F.-G. Tournilhac, P. Bassoul, P. Herson, Mesomorphism and Polar Distortion in 1,4,5,8-Tetrasubstituted Anthraquinones and Anthracenes. *Chemistry of Materials* **13**, 2552 (2001).
55. K. Okamoto, T. Kawamura, M. Sone, K. Ogino, Study on liquid crystallinity in 2,9-dialkylpentacenes. *Liquid Crystals* **34**, 1001 (2007).
56. V. Lemaur *et al.*, Structural and Charge-Transport Properties of a Liquid-Crystalline α,ω-Disubstituted Thiophene Derivative: A Joint Experimental and Theoretical Study. *The Journal of Physical Chemistry C* **114**, 4617 (2010).
57. P. N. Murgatroyd, Theory of space-charge-limited current enhanced by Frenkel effect. *Journal of Physics D: Applied Physics* **3**, 151 (1970).
58. K. C. Kao, Double injection in solids with non-ohmic contacts. I. Solids without defects. *Journal of Physics D: Applied Physics* **17**, 1433 (1984).
59. G. Horowitz, Organic Field-Effect Transistors. *Advanced Materials* **10**, 365 (1998).
60. C. H. Kim *et al.*, Capacitive behavior of pentacene-based diodes: Quasistatic dielectric constant and dielectric strength. *Journal of Applied Physics* **109**, 083710 (2011).
61. A. Ghanadzadeh, M. S. Beevers, Effect of surface and molecular structure on the dielectric behaviour in thick layers of cyanobiphenyl liquid crystals. *Journal of Molecular Liquids* **100**, 47 (2002).
62. R. W. I. de Boer, Space charge limited transport and time of flight measurements in tetracene single crystals: A comparative study. *Journal of Applied Physics* **95**, 1196 (2004).
63. M. M. Payne, S. R. Parkin, J. E. Anthony, C. C. Kuo, T. N. Jackson, Organic field-effect transistors from solution-deposited functionalized acenes with mobilities as high as 1 cm2/V x s. *Journal of the American Chemical Society* **127**, 4986 (2005).
64. S. Sang-Il, K. Jae-Hong, K. Hochul, J. Byeong-Kwon, Solution-processed 6,13-bis(triisopropylsilylethynyl) (TIPS) pentacene thin-film transistors with a polymer dielectric on a flexible substrate. *Semiconductor Science and Technology* **23**, 085009 (2008).
65. C. A. Mirkin, R. L. Letsinger, R. C. Mucic, J. J. Storhoff, A DNA-based method for rationally assembling nanoparticles into macroscopic materials. *Nature* **382**, 607 (1996).
66. R. J. Macfarlane *et al.*, Nanoparticle superlattice engineering with DNA. *Science* **334**, 204 (2011).
67. M. P. Valignat, O. Theodoly, J. C. Crocker, W. B. Russel, P. M. Chaikin, Reversible self-assembly and directed assembly of DNA-linked micrometer-sized colloids. *Proceedings of the National Academy of Sciences of the United States of America* **102**, 4225 (2005).
68. M. E. Leunissen *et al.*, Towards self-replicating materials of DNA-functionalized colloids. *Soft Matter* **5**, 2422 (2009).

69. C. K. Tison, V. T. Milam, Manipulating DNA probe presentation via enzymatic cleavage of diluent strands. *Biomacromolecules* **9**, 2468 (2008).
70. C. K. Tison, V. T. Milam, Reversing DNA-mediated adhesion at a fixed temperature. *Langmuir : the ACS journal of surfaces and colloids* **23**, 9728 (2007).
71. A. Rajendran, M. Endo, Y. Katsuda, K. Hidaka, H. Sugiyama, Photo-cross-linking-assisted thermal stability of DNA origami structures and its application for higher-temperature self-assembly. *Journal of the American Chemical Society* **133**, 14488 (2011).
72. C. A. Mirkin, Programming the Assembly of Two- and Three-Dimensional Architectures with DNA and Nanoscale Inorganic Building Blocks. *Inorganic Chemistry* **39**, 2258 (2000).
73. MLA style: "Nobelprize.org". Nobelprize.org. 18 Nov 2012 http://www.nobelprize.org/nobel_prizes/chemistry/laureates/1984/presentation-speech.html
74. M. J. Schmid *et al.*, Feature Multiplexing—Improving the Efficiency of Microarray Devices. *Angewandte Chemie International Edition* **45**, 3338 (2006).
75. J. E. Meiring *et al.*, Hydrogel Biosensor Array Platform Indexed by Shape. *Chemistry of Materials* **16**, 5574 (2004).
76. L. F. Thompson, C. G. Willson, J. Bowden, *Introduction to microlithography*. (American Chemical Society, 1994).
77. C. Samyn, W. Ballet, T. Verbiest, M. Van Beylen, A. Persoons, Chromophore functionalised maleimide copolymers with high poling stabilities of the nonlinear optical effect at elevated temperature. *Polymer* **42**, 8511 (2001).
78. J. A. Maynard, R. Myhre, B. Roy, Microarrays in infection and immunity. *Current Opinion in Chemical Biology* **11**, 306 (2007).
79. A. Sassolas, B. D. Leca-Bouvier, L. J. Blum, DNA Biosensors and Microarrays. *Chemical Reviews* **108**, 109 (2007).
80. J. A. Francisco *et al.*, cAC10-vcMMAE, an anti-CD30–monomethyl auristatin E conjugate with potent and selective antitumor activity. *Blood* **102**, 1458 (2003).
81. J. W. Lichtman, J.-A. Conchello, Fluorescence microscopy. *Nat Meth* **2**, 910 (2005).
82. I. D. Johnson, L. Technologies, R. P. Haugland, M. T. Z. Spence, *The Molecular Probes Handbook: A Guide to Fluorescent Probes and Labeling Technologies, 11th Edition*. (Life Technologies, 2010).
83. J. M. Dixon, M. Taniguchi, J. S. Lindsey, PhotochemCAD 2: A Refined Program with Accompanying Spectral Databases for Photochemical Calculations¶ *Photochemistry and Photobiology* **81**, 212 (2005).
84. http://www.idtdna.com/catalog/Modifications/Dyes.aspx
85. http://www.invitrogen.com/site/us/en/home/support/Research-Tools/Fluorescence-SpectraViewer.html
86. G. H. McGall *et al.*, The Efficiency of Light-Directed Synthesis of DNA Arrays on Glass Substrates. *Journal of the American Chemical Society* **119**, 5081 (1997).

87. M. R. Lockett, M. F. Phillips, J. L. Jarecki, D. Peelen, L. M. Smith, A Tetrafluorophenyl Activated Ester Self-Assembled Monolayer for the Immobilization of Amine-Modified Oligonucleotides. *Langmuir : the ACS journal of surfaces and colloids* **24**, 69 (2007).
88. T. M. Herne, M. J. Tarlov, Characterization of DNA Probes Immobilized on Gold Surfaces. *Journal of the American Chemical Society* **119**, 8916 (1997).
89. M. Hatzakis, PMMA copolymers as high sensitivity electron resists. *Journal of Vacuum Science and Technology* **16**, 1984 (1979).
90. W. Moreau *et al.*, Speed enhancement of PMMA resist. *Journal of Vacuum Science and Technology* **16**, 1989 (1979).
91. I. T. Ibrahim, A. Williams, Concerted general acid catalysis in the reaction of acetate ion with water-soluble carbodi-imide. *Journal of the Chemical Society, Chemical Communications*, 25 (1980).
92. T. Lindahl, B. Nyberg, Rate of depurination of native deoxyribonucleic acid. *Biochemistry* **11**, 3610 (1972).
93. G. T. Hermanson, *Bioconjugate Techniques*. (Academic Press, 2008).
94. Z. Zhang *et al.*, Sodium citrate: A universal reducing agent for reduction / decoration of graphene oxide with au nanoparticles. *Nano Research* **4**, 599 (2011).
95. J. C. Han, G. Y. Han, A Procedure for Quantitative Determination of Tris(2-Carboxyethyl)phosphine, an Odorless Reducing Agent More Stable and Effective Than Dithiothreitol. *Analytical Biochemistry* **220**, 5 (1994).
96. A. H. El-Sagheer, T. Brown, Click chemistry with DNA. *Chemical Society Reviews* **39**, 1388 (2010).
97. H. C. Kolb, M. G. Finn, K. B. Sharpless, Click Chemistry: Diverse Chemical Function from a Few Good Reactions. *Angewandte Chemie International Edition* **40**, 2004 (2001).
98. R. Kumar *et al.*, Template-Directed Oligonucleotide Strand Ligation, Covalent Intramolecular DNA Circularization and Catenation Using Click Chemistry. *Journal of the American Chemical Society* **129**, 6859 (2007).
99. K. M. Ririe, R. P. Rasmussen, C. T. Wittwer, Product Differentiation by Analysis of DNA Melting Curves during the Polymerase Chain Reaction. *Analytical Biochemistry* **245**, 154 (1997).
100. J. SantaLucia, A unified view of polymer, dumbbell, and oligonucleotide DNA nearest-neighbor thermodynamics. *Proceedings of the National Academy of Sciences* **95**, 1460 (1998).
101. J. SantaLucia, H. T. Allawi, P. A. Seneviratne, Improved Nearest-Neighbor Parameters for Predicting DNA Duplex Stability†. *Biochemistry* **35**, 3555 (1996).
102. K. J. Breslauer, R. Frank, H. Blöcker, L. A. Marky, Predicting DNA duplex stability from the base sequence. *Proceedings of the National Academy of Sciences* **83**, 3746 (1986).
103. J. N. Zadeh *et al.*, NUPACK: Analysis and design of nucleic acid systems. *Journal of Computational Chemistry* **32**, 170 (2011).

104. D. Nykypanchuk, M. M. Maye, D. van der Lelie, O. Gang, DNA-guided crystallization of colloidal nanoparticles. *Nature* **451**, 549 (2008).
105. M. M. Maye, D. Nykypanchuk, M. Cuisinier, D. van der Lelie, O. Gang, Stepwise surface encoding for high-throughput assembly of nanoclusters. *Nature materials* **8**, 388 (2009).
106. G. Tikhomirov *et al.*, DNA-based programming of quantum dot valency, self-assembly and luminescence. *Nature nanotechnology* **6**, 485 (2011).
107. H. M. Shapiro, *Practical Flow Cytometry*. (John Wiley & Sons, 2003).
108. C. M. Soto, A. Srinivasan, B. R. Ratna, Controlled Assembly of Mesoscale Structures Using DNA as Molecular Bridges. *Journal of the American Chemical Society* **124**, 8508 (2002).
109. L. Bonetta, Flow cytometry smaller and better. *Nature Methods* **2**, 785 (2005).
110. D. A. Basiji, W. E. Ortyn, L. Liang, V. Venkatachalam, P. Morrissey, Cellular Image Analysis and Imaging by Flow Cytometry. *Clinics in Laboratory Medicine* **27**, 653 (2007).
111. G. Helguera *et al.*, Visualization and quantification of cytotoxicity mediated by antibodies using imaging flow cytometry. *Journal of Immunological Methods* **368**, 54 (2011).
112. V. T. Milam, A. L. Hiddessen, J. C. Crocker, D. J. Graves, D. A. Hammer, DNA-Driven Assembly of Bidisperse, Micron-Sized Colloids. *Langmuir : the ACS journal of surfaces and colloids* **19**, 10317 (2003).
113. B. D. Rabideau, R. T. Bonnecaze, A Computational Study of the Hydrodynamically Assisted Organization of DNA-Functionalized Colloids in 2D. *Langmuir : the ACS journal of surfaces and colloids* **23**, 10000 (2007).
114. J. J. Maurer, D. J. Eustace, C. T. Ratcliffe, Thermal characterization of poly(acrylic acid). *Macromolecules* **20**, 196 (1987).
115. C. Lu, M. M.-C. Cheng, A. Benatar, L. J. Lee, Embossing of high-aspect-ratio-microstructures using sacrificial templates and fast surface heating. *Polymer Engineering & Science* **47**, 830 (2007).
116. A. L. Koh, S. University, S. U. D. M. Engineering, *Electron Microscopy Investigations of Nanoparticles for Cancer Diagnostic Applications*. (Stanford University, 2009).
117. J. V. Koleske, *Paint and Coating Testing Manual: Fourteenth Edition of the Gardner-Sward Handbook*. (American Society for Testing & Materials, 1995).
118. T. Izawa, E. Miyazaki, K. Takimiya, Solution-Processible Organic Semiconductors Based on Selenophene-Containing Heteroarenes, 2,7-Dialkyl[1]benzoselenopheno[3,2-b][1]benzoselenophenes (Cn-BSBSs): Syntheses, Properties, Molecular Arrangements, and Field-Effect Transistor Characteristics. *Chemistry of Materials* **21**, 903 (2009).
119. M. Reznikov, B. Wall, M. A. Handschy, P. J. Bos, Monodomain alignment of the smectic-A liquid crystalline phase from the isotropic phase. *Journal of Applied Physics* **104**, 044902 (2008).

120. http://www.neb.com/nebecomm/tech_reference/restriction_enzymes/sequences/GenBank/M13mp18.gbk.txt
121. W. Volksen, R. D. Miller, G. Dubois, Low Dielectric Constant Materials. *Chemical Reviews* **110**, 56 (2009).
122. H. Wang *et al.*, The self-assembly of porous microspheres of tin dioxide octahedral nanoparticles for high performance lithium ion battery anode materials. *Journal of Materials Chemistry* **21**, 10189 (2011).
123. Y.-M. Jeon, G. S. Armatas, J. Heo, M. G. Kanatzidis, C. A. Mirkin, Amorphous Infinite Coordination Polymer Microparticles: A New Class of Selective Hydrogen Storage Materials. *Advanced Materials* **20**, 2105 (2008).
124. Y. Liu, X. Zhang, Metamaterials: a new frontier of science and technology. *Chemical Society Reviews* **40**, 2494 (2011).
125. D. Schurig *et al.*, Metamaterial Electromagnetic Cloak at Microwave Frequencies. *Science* **314**, 977 (2006).
126. Y. Lai *et al.*, Illusion Optics: The Optical Transformation of an Object into Another Object. *Physical Review Letters* **102**, 253902 (2009).
127. J. Leroy, J. Levin, S. Sergeyev, Y. Geerts, Practical One-step Synthesis of Symmetrical Liquid Crystalline Dialkyloligothiophenes for Molecular Electronic Applications. *Chemistry Letters* **35**, 166 (2006).
128. S. Mery *et al.*, Liquid crystals containing a 2,6-disubstituted anthracene core mesomorphism, charge transport and photochemical properties. *Journal of Materials Chemistry* **13**, 1622 (2003).
129. H. W. Boone, H. K. Hall, Novel Polyaromatic Quinone Imines. 2. Synthesis of Model Compounds and Stereoregular Poly(quinone imines) from Disubstituted Anthraquinones. *Macromolecules* **29**, 5835 (1996).
130. K. Ono *et al.*, Synthesis and Properties of BF2 Complexes to Dihydroxydiones of Tetracene and Perylene: Novel Electron Acceptors Showing n-Type Semiconducting Behavior. *Organic letters* **11**, 149 (2008).
131. I. Kaur *et al.*, Substituent Effects in Pentacenes: Gaining Control over HOMO−LUMO Gaps and Photooxidative Resistances. *Journal of the American Chemical Society* **130**, 16274 (2008).
132. T. R. Chan, R. Hilgraf, K. B. Sharpless, V. V. Fokin, Polytriazoles as Copper(I)-Stabilizing Ligands in Catalysis. *Organic Letters* **6**, 2853 (2004).
133. A. M. Alb *et al.*, Quantitative Contrasts in the Copolymerization of Acrylate- and Methacrylate-Based Comonomers. *Macromolecules* **39**, 8283 (2006).
134. Z.-H. Zhou, R.-Y. Chen, Synthesis of Glycerophospholipid Conjugates of Cantharidin and Its Analogues. *Synthetic Communications* **30**, 3527 (2000).
135. M. Kawaguchi, M. Tohyama, Y. Mutoh, A. Takahashi, Ellipsometric study of polymer monolayers spread at the air-water interface. 1. Thickness of monolayers. *Langmuir : the ACS journal of surfaces and colloids* **4**, 407 (1988).

Vita

Hao Tang, son of Minglong Tang and Jufang Du, was born October 24, 1985 in Shanghai, China. He graduated from Chuansha High School in Shanghai, China in 2003 and attended Peking University in Beijing, China from 2003 to 2007. He received his Bachelor of Engineering degree in Microelectronics in July 2007. In the fall of 2007, Hao began graduate studies in the Department of Chemical Engineering at The University of Texas at Austin under the supervision of Professor C. Grant Willson. Hao Tang will work for IBM at Hopewell Junction, NY after his graduation.

Permanent address: 29 Tangjiazhai, Group 2 Duying Village, Chuansha, Shanghai 201202, China

Email: tanghao1985@gmail.com

This dissertation was typed by the author.